AD-A125 767 SCATTERING BY SPHEROIDAL AND ROUGH PARTICLES(U) ARMY ARMAMENT RESEARCH AND DEVELOPMENT COMMAND ABERDEEN PROVING GROUND MD CHEMICAL SYSTEMS LAB 1/1

UNCLASSIFIED D W SCHUERMAN ET AL. DEC 82 ARCSL-CR-82037 F/G 20/6 NL

END

FILMED

DTIC

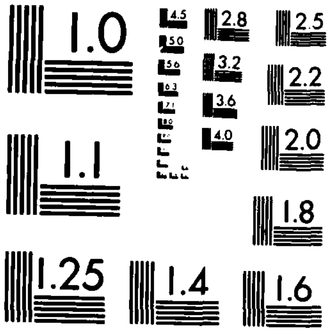

MICROCOPY RESOLUTION TEST CHART
NATIONAL BUREAU OF STANDARDS-1963-A

2

CHEMICAL SYSTEMS LABORATORY CONTRACTOR REPORT

ARCSL-CR-82037

SCATTERING BY SPHEROIDAL AND ROUGH PARTICLES

by

Donald W. Schuerman
Ru T. Wang

December 1982

SPACE ASTRONOMY LABORATORY
University of Florida
Gainesville, Florida 32601

US ARMY ARMAMENT RESEARCH AND DEVELOPMENT COMMAND
Chemical Systems Laboratory
Aberdeen Proving Ground, Maryland 21010

UNCLASSIFIED
SECURITY CLASSIFICATION OF THIS PAGE *(When Data Entered)*

REPORT DOCUMENTATION PAGE

READ INSTRUCTIONS BEFORE COMPLETING FORM

1. REPORT NUMBER
ARCSL-CR-82037

2. GOVT ACCESSION NO.
AD.A125 767

3. RECIPIENT'S CATALOG NUMBER

4. TITLE *(and Subtitle)*
SCATTERING BY SPHEROIDAL AND ROUGH PARTICLES

5. TYPE OF REPORT & PERIOD COVERED
Contract Report
(See preface)

6. PERFORMING ORG. REPORT NUMBER

7. AUTHOR(s)
Donald W. Schuerman
Ru T. Wang

8. CONTRACT OR GRANT NUMBER(s)
See preface.

9. PERFORMING ORGANIZATION NAME AND ADDRESS
Commander, Chemical Systems Laboratory
ATTN: DRDAR-CLB-PS
Aberdeen Proving Ground, Maryland 21010

10. PROGRAM ELEMENT, PROJECT, TASK AREA & WORK UNIT NUMBERS
1L161102A71A-D

11. CONTROLLING OFFICE NAME AND ADDRESS
Commander, Chemical Systems Laboratory
ATTN: DRDAR-CLJ-R
Aberdeen Proving Ground, Maryland 21010

12. REPORT DATE
December 1982

13. NUMBER OF PAGES
94

14. MONITORING AGENCY NAME & ADDRESS *(if different from Controlling Office)*

15. SECURITY CLASS. *(of this report)*
UNCLASSIFIED

15a. DECLASSIFICATION/DOWNGRADING SCHEDULE
NA

16. DISTRIBUTION STATEMENT *(of this Report)*

Approved for public release; distribution unlimited.

17. DISTRIBUTION STATEMENT *(of the abstract entered in Block 20, if different from Report)*

18. SUPPLEMENTARY NOTES

The publication of this report was supported by the Army Smoke Research Program, Chemical Systems Laboratory, Aberdeen Proving Ground, Maryland.

19. KEY WORDS *(Continue on reverse side if necessary and identify by block number)*

20. ABSTRACT *(Continue on reverse side if necessary and identify by block number)*

DD FORM 1 JAN 73 1473 EDITION OF 1 NOV 65 IS OBSOLETE

UNCLASSIFIED
SECURITY CLASSIFICATION OF THIS PAGE *(When Data Entered)*

PREFACE

This work was authorized under Project 1L161102A71A-D, Smoke and Obscurants, Aerosol Obscuration Science. The data were collected over a period of many years in the microwave analog facility of the Space Astronomy Laboratory, State University of New York at Albany. The assembly of the data into a collection appropriate for publication and the performance of the research analyses were supported by National Aeronautics and Space Administration (NASA). This report was initially prepared by NASA but was never published; therefore the Army Smoke Research Program and the Chemical Systems Laboratory are sponsoring publication.

Reproduction of this document in whole or in part is prohibited except with permission of the Commander, Chemical Systems Laboratory, ATTN: DRDAR-CLJ-R, Aberdeen Proving Ground, Maryland 21010. However, the Defense Technical Information Center and the National Technical Information Service are authorized to reproduce the document for United States Government purposes.

A

SCATTERING BY SPHEROIDAL AND ROUGH PARTICLES

CONTENTS:

SCATTERING BY SPHEROIDAL AND ROUGH PARTICLES

I. INTRODUCTION

We live in a world rich in the phenomena of electromagnetic scattering; the blue of the sky, the wonderful colors of colloidal suspensions, rainbows, and, indeed, almost every visual experience is the result of scattering. Curious and analytical minds have been attracted to the scientific explanation of these phenomena in terms of the physical processes involved. This effort, which has been continued from ancient times, has evolved into light scattering studies of academic as well as practical interests. Gradually, it was realized that under most circumstances the total scattered light and also the observed polarization could be estimated from the simple sum of the scattered light from the individual particles in a given medium. This is the so-called single-particle scattering approach. Furthermore, each single scattering was found to be completely determined by the particle size in comparison with the wavelength of the incident wave, its shape, its index of refraction, and the particle orientation with respect to the incident polarization.

In spite of the long history of active research in this field, presently there exist few single-particle scattering problems whose solutions are known with sufficient generality and rigor to be useful for practical purposes. Even the recent mathematical solutions for spheroids and cylinders (Asano et. al. 1975; Barber et. al. 1975) require numerical evaluations which are quite cumbersome and costly on the most modern computers. To aggravate the situation, few systematic experimental methods on the study of nonspherical particles other than using microwave techniques are available at present. This is because in addition to the problems of precisely controlling target parameters and orientation, the art of compensating the incident and other unwanted background radiation for the measurement of the true scattered wave is rather difficult.

The paucity of relevant published data motivated this compilation of microwave-scattering results which provide empirical information on how nonspherical particles scatter light waves.

II. EXPERIMENTAL METHOD

It follows from the principle of electrodynamic similitude (Stratton, 1941) that identical scattering patterns are obtained in two different single-particle scattering processes if the particle size and wavelength differ in such a way that the ratio size/wavelength (x) is the same. This principle provides a means to study the manner in which micron-size particles scatter visible light. By scaling up both the particle size and the wavelength by a factor $\sim 10^5$, while keeping the refractive index of the particle constant, one can study the same single-particle scattering process in the microwave region where all essential parameters that characterize the scattering may be brought under much more precise control.

The microwave analog method used here has been developed over the past two decades. (Greenberg, Pedersen & Pedersen, 1960; Lind et. al., 1965; Lind, 1966; Wang, 1968; Wang et. al., 1977)

Critical steps in this effort and useful symmetry relations employed therein will be outlined in the following subsections.

A. Scattering Quantities, Symmetry Relations and Other Theoretical Considerations

The notations of van de Hulst (1957) are generally used to describe the scattering quantities. The four elements of the scattering amplitude matrix $\tilde{S}$, all dimensionless complex numbers, relate the complex amplitude of the incident wave

$$\vec{E}_o = \begin{pmatrix} E_{l_o} \\ E_{r_o} \end{pmatrix}$$

and the scattered wave

$$\vec{E} = \begin{pmatrix} E_l \\ E_r \end{pmatrix}$$

in the following way:

$$\vec{E} = \frac{e^{-ikr+ikz}}{ikr} \tilde{S} \cdot \vec{E} = \frac{e^{-ikr+ikz}}{ikr} \begin{pmatrix} S_2 & S_3 \\ S_4 & S_1 \end{pmatrix} \begin{pmatrix} E_{l_o} \\ E_{r_o} \end{pmatrix} \qquad (1)$$

where $k = |\vec{k}_o| = 2\pi/\lambda$, λ = wavelength, and the time factor $e^{i\omega t}$ is omitted. Suffixes l and r denote the components of the electric field parallel and perpendicular to the scattering plane, which is formed by the incident and scattered rays. The observation point P is at a distance r from the scatterer located at the coordinate origin (See Fig. 1). It is assumed that r is very large compared to λ and to the size of the particle. In Fig. 1, the yz plane is chosen to be the scattering plane (a horizontal plane in the laboratory), and $\vec{E}_o$ is polarized along the x axis (vertical in the laboratory); i.e., $E_{l_o} = 0$. In this case only the elements S_1 and S_3 are needed. They are proportional, respectively, to the components of the complex amplitudes of the scattered wave parallel and perpendicular to the incident polarization. If, instead, $\vec{E}_o$ were polarized along the y axis, i.e., $E_{r_o} = 0$, only the elements S_2 and S_4 would be needed.

The phase lag ϕ_j of the scattered wave components with respect to the direct ray path via target to P is then

$$\phi_j = \frac{\pi}{2} - \sigma_j \quad \text{where} \qquad S_j = |S_j| e^{i\sigma_j} \quad j=1,2,3,4 \qquad (2)$$

The principal intensity components of the scattered wave, all dimensionless positive numbers, are defined as

$$\begin{aligned} i_1 &= |S_1|^2 \\ i_2 &= |S_2|^2 \end{aligned} \qquad (3)$$

For forward scattering ($\theta = 0^o$) the optical theorem (Feenberg 1932, Montroll & Greenberg 1954, Hulst 1946, 1957) relates the extinction cross section C_{ext} to S_1 by

$$C_{ext} = \frac{4\pi}{k^2} \operatorname{Re}\{S_1\} = \frac{4\pi}{k^2} |S_1(0)| \sin\phi_1(0) \qquad (4)$$

Other useful symmetry relations for an axially symmetric particle are given by (Greenberg, et. al., 1963; Wang, 1968):

$$\begin{aligned} S_1(\chi,\psi) &= S_{\chi E}\cos^2\psi + S_{\chi H}\sin^2\psi \\ S_2(\chi,\psi) &= S_{\chi E}\sin^2\psi + S_{\chi H}\cos^2\psi \\ S_3(\chi,\psi) = S_4(\chi,\psi) &= (S_{\chi H} - S_{\chi E})\cos\psi\sin\psi \end{aligned} \tag{5}$$

where $S_j(\chi,\psi)$ are the complex amplitudes corresponding to the orientation angle (χ,ψ) as shown in Fig. 1. $S_{\chi E}$ and $S_{\chi H}$ are the complex amplitudes when the symmetry axis, tilted by an angle χ from the incident direction, is in the k-E (xz plane in Fig.1) and the k-H (yz plane in Fig.1) plane respectively. Immediate application of Eqs. (4) and (5) gives the extinction cross section $C_{\chi\psi}$ for an axially symmetric particle at an arbitrary orientation (χ,ψ):

$$C_{\chi\psi} = C_{\chi E}\cos^2\psi + C_{\chi H}\sin^2\psi \tag{6}$$

From the first of Eqs. (5) it follows that

$$S_1(\chi,\psi) - S_{\chi E} = (S_{\chi H}-S_{\chi E})\sin^2\psi \tag{7}$$

Thus, if χ is fixed and ψ is varied, the difference vector between the variable vector $S_1(\chi,\psi)$ and the constant vector $S_{\chi E}$ is always parallel to the constant vector $(S_{\chi H}-S_{\chi E})$ and the magnitude of the former is $\sin^2\psi$ times that of the latter; i.e., the tip of $S_1(\chi,\psi)$ should trace a straight line in the actual experimental plot. (Note: In the X-Y recorder plot or P-Q plot in this report, P and Q are proportional to the in-phase and the 90° out-of-phase components of $S_1(\chi,\psi)$ with respect to the incident wave.) This provides a quick check on the accuracy/consistency of the experimental data.

Interesting results may further be inferred from these symmetry relations about the averaged forward-scattering quantities over random orientations. Thus the random average of $C_{\chi\psi}$ in Eq. (6) gives

$$\begin{aligned} \langle C_{\chi\psi}\rangle &= \frac{1}{4\pi}\int_0^{2\pi} d\psi \int_0^{\pi} \sin\chi\, d\chi\, (C_{\chi E}\cos^2\psi + C_{\chi H}\sin^2\psi) \\ &= \frac{1}{2}\int_0^{\pi/2} \sin\chi\, d\chi\, (C_{\chi E} + C_{\chi H}) \end{aligned} \tag{8}$$

Likewise, the averaged forward-scatter intensity $\langle i_1\rangle$ (or $\langle i_2\rangle$) over radam orientations is, from Eqs. (3) and (5),

$$\langle i_1\rangle = \frac{1}{4\pi}\int_0^{2\pi} d\psi \int_0^{\pi} \sin\chi\, d\chi \left| S_{\chi E}\cos^2\psi + S_{\chi H}\sin^2\psi \right|^2 \tag{9}$$

If we assume $S_{\chi E}$ and $S_{\chi H}$ are equal in phase, as is approximately true from the experimental plots (Greenberg et. al. 1963), we have

$$\langle i_1\rangle \simeq \frac{1}{4\pi}\int_0^{2\pi} d\psi \int_0^{\pi} \sin\chi\, d\chi \left| |S_{\chi E}|\cos^2\psi + |S_{\chi H}|\sin^2\psi \right|^2$$

so

$$\langle i_1\rangle \simeq \frac{1}{4}\int_0^{\pi/2} \sin\chi\, d\chi \left\{ |S_{\chi E}|^2 + |S_{\chi H}|^2 + \frac{\left[|S_{\chi E}| + |S_{\chi H}|\right]^2}{2} \right\} \tag{10}$$

An identical expression holds also for $\langle i_2\rangle$

B. Experimental Considerations

An ideal scattering laboratory should simulate the following conditions:

1. The scatterer is to be illuminated <u>only</u> by a distant light source.
2. The detector should "see" only the primary scattering from the target, not the incident beam or reflections from the laboratory enclosure.

Condition 1 implies that the wave front as the target site be flat, both in amplitude and in phase. Design of an indoor laboratory to meet this condition is rather difficult and is still controversial (Silver, 1949, 1962; Beard et. al., 1962; Hansen et. al., 1959; Rhodes 1954; Lind 1966; Wang 1968).

To approximate a flat wave front from a spherical wave front from a microwave antenna, or to receive a scattered wave as though it came from a large distance, the antenna and the target should be separated at least by a distance:

$$R_{min} \gtrsim \frac{2D^2}{\lambda}$$

where D is the diameter of the antenna. A large D places impractical demands on R_{min} for indoor experiments, while if D is made too small, the resulting increase of the beam width would increase unwanted background signals, violating condition 2. Thus a compromise had to be made and we chose $\sim \frac{1}{2}R_{min}$ for the actual target-antenna separations. The results of $\theta=0^\circ$ measurements and wave front examinations (Lind et. al. 1965; Lind, 1966; Wang, 1968: Wang, et. al., 1977) indicate, however, that up to size $x \simeq 21$ the error due to the finite range is less than $\sim 5\%$ in $|S(0)|$ and $\sim 8^\circ$ in $\phi(0)$ if the ratio $i(\pi)/i(0)$ of the target is less than $\simeq 2\%$ (target-antennae multiple reflection error). The error seems to increase for higher θ's but in much more moderate way than was expected.

C. Remarks on Microwave and Electronic Circuitry

In Figs. 2-4 we show the two measurement set-ups from which the data in this report were obtained. Notice that in Figs. 2 and 3, both forward scattering measuring device differ only in size and structure of the laboratory building and hence in the antenna parameters, ranges height of target-site and absorber placement. The laboratory shown in Fig. 2 was used until 1968 with target height H=1.98 meters above the floor level while that in Figs. 3 and 4 was employed until 1970 with H=2.44 meters.

In all cases, linearly polarized CW(continuous wave) microwave radiation of $\lambda = 3.18$ cm was used to illuminate the target. A frequency-stabilized klystron oscillator served as a source, and the incident wave was transmitted via a dipole-disk fed parabollic reflector antenna to provide a tight beam with small side lobes. A similar antenna served as a receiver to accept the scattered wave. The antennae were mounted on steel plates bolted onto laboratory walls or on sturdy scaffolding, and rigid rectangular waveguides and components were supported on the floor level by wood and other shock-absorbing materials. These measures improved the mechanical and hence the phase stability essential for the compensation technique.

For $\theta = 0^\circ$, the separation of the forward-scattered wave from the much more intense incident wave was accomplished by the compensation (null) technique. In the absence of a target, the direct incident wave was led to a null hybrid junction (Figs. 2,3) and was cancelled by a reference wave fed directly from the transmitter via a separate waveguide. The reference wave could be attenuated (Ψ_0) and phase-shifted (Φ_0) as necessary to cancel the incident wave. As the target was brought into the beam, the off-balance from the already established cancellation is linearly proportional to the forward-scattered signal S(0), whose in-phase and 90° out-of-phase components (P and Q components in Figs. 6A-12D) with respect to the incident wave were displayed on an X-Y recorder. The X- and Y- arms of the microwave circuitry in Figs. 2 and 3 served for this orthogonal separation and for the linear display. The tilt and the scaling of the P-Q coordinates in an actual X-Y recorder plot was provided by a set of standard spheres which were run in quick succession after the target was removed and whose S(0) 's and $\phi(0)$'s were known from Mie theory.

The stability of cancellation during an experimental run is a decisive factor affecting the accuracy of the measurement, of S(0) because the scattered signal is much smaller than both the direct wave D and the reference wave N. The error signal $\delta = D-N$ due to a drift in cancellation will add vectorially to S(0) at the null hybrid junction, resulting in the detected signal $S(0)+\delta$ instead of the desired true scattered signal S(0). Therefore, a highly stabilized oscillator was used, and extreme care was exercised in maintaining the mechanical stability of the circuitry. Many experimental runs, particularly for the small targets, were made during the time of maximum temperature stability and minimum power line surges such as during the early morning hours. Also, the location of the null hybrid junction was selected so that the derivative with respect to frequency of the difference between the optical path lengths of the D wave and N wave leading to this junction was zero. Without these precautions, the drift δ was observed to be intolerable especially when small S(0)'s were measured (Wang, 1968).

Fig. 4 shows the circuit schematic employed for angular distribution measurements. A shortage of equipment, mechanical structures and absorbers during the period before 1970 made the compensation technique impossible to perform. Nevertheless, it was possible to see the correct side-scattering by nonspherical particles for a range of θ in which the background radiation was relatively small. In addition to a 4.6m x 4.8m absorber screen behind the fixed receiver antenna at $\theta = 0^\circ$, which is intended to reduce the reflection due to the main and the first side robes of the transmitted beam, belts of absorbers were placed on some critical portions of the side wall in the main reception cone of the movable receiving antenna. By sweeping the receiver, it was observed that over angular intervals $38^\circ \leq \theta \leq 125^\circ$, $127^\circ \leq \theta \leq 140^\circ$, $143^\circ \leq \theta \leq 148^\circ$ and $150^\circ \leq \theta \leq 160^\circ$ the background level were near or below the noise level of the amplifier of the polarization of the radiation is vertical; but a larger background was observed for the horizontal polarization, the levels of which at some θ's are shown by NT in Fig. 13B.

At θ's other than 0, only the principal intensity measurements (i_1 and i_2) were made. The electronic circuitry is therefore much simpler than in the $\theta = 0^\circ$ scattering; the received wave was modulated, fed to a good square-law detector, amplified (40dB) and coherently detected to produce a D.C. voltage proportional to i_1 and i_2 before the display on the y-axis of an X-Y recorder.

D. Target Orientation and Positioning Device

The present orientation device is as described in Lind's thesis (1966). The objective is to construct a device that:

1. Contributes little to the secondary scattering.
2. Quickly, accurately and reproducibly positions an arbitrary target to any given orientation.

The present mechanism meets these criteria. It is remotely operated through 3 potentiometer settings which control the hoist-drop, azimuth, and elevation positions. To expedite the data-gathering, azimuth and elevation detector circuits were later added to read the orientation electronically. The drawbacks to this system are:

1. Considerable patience is needed in handling control strings due to their susceptibility to entangling and breakage.
2. Target height in the beam is slightly target-size dependent.
3. The elevation angles are not linearly related to the potentiometer settings.
4. The process of manual control is time-consuming when an average over all spatial orientations is required.

E. Scatterers and Their Properties

The preparation of targets and the determinations of their refractive-index require considerable time and effort. Early attempts to simulate elongated dielectric particles in interstellar space led us to fabricate spheroidal particles from commercial plastics. Among a variety of materials, two low cost thermoplastics were found to possess stability, machinability, the possibility for molding and refractive indices compatible with those currently suggested for interstellar grains.

The first plastic is called the polymethyl methacrylate, acrylic plastic or sometimes lucite (Dupont's trade name). This material has a refractive index in the microwave region which is close to that of silicates in the optical region. A number of prolate and obtate spheroids of elongation ratios $b/a = 2$ and $b/a = 0.5$, respectively, were machined from commercial blocks.

The second plastic is expandable polystyrene, supplied by Sinclair-Koppers Co. under the trade name Dylite F-40, which consists of small beads about 0.5mm in diameter, each with ~7% impregnated volatile material to help expansion when heated. A proper amount of such beads will expand and fuse to each other when-heated in an enclosed cavity, transforming them into a strong, smooth-skinned foam filling the mold cavity. A number of spheroidal and cylindrical targets were thus fabricated in a series of cement or glass-tube molds of various sizes. Since the dielectric constant, and hence the refractive index, of such material depends only on its density, one can control the refractive index of the product target beforehand. To prepare homogeneous targets of lower density, however, it was found essential to pre-expand these beads in a separate rotating heat chamber to near desired density prior to molding. Another advantage of molding such plastics is that one can introduce absorption (the imaginary part of refractive index) by admixing these beads with such material as carbon dust before molding.

In Figs. 5A-5C we show 3 basic target shapes studied. In particular, Fig. 5C shows a rough-sphere model in which 6 dylite cylinders of equal length symmetrically surround a longer center dylite cylinder. Each target is assigned a 6-digit ID number; the first 3 digits denote the series while the second 3 denote the number in that series.

The complex refractive index: $m=m'-im''$ of acrylic scatterers (Tables I & V was obtained from the average of a number of complex dielectric constant ($\epsilon=\epsilon'-i\epsilon''$) measurements on waveguide samples prepared from the same commerc supply, using the standing wave technique of Roberts and von Hippel (1946) its technical development in this laboratory (see also Sucher, Ed., 1963).

For carbon-dylite-mixture targets (004- and 005- series, Table III), the same technique was applied to a number of separately prepared waveguide samples of the same mixing ratio. Appreciable variations of m(m' up to ~8%, m'' up to ~40%) as well as density (d) were observed primarily due to the difficulties involved in preparing samples of homogeneous isotropic mixtures. Targets selected in this report have overall density near 0.445 grams/cm^3, which corresponds to $m=1.33-i0.05$. It was impractical to measure ϵ values for all expanded-dylite targets of low-loss (001-, 002-, 003- and 020-series; Tables I-IV). Instead, a number of waveguide samples covering a wide range of density were prepared and the ϵ value measured for each. Despite a fair amount of scatter in the imaginary part of m ($m''=0.005\pm 0.002$), the real part of m was almost on a straight line when plotted against the density of these samples. Values of m' listed in Tables I-IV were therefore obtained from this straight line by finding the density of the target through volume and weight measurements.

III. EXPERIMENTAL PLOTS AND EXPLANATIONS

Numerous experimental results derived from the methods described in the previous section have been obtained. Out of these we selected some typical results on spheroidal and rough-particle scatterers which are of possible immediate interest.

Because of the distinct difference in the operational procedures, the results are divided in two parts, i.e., the forward-scattering and the angular distribution.

A. Forward Scattering, $\theta=0^{\circ}$

Each experimental X-Y recorder plot (or P-Q plot) of the complex forward-scattering amplitude S(0) parameterized by the orientation angle χ, for each one of the targets whose characteristics are tabulated in Tables II-IV, are reproduced in Figs. 6A-12D as solid curves.

For an axially symmetric particle such as a spheroid, S(0) of an arbitrarily oriented target may be obtained from a linear composition of those obtained as the axis of the target is rotated in two perpendicular planes, the k-E plane and the k-H plane. These planes contain the propagation vector $\vec{k}_o$ and the electric ($\vec{E}_o$) and magnetic ($\vec{H}_o$) vector of the incident radiation respectively(Cf II-A). Two solid curves in each P-Q plot for spheroids show the χ dependence of S(0) when the axis is swept in these two principal planes. Each fiducial point along the curve marks the value of χ, and in particular, k, E and H denote, respectively, the cases in which the axis is parallel to $\vec{k}_o$, $\vec{E}_o$ and $\vec{H}_o$

For a rough particle (Fig. 5C) which lacks a complete cylindrical symmetry, k, E and H denote, respectively, the orientations in which a particle-fixed plane containing the particle axis and the largest geometrical cross-section is parallel to $\vec{k}_o$-$\vec{H}_o$, $\vec{E}_o$-$\vec{H}_o$ and $\vec{k}_o$-$\vec{H}_o$ planes, in addition to that the axis itself being parallel to $\vec{k}_o$, $\vec{E}_o$ and $\vec{H}_o$. In the E orientation, a 30° rotation about the particle axis yields the orientation marked e on Figs. 11A-12D.

The vector drawn from the origin of each P-Q plot to each χ-mark along the solid curves is therefore the cartesian representation of S(0) at that target orientation χ, and the tilt of this vector from the P-axis is the phase lag of the forward-scattered wave at χ. The absolute magnitude of S(0) at each χ is found by comparing the length of this vector with that of the standard sphere during the same experimental run, whose S(0) is shown in the same plot, and whose magnitude is listed in Table I.

The projection of each such S(0) vector on the Q-axis is (according to the optical theorem, Eq.(4), Section II-A) proportional to the extinction cross-section C_{ext} at that χ. The Q-axis is calibrated in units of extinction efficiency $Q=C_{ext}/A$; where A is the geometrical cross section perpendicular to the axis for a spheroid, or that of an equal-volume sphere for a rough particle.

These P-Q plots were selected out of a number of similar experimental runs for various sizes of spheroids based on the reliability of the target-parameter measurements, stability of the compensation under which the experiments were performed, and target sizes to span a range near the first resonance in extinction curves.

B. Angular Distribution $40^\circ \lesssim \theta \lesssim 150^\circ$

Dependence of scattering intensities $i_1(\theta)$ and $i_2(\theta)$ on the scattering angle θ , as measured by the method in II-C are shown in Figs. 13A-22A. Suffixes 1 and 2 in $i_1(\theta)$ and $i_2(\theta)$ denote, respectively, the cases when both polarizations of the transmitting and receiving antennae are vertical and horizontal (Cf II-A).

Figs. 13A-13D are for an acrylic sphere #137, which has also been used extensively as a standard to provide calibrations. These measurements provide a consistency check, and the results of Mie theory prediction using the appropriate parameters of this sphere, x=4.978 & m=1.610, are also included. Experimental values are normalized at $\theta=90^\circ$. Each of Figs. 13B-13D; all for i_2, differs from each other only in the way of absorber placement and in the angular intervals of θ for which the measurements were taken. In particular, HT's in Fig. 13B indicate the received intensity levels in the absence of the target (the background intensity) for that polarization from which specular reflection from the laboratory floor and wall is more likely to occur.

Figs. 14A-19B are the results for 6 acrylic prolate spheroids whose characteristics are also tabulated in Table V. At each θ, intensity measurements were made for 3 principal target orientations k, E and H, the orientations in which the particle axis is parallel to $\vec{K}_o$, $\vec{E}_o$ and $\vec{H}_o$ of the incident wave, respectively. For each target, Mie theory predictions of $i_1(\theta)$ or $i_2(\theta)$, multiplied by a factor 4 for a sphere whose radius is equal to the semi-minor-axis of the spheroid and whose refractive index is m=1.610, are also included in the appropriate figure.

Figs. 20A-22A show the $i_1(\theta)$'s and $i_2(\theta)$'s for 3 rough particles made of expanded polystyrene (Cf also Table IV). Lack of cylindrical symmetry and homogeneity complicates the target-orientation dependence of i's considerably, and only 4 to 5 principal orientations were considered in the data-taking. The same notation as in forward-scattering (III-A) is used to indicate the target orientations, k, E, and H. Suffixed notations such as E_k and E_H are needed here, however, to indicate whether this E was attained from the k or H orientation initially. Orientation symbols such as e_{E_H} (Fig. 21A) denotes that orientation reached from the E_H orientation by a 30° azimuthal rotation. Similarly, h_{H_E} results from 30° azimuthal rotation around H_E (Fig. 21B). Mie theory predictions of i_1, i_2 of an equal-volume sphere with the same index of refraction as the target are also included in each figure.

IV. DISCUSSION AND ANALYSIS

A. On Spheroidal Particles

The P-Q experimental plots of forward scattering ($\theta=0^\circ$), as displayed in Figs. 6A-10E provide detail on the subtle target-orientation dependence of the scattered wave. They provide the phase shifts (ϕ_E, ϕ_H), the extinction efficiencies (Q_E, Q_H), the polarization by extinction $P=(Q_E - Q_H)/(Q_E + Q_H)$ and other pertinent scattering data. The subscripts E and H denote the case when the particle-symmetry axis is swept in the k-E plane and the k-H plane, respectively. (Cf Sec. II-A).

If we fix our attention to a particular group of spheroids in which the refractive index m is relatively constant (say #001 series, Figs. 6A-6E), and also to a particular orientation (say E), we notice that the tip of the S(0) vector will make a clockwise rotation in the P-Q plot as we increase the particle size. For a given target, orientation changes from E to k or H to k causes a similar rotation. van de Hulst (1957) attributes this to an anomalous diffraction effect due to the increased ray path of the penetrating incident wave before it is scattered forward. For spherical particles, a theoretical P-Q plot as function of size x for m=1.365 is shown in Fig. 23A, using Mie theory. In Fig. 23B, we show a similar theoretical P-Q plot for infinite dielectric circular cylinders with m=1.2664 at perpendicular incidences in which E and H distinguish the cases when the cylinder axis is parallel to $\vec{E}_o$ and $\vec{H}_o$ vectors of the incident wave, respectively.

For the purpose of explaining the subtle orientation of S(0) displayed in these previous P-Q plots of spheroids, there are a few approximation methods based on Mie theory for spheres which replace the actual spheroid under investigation by a set of appropriate equivalent spheres (Greenberg, 1974; Latimar, 1975). Because these approximation methods are based on sphere models, it is not immediately apparent whether they can provide useful results to explain, in particular, the polarization by extinction by these spheroidal particles.

Instead, we report here an approximation based on the rigorous infinite cylinder solution (Lind et. al., 1966), and replace the actual spheroid by a section of an appropriate infinite cylinder. This is because, as follows from Fig. 23B. the cylinder approach appears to be the most tractable way to qualitatively account for the polarization. We replace the spheroid by a finite cylinder whose volume, refractive index and the elongation ratio are the same. We further assume that the scattered field from this finite cylinder can be estimated from that of the infinite cylinder solution. The normalization area needed to deduce the Q's (the extinction efficiencies) is taken to be the base of the cylinder. The results of numerical calculation using this method are also shown in Tables VIA-VIF and are to be compared with the experimental results for some appropriate spheroids. We note from these comparisons that Q's by this cylinder model somewhat overestimate the magnitude, but the polarization by extinction and the forward phase shift agree fairly well especially near perpendicular incidence. It also appears that the cylinder approximation progressively improves as the size of the spheroid increases. Away from the perpendicular incidence. the cylinder approximation becomes progressively poorer; at $\chi=0^\circ$ the infinite cylinder theory predicts $Q=0$. (The theoretical results at edge-on incidence are therefore not tabulated). A duplicate of Fig. 6C, the P-Q experimental plot for the spheroid #001010 (See also Table VIB), with the added cylinder theory prediction, is displayed in Fig. 24 for direct comparison. For strongly absorbing (lossy) prolate spheroids (#004-series), similar comparisons and results hold except that for the smallest target (#004001) the assigned value of complex refractive index is subject to some error due to the difficulties involved in the process of fabricating small homogeneous targets of the carbon-dylite mixture.

Angular distribution results for spheroidal particles, as displayed in Figs. 14A-19B, show how these elongated particles side-scatter light waves. A number of experimental difficulties were encountered when these data were taken. These difficulties included: (1) Not enough absorbers were available to reduce the background radiation, (2) Poor mechanical and geometric conditions: floor irregularities (up to ~5. cm variation) displaced the antenna cart which is mechanically coupled to the orientation mechanism through a relatively slender aluminum frame; (3) Lack of sufficient microwave components to perform the cancellation technique, (4) Some of the electronic instruments employed such as the lock-in amplifier-detector had insufficient sensitivity to read small received signals; hence linear scaling was employed to plot i_1 and i_2 instead of the widely used logarithmic scaling.

In spite of these difficulties the target parameters, orientation and other factors could be controlled much more precisely than is possible for any other known method of experimental investigation. (Target parameters are shown in Table V, Orientations are as described in II-A and figure captions).

Attempts were first made to concentrate on some principal target orientations with respect to the transmitting and the receiving antenna polarizations. i_1 and i_2 in Figs. 14A-19B denote, respectively, the scattering intensities when both the transmitting and receiving antennas are vertically and horizontally polarized. k, E and H are the target orientations in which the target axis is parallel to $\vec{k}_0$, $\vec{E}_0$ and $\vec{H}_0$ of the incident wave vectors, respectively. This choice was made on the intuition that from these principal orientations, the experimental angular distribution data could be analyzed most easily in comparison with Mie theory for appropriately sized spheres. In particular, for the E or H orientation, the target presents a geometrical cross section that is the sum of two identical spheres whose radii are equal to the semi-minor axis of the spheroid. In addition, these two spheres have their total volume equal to the volume of the spheroid itself. If these two spheres scatter the radiation independently but coherently, the total scattering intensity would be 4 times that of an individual sphere and might resemble that by the spheroid at these orientations. The scattering intensities i_1 and i_2 from this sphere as computed by Mie theory and multiplied by 4 are shown in each figure. The comparisons reveal that for i_1 at E orientations and for smaller sizes, the scattering intensity is roughly 2 times that of the sphere with similar angular distribution patterns. Beyond this normalization factor, the comparison between the sphere and the spheroid does not seem to correlate in either total brightness or polarization over the range of scattering.

Further comparisons based on infinite cylinder theory were made in an attempt to obtain a better explanation of the spheroid angular signature. With the same refractive index as the spheroids, the equivalent cylinder sizes were chosen as in the previous forward-scatter comparisons. Figs. 25A-26B show such comparisons on two spheroids #100009 and #100019 with appropriate cylinder sizes $x_C=2.190$ and $x_C=4.026$ respectively. Since the cylinder theory uses the axis as one of the principal coordinates, which matches the present laboratory coordinates only at two orientations, it is feasible at this moment only to compare i_1 at E orientation and i_2 at H orientation for the experimental and theoretical data. For #100009 (Cf. Figs. 25A-25B) this cylinder model approximates the actual angular distribution fairly well in shape but not in magnitude. For the larger spheroid, #100019, (Cf. Figs. 26A-26B) the correlation still exists between the spheroid and the infinite cylinder except that the peaks predicted by the cylinder theory are shifted by a considerable amount. The cylinder does not appear to be a reliable basis for predicting angular scattering by spheroidal particles. A final possibility, yet to be explored, is the conjecture that the angular distribution from a spheroid may be deduced from equivalent spheres where each angle corresponds to a different sphere (Greenberg, 1974).

B. On Rough Particles

The experimental P-Q plots for rough dylite particles as shown in Figs. 11A-11D, as well as for the totally reflecting rough particles in Figs. 12A-12D, suggest the complexity of the dependence of forward-scattered wave on target parameters and orientations. They bear little resemblance to the P-Q plots of previous spheroidal particles or to those which have a more defined non-sphericity, and present an awesome barrier to a predictable explanation.

Even though these particles have no complete axial symmetry, they have mirror symmetry with respect to 7 planes. One such plane passes through the center of the particle and is orthogonal to the axis; the other 6 planes, all containing the particle axis, have equal angular separation of 30° from the neighboring ones. How this mirror symmetry can reduce the amount of data needed for the complete description of orientation dependence of S(0) or help to evaluate the extinction cross-section averaged over random orientations (Cf. Eq. (8). Sec. II-A) is not presently known. For this reason, the orientations in the P-Q plots are not exhaustive. We have not yet investigated how much deviation from a straight line in a P-Q plot would result by going from the E to the H orientation (Cf. Eq. (7), Sec. II-A) because of the incomplete axial symmetry of each particle. Nevertheless, for penetrable dylite particles (#020-series) there is a definite trend indicating that as we decrease the particle size (by going from Fig. 11A to Fig. 11D), the percentage variation of S(0) is also reduced, both in the P and Q-components; i.e., the variation of extinction efficiency due to the orientation change is reduced. Also, the forward phase shifts as we go from the k orientation to either E or H orientation are also increased. This suggests extending the eikonal approximation (Greenberg 1960; Greenberg, 1968; Wang et. al., 1976) to this kind of rough particle. The totally reflecting rough particles (Figs. 12A-12D) do not seem to have the above distinct features.

The overall size dependence of extinction by these rough particles and comparison with appropriate smooth spheres has been reported previously (Greenberg et. al., 1971). Similar comparison based on cylinder theory has also been published (Shah. et. al., 1972). This report gives a more detailed account of the phenomena for some of the separate particles.

Little analysis can be made on the angular distribution by rough particles as displayed on Figs. 20A-22A beyond the explanations described in Sec. III-B presently. The particles do not possess complete cylindrical symmetry and are possibly not perfectly homogeneous. The effects of target non-homogeneity are not very serious in the $\theta=0^o$ scattering, but show marked variation in scattering intensity at higher θ's (Wang, 1968). In addition, only a limited number of orientation changes were possible at each θ where these data were taken. Thus, the averaged intensities over random particles orientations are impossible to evaluate. Qualitatively, however, it seems that a rough particle will scatter more light in smaller θ's and less in larger θ's as compared to a smooth sphere of the equal volume.

V. SUMMARY REMARKS

We have presented some hitherto unpublished facts on the scattering by spheroidal and rough particles based on microwave measurements. We believe these results contain some experimental errors, but are nevertheless superior in precision to any known method other than microwave techniques at present, especially in the $\theta=0^o$ scattering and particularly for the rough particles.

Symmetry relations existing in the scattering process (Sec. II-A), which are independent of the target material and which proved very useful in the forward-scattering, should be studied and extended to other scattering angles θ. This is useful not only for expediting the data-gathering, but also to check the consistency or accuracy of measurements on particles possessing axial, mirror or other geometrical symmetries.

In extinction measurements, spheroidal particles polarize light depending upon the particles orientation. For the size range investigated, the degree of polarization decreases with size. In particular, for the prolate spheroids near perpendicular incidence to the axis, the degree of polarization can be fairly well estimated by infinite cylinder scattering theory using appropriately sized cylinders. In this regard, scattering by finite cylinders needs to be investigated to complete the comparison and to cover the flattened particles such as oblate spheroids.

To avoid the chaotic accumulation of scattering data for particles of infinite variety of nonsphericity, judicial selection and classification of targets for experiment, and systematic catalogue of such data are essential.

Table I. Characteristics of spherical targets used as standards to calibrate and check the 3.18 cm microwave scattering measurements. $S(0)_{Mie}$ and $\phi(0)_{Mie}$ are respectively the amplitude and the phase shift of the scattered wave at $\theta = 0^\circ$, as predicted by Mie theory.

Sphere	Radius	$x =$	Material	Refractive Index		$S(0)_{Mie}$	$\phi(0)_{Mie}$
ID No.	a (cm)	$2\pi a/\lambda$		Re{m}	Im{m}		(degrees)
#1	2.529	4.993	Expanded Polystyrene	1.267	-0.005 ±0.002	21.38	54.6
#2	2.712	5.354	"	1.247	"	24.08	54.4
#4	3.162	6.241	"	1.258	"	36.06	66.6
#12	3.848	7.594	"	1.152	"	42.33	48.1
#13	2.166	4.276	"	1.254	"	13.57	43.8
#251	2.155	4.253	"	1.130	"	7.037	21.8
#256	3.813	7.525	"	1.157	"	42.34	49.2
#137	2.522	4.978	Acrylic	1.610	-0.004	19.54	113.8

Table II. Parameters of the low-loss prolate spheroids of elongation ratio $b/a = 2$, used for the microwave measurements in this report. These particles were prepared by molding expandable polystyrene (Sinclair-Koppers Dylite F 40) in cement molds of varied sizes. Each target is also assigned two size parameters $x = ka$ and $x_v = ka_v$, where a_v is the radius of the equal-volume sphere.

Target	Shape & Size			Refractive Index		$x = ka$	$x_v = ka_v$
ID No.	Figure	a (cm)	b (cm)	$\mathrm{Re}\{m\}$	$\mathrm{Im}\{m\}$		
#001002	5A	1.362	2.724	1.264	-0.005 ±0.002	2.688	3.389
#001007	5A	1.888	3.776	1.266	"	3.726	4.694
#001010	"	2.228	4.456	1.270	"	4.397	5.539
#001015	"	3.020	6.040	1.269	"	5.960	7.510
#001020	"	4.092	8.184	1.263	"	8.076	10.175
#002003	"	1.480	2.960	1.109	"	2.921	3.680
#002007	"	1.889	3.778	1.109	"	3.747	4.722
#002015	"	3.080	6.160	1.108	"	6.078	7.659
#002020	"	4.092	8.184	1.110	"	8.076	10.175
#002022	"	4.500	9.000	1.111	"	8.881	11.190
#003004	"	1.588	3.176	1.361	"	3.134	3.949
#003107	"	1.914	3.828	1.371	"	3.778	4.759
#003108	"	2.007	4.014	1.374	"	3.961	4.991
#003109	"	2.111	4.222	1.372	"	4.166	5.249
#003010	"	2.230	4.460	1.370	"	4.401	5.545

Table III. Characteristics of lossy prolate and oblate spheroids of elongation ratios b/a=2 and b/a=0.5 respectively, in this report. These particles were prepared by admixing carbon dust(lamp black) and expanded polystyrene beads(Sinclair-Koppers Dylite F 40) in the weight proportion 0.025 to 1.0, and molding the homogeneous mixture in cement molds of various sizes. Two size parameters $x = ka$ and $x_v = ka_v$ for each target are also shown, where a_v is the radius of the equal-volume sphere.

Target ID No.	Shape & Size Figure	a (cm)	b (cm)	Refractive Index Re $\{m\}$	Im $\{m\}$	$x = ka$	$x_v = ka_v$
#004001-	5A	1.161	2.322	1.33	-0.05	2.291	2.887
#004003	"	1.473	2.946	"	"	2.907	3.664
#004011	"	2.352	4.704	"	"	4.642	5.849
#004215	"	3.026	6.052	"	"	5.972	7.297
#004017	"	3.389	6.778	"	"	6.689	8.428
#005010	5B	1.803	0.902	"	"	3.558	2.824
#005018	"	2.983	1.492	"	"	5.888	4.673
#005020	"	3.376	1.688	"	"	6.664	5.289
#005024	"	4.175	2.088	"	"	8.241	6.541
#005032	"	5.780	2.890	"	"	11.408	9.054

Table IV. Characteristics of rough particles in this report. The first group(#020 Series) is prepared by stacking 7 expanded polystyrene (Sinclair-Koppers Dylite F 40) cylinders. The second group(#030 series) is prepared by coating the similar stack by aluminum foils of 0.0025cm thickness. For each target, the size parameter $x_v = ka_v$, where a_v is the radius of the equal-volume sphere, is also shown.

Target	Shape & Size				Refractive Index		$x_v = ka_v$
ID No.	Figure	2a (cm)	l_1 (cm)	l_2 (cm)	Re $\{m\}$	Im $\{m\}$	
#020001	5C	2.75	8.25	5.65	1.356	-0.005, ±0.002	7.717
#020002	"	2.20	6.56	4.35	1.362	"	6.108
#020003	"	1.55	4.64	3.09	1.354	"	4.314
#020004	"	1.28	3.84	2.53	1.333	"	3.554
#030001	"	2.78	8.40	5.58	∞ (Totally reflecting)		7.756
#030002	"	2.19	6.55	4.40	"		6.107
#030003	"	1.56	4.65	3.08	"		4.329
#030004	"	1.28	3.73	2.59	"		3.570

Table V. Characteristics of prolate spheroids of elongation ratio b/a=2 in this report. These particles were prepared by machining commercially available acrylic material. For each target, two size parameters $x = ka$ and $x_v = ka_v$ are also shown. a_v is the radius of the equal-volume sphere.

Target	Shape & Size			Refractive Index		$x = ka$	$x_v = ka_v$
ID No.	Figure	a (cm)	b (cm)	$Re\{m\}$	$Im\{m\}$		
#100009	5A	1.270	2.540	1.610	-0.004	2.507	3.159
#100010	"	1.378	2.756	"	"	2.718	3.424
#100013	"	1.702	3.404	"	"	3.359	4.232
#100015	"	1.902	3.804	"	"	3.754	4.730
#100017	"	2.115	4.230	"	"	4.175	5.260
#100019	"	2.335	4.670	"	"	4.609	5.807

Table VI A

Forward-scatter data for a prolate spheroid of elongation $b/a = 2$ (ID #001002 , refractive index $m = 1.264$) as a function of orientation angle χ. ϕ_E & ϕ_H are phase shifts in degrees, Q_E & Q_H are extinction efficiencies and $(Q_E - Q_H)/(Q_E + Q_H)$ is the polarization by extinction. Subscripts E and H denote, respectively, cases when the symmetry axis is in the k-E plane and in the k-H plane. Corresponding scattering quantities for a section of an infinite circular cylinder which has the same m, the equal volume and the identical elongation ratio as the spheroid; are obtained theoretically from the rigorous infinite cylinder solution and are also tabulated for comparison. $x_c = 2.348$ is the size parameter for this cylinder. The geometricalcross section perpendicular to the axis is used for the evaluation of Q's in both spheroid and cylinder cases.

Data	Item		Target Orientation Angle χ								
		k	10°	20°	30°	40°	50°	60°	70°	80°	90°
ϕ_E	Expt.	38.6			36.3			31.0			28.3
	Theory				50.8			35.6			32.1
ϕ_H	Expt.	38.6			34.0			27.6			24.0
	Theory				44.8			29.8			25.5
Q_E	Expt.	2.69			2.46			2.10			1.98
	Theory				3.65			3.04			2.78
Q_H	Expt.	2.69			2,22			1.81			1.60
	Theory				3.07			2.39			2.10
$\frac{Q_E+Q_H}{2}$	Expt.	2.69			2.34			1.95			1.79
	Theory				3.36			2.72			2.44
$\frac{Q_E-Q_H}{Q_E+Q_H}$	Expt.	0.			0.051			0.072			0.107
	Theory				0.087			0.119			0.139

Table VI B

Forward-scatter data for a prolate spheroid of elongation b/a = 2 (ID #001010 , refractive index m= 1.270) as a function of orientation angle X . ϕ_E & ϕ_H are phase shifts in degrees, Q_E & Q_H are extinction efficiencies and $(Q_E - Q_H)/(Q_E + Q_H)$ is the polarization by extinction. Subscripts E and H denote, respectively, cases when the symmetry axis is in the k-E plane and in the k-H plane. Corresponding scattering quantities for a section of an infinite circular cylinder which has the same m, the equal volume and the identical elongation ratio as the spheroid; are obtained theoretically from the rigorous infinite cylinder solution and are also tabulated for comparison. x_c =3.841 is the size parameter for this cylinder The geometricalcross section perpendicular to the axis is used for the evaluation of Q's in both spheroid and cylinder cases.

Data	Item		Target Orientation Angle X								
		k	10°	20°	30°	40°	50°	60°	70°	80°	90°
ϕ_E	Expt.	85.7	83.8	78.0	68.5	62.0	57.3	53.9	51.9	50.7	50.1
	Theory		134.4	99.7	83.0	70.7	63.4	57.8	54.2	52.4	51.8
ϕ_H	Expt.	85.7	83.1	77.1	68.5	61.0	55.2	51.7	48.5	46.5	46.9
	Theory		135.6	93.3	77.7	67.8	59.3	53.4	49.4	47.4	46.8
Q_E	Expt.	5.48	5.47	5.25	5.06	4.98	4.87	4.79	4.71	4.66	4.73
	Theory		1.67	4.14	5.85	6.43	6.57	6.44	6.34	6.28	6.25
Q_H	Expt.	5.48	5.42	5.25	5.06	4.78	4.62	4.52	4.35	4.26	4.34
	Theory		1.47	3.39	5.54	5.93	5.93	5.78	5.64	5.57	5.54
$\frac{Q_E+Q_H}{2}$	Expt.	5.48	5.44	5.25	5.06	4.88	4.75	4.66	4.53	4.46	4.54
	Theory		1.57	3.77	5.69	6.18	6.25	6.11	5.99	5.92	5.90
$\frac{Q_E-Q_H}{Q_E+Q_H}$	Expt.	0.	0.004	0.000	0.001	0.020	0.027	0.030	0.040	0.044	0.042
	Theory		0.063	0.100	0.028	0.040	0.051	0.054	0.058	0.060	0.060

Table VI C

Forward-scatter data for a prolate spheroid of elongation $b/a = 2$ (ID #001020 , refractive index $m = 1.263$) as a function of orientation angle χ. ϕ_E & ϕ_H are phase shifts in degrees, Q_E & Q_H are extinction efficiencies and $(Q_E - Q_H)/(Q_E + Q_H)$ is the polarization by extinction. Subscripts E and H denote, respectively, cases when the symmetry axis is in the k-E plane and in the k-H plane. Corresponding scattering quantities for a section of an infinite circular cylinder which has the same m, the equal volume and the identical elongation ratio as the spheroid; are obtained theoretically from the rigorous infinite cylinder solution and are also tabulated for comparison. $x_C = 7.055$ is the size parameter for this cylinder. The geometricalcross section perpendicular to the axis is used for the evaluation of Q's in both spheroid and cylinder cases.

Data Item		Target Orientation Angle χ									
		k	10°	20°	30°	40°	50°	60°	70°	80°	90°
ϕ_E	Expt.	151.9	146.2	131.6	119.7	107.5	98.3	92.2	88.5	85.6	85.0
	Theory		76.1	90.4	132.2	120.2	107.2	99.1	93.5	90.1	88.9
ϕ_H	Expt.	151.9	146.7	133.5	119.7	106.8	96.3	92.5	85.0	82.3	81.5
	Theory		76.9	74.8	130.4	117.0	103.5	96.2	90.5	87.5	86.4
Q_E	Expt.	1.36	1.81	3.05	4.11	5.32	6.15	6.75	7.09	7.38	7.34
	Theory		1.86	1.04	2.38	4.56	6.89	8.24	9.12	9.55	9.70
Q_H	Expt.	1.36	1.74	2.66	3.89	5.00	5.48	6.48	6.90	7.09	7.17
	Theory		1.95	1.26	2.41	4.52	6.72	8.03	8.92	9.33	9.46
$\frac{Q_E+Q_H}{2}$	Expt.	1.36	1.78	2.86	4.00	5.16	5.82	6.61	7.00	7.24	7.25
	Theory		1.90	1.15	2.39	4.54	6.81	8.13	9.02	9.44	9.58
$\frac{Q_E-Q_H}{Q_E+Q_H}$	Expt.	0.	0.019	0.067	0.028	0.032	0.057	0.021	0.014	0.020	0.012
	Theory		-0.022	-0.094	-0.005	0.005	0.012	0.013	0.011	0.012	0.013

Table VI D

Forward-scatter data for a prolate spheroid of elongation b/a = 2 (ID #004001- , refractive index m=1.33-i0.05) as a function of orientation angle χ. ϕ_E & ϕ_H are phase shifts in degrees, Q_E & Q_H are extinction efficiencies and $(Q_E - Q_H)/(Q_E + Q_H)$ is the polarization by extinction. Subscripts E and H denote, respectively, cases when the symmetry axis is in the k-E plane and in the k-H plane. Corresponding scattering quantities for a section of an infinite circular cylinder which has the same m, the equal volume and the identical elongation ratio as the spheroid; are obtained theoretically from the rigorous infinite cylinder solution and are also tabulated for comparison. $x_C = 2.001$ is the size parameter for this cylinder. The geometricalcross section perpendicular to the axis is used for the evaluation of Q's in both spheroid and cylinder cases.

Data	Item	Target Orientation Angle χ									
		k	10°	20°	30°	40°	50°	60°	70°	80°	90°
ϕ_E	Expt.	68.0			66.3			59.1			57.7
	Theory				60.3			46.1			43.6
ϕ_H	Expt.	68.0			65.2			53.6			50.8
	Theory				53.2			37.7			34.1
Q_E	Expt.	4.35			4.27			3.69			3.65
	Theory				3.94			3.75			3.64
Q_H	Expt.	4.35			3.98			3.32			3.19
	Theory				3.15			2.91			2.74
$\frac{Q_E+Q_H}{2}$	Expt.	4.35			4.12			3.50			3.42
	Theory				3.54			3.33			3.19
$\frac{Q_E-Q_H}{Q_E+Q_H}$	Expt.	0.			0.035			0.053			0.067
	Theory				0.112			0.127			0.142

Table VI E

Forward-scatter data for a prolate spheroid of elongation b/a = 2 (ID # 004011 , refractive index $m = 1.33 - i.05$) as a function of orientation angle χ. ϕ_E & ϕ_H are phase shifts in degrees, Q_E & Q_H are extinction efficiencies and $(Q_E - Q_H)/(Q_E + Q_H)$ is the polarization by extinction. Subscripts E and H denote, respectively, cases when the symmetry axis is in the k-E plane and in the k-H plane. Corresponding scattering quantities for a section of an infinite circular cylinder which has the same m, the equal volume and the identical elongation ratio as the spheroid; are obtained theoretically from the rigorous infinite cylinder solution and are also tabulated for comparison. $x_C = 4.055$ is the size parameter for this cylinder. The geometricalcross section perpendicular to the axis is used for the evaluation of Q's in both spheroid and cylinder cases.

Data	Item	k	10°	20°	30°	40°	50°	60°	70°	80°	90°
			Target Orientation Angle χ								
ϕ_E	Expt.	105.7	104.4	99.7	94.4	89.5	85.2	82.3	80.7	79.2	78.3
	Theory		131.0	114.5	102.1	91.2	82.8	77.2	73.8	71.7	71.0
ϕ_H	Expt.	105.7	102.7	97.2	91.5	86.1	81.8	78.4	76.1	74.8	74.0
	Theory		125.2	109.8	97.6	85.4	77.2	71.6	68.2	66.3	65.6
Q_E	Expt.	3.91	4.01	4.41	4.86	5.29	5.64	5.88	6.01	6.08	6.09
	Theory		1.18	3.09	4.83	6.07	6.78	7.25	7.48	7.58	7.61
Q_H	Expt.	3.91	4.11	4.46	4.83	5.17	5.40	5.55	5.67	5.72	5.72
	Theory		1.14	2.97	4.42	5.62	6.31	6.74	6.97	7.05	7.08
$\frac{Q_E+Q_H}{2}$	Expt.	3.91	4.06	4.44	4.84	5.23	5.52	5.71	5.84	5.90	5.90
	Theory		1.16	3.03	4.63	5.85	6.54	7.00	7.22	7.32	7.34
$\frac{Q_E-Q_H}{Q_E+Q_H}$	Expt.	0.	-0.013	-0.006	0.004	0.011	0.022	0.028	0.029	0.031	0.032
	Theory		0.016	0.019	0.044	0.038	0.036	0.036	0.035	0.036	0.036

Table VI F

Forward-scatter data for a prolate spheroid of elongation b/a = 2 (ID #004017 , refractive index m = 1.33-i.05) as a function of orientation angle X. ϕ_E & ϕ_H are phase shifts in degrees, Q_E & Q_H are extinction efficiencies and $(Q_E - Q_H)/(Q_E + Q_H)$ is the polarization by extinction. Subscripts E and H denote, respectively, cases when the symmetry axis is in the k-E plane and in the k-H plane. Corresponding scattering quantities for a section of an infinite circular cylinder which has the same m, the equal volume and the identical elongation ratio as the spheroid; are obtained theoretically from the rigorous infinite cylinder solution and are also tabulated for comparison. x_C = 5.843 is the size parameter for this cylinder. The geometricalcross section perpendicular to the axis is used for the evaluation of Q's in both spheroid and cylinder cases.

Data	Item	Target Orientation Angle X									
		k	10°	20°	30°	40°	50°	60°	70°	80°	90°
ϕ_E	Expt.	94.8	95.8	97.7	98.2	97.8	96.8	95.4	94.3	93.5	93.0
	Theory		97.8	106.6	114.8	110.0	104.5	98.6	94.7	92.3	91.5
ϕ_H	Expt.	94.8	95.8	96.8	96.5	95.3	93.7	92.2	90.8	90.1	89.9
	Theory		98.6	102.3	103.0	105.0	100.0	94.2	90.5	88.3	87.5
Q_E	Expt.	3.09	3.10	3.23	3.65	4.12	4.56	5.06	5.36	5.49	5.61
	Theory		1.35	1.76	2.74	4.32	5.74	6.83	7.57	7.98	8.12
Q_H	Expt.	3.09	3.10	3.24	3.58	4.06	4.56	4.96	5.27	5.43	5.49
	Theory		1.30	1.77	2.80	4.24	5.62	6.64	7.38	7.77	7.89
$\frac{Q_E+Q_H}{2}$	Expt.	3.09	3.10	3.24	3.62	4.09	4.56	5.01	5.32	5.46	5.55
	Theory		1.32	1.77	2.77	4.28	5.68	6.73	7.47	7.87	8.01
$\frac{Q_E-Q_H}{Q_E+Q_H}$	Expt.	0.	0.	-0.003	0.009	0.007	0.0001	0.010	0.009	0.006	0.010
	Theory		0.017	-0.004	-0.010	0.009	0.010	0.014	0.013	0.014	0.014

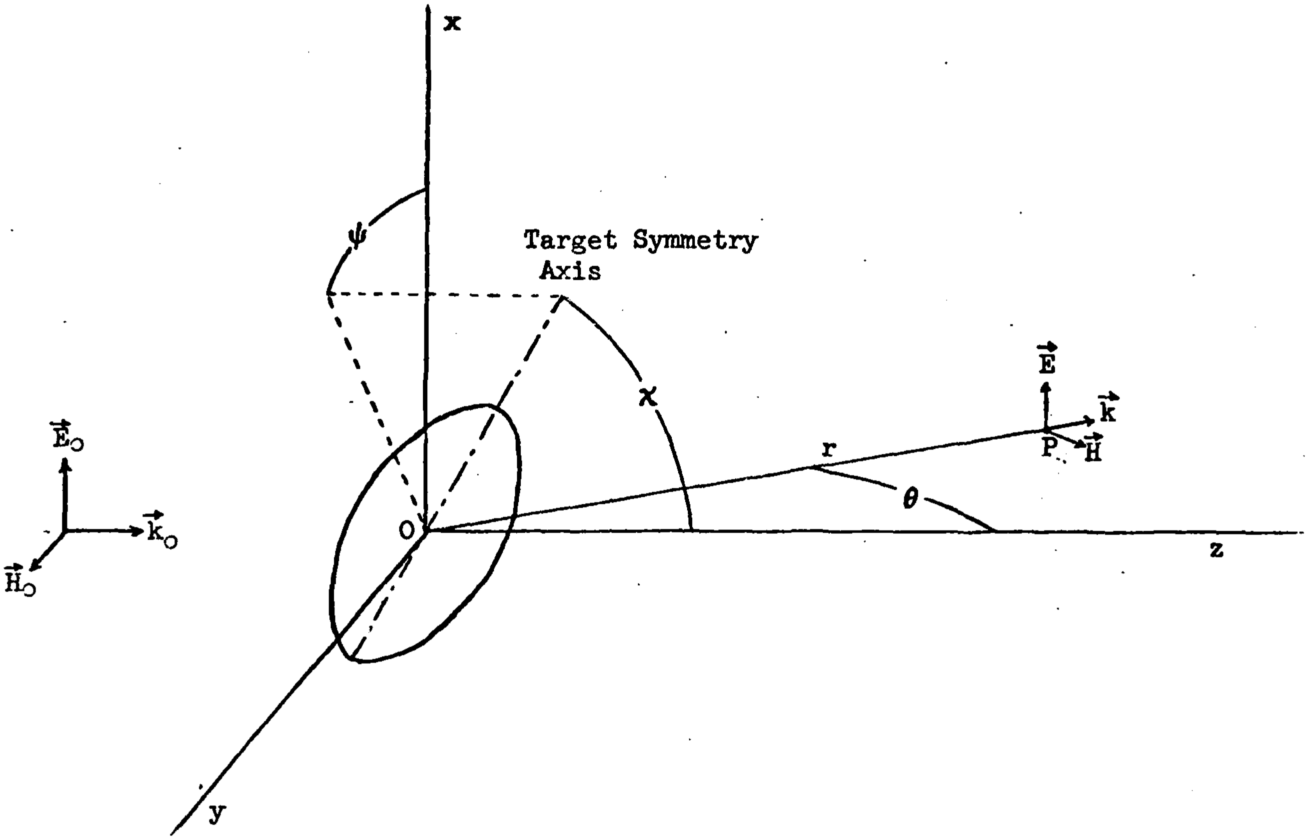

Fig. 1. Angular coordinates which specify the scattering angle θ and the target orientation angles (χ, ψ) with respect to the incident wave.

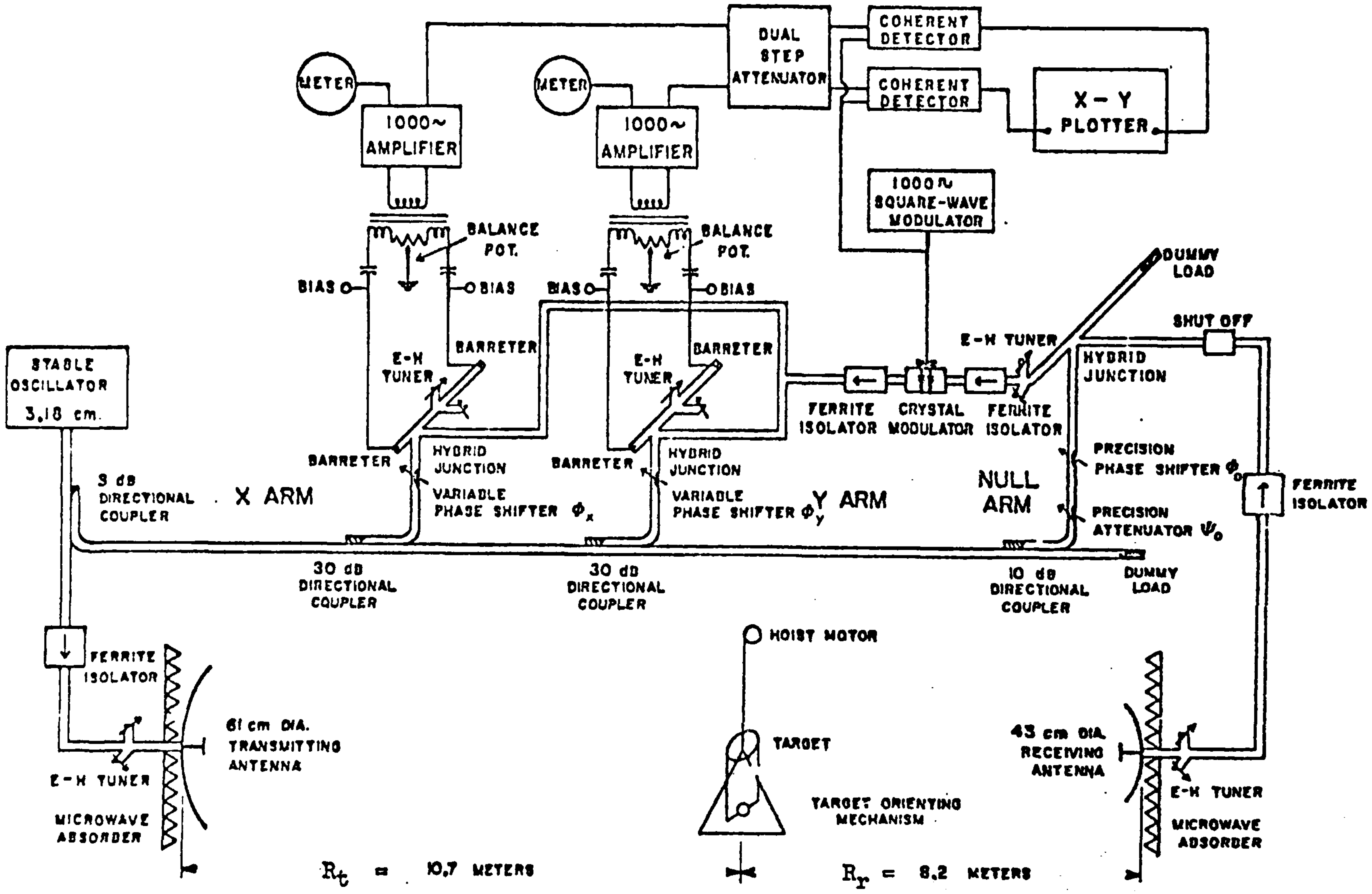

Fig. 2 Microwave circuitry, antenna diameters and ranges for forward-scatter($\theta = 0^{\circ}$) measurements. (University Building, Rensselaer Polytechnic Institute, Troy, N.Y.)

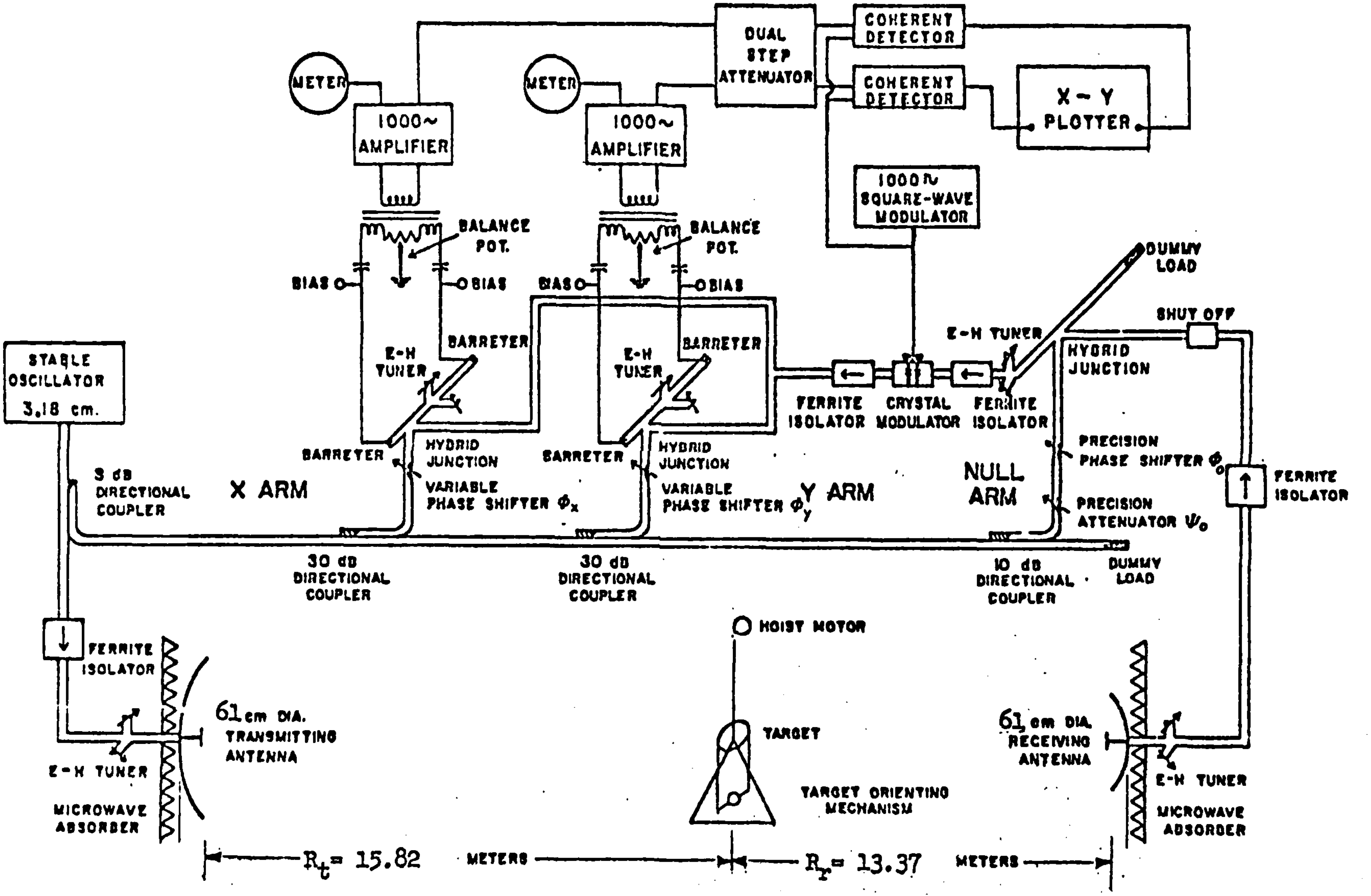

Fig. 3 Microwave circuitry, antenna diameters and ranges for forward-scatter($\theta \doteq 0°$) measurements. (Chapel, Peoples Ave. Complex, Rensselaer Polytechnic Institute, Troy, N.Y.)

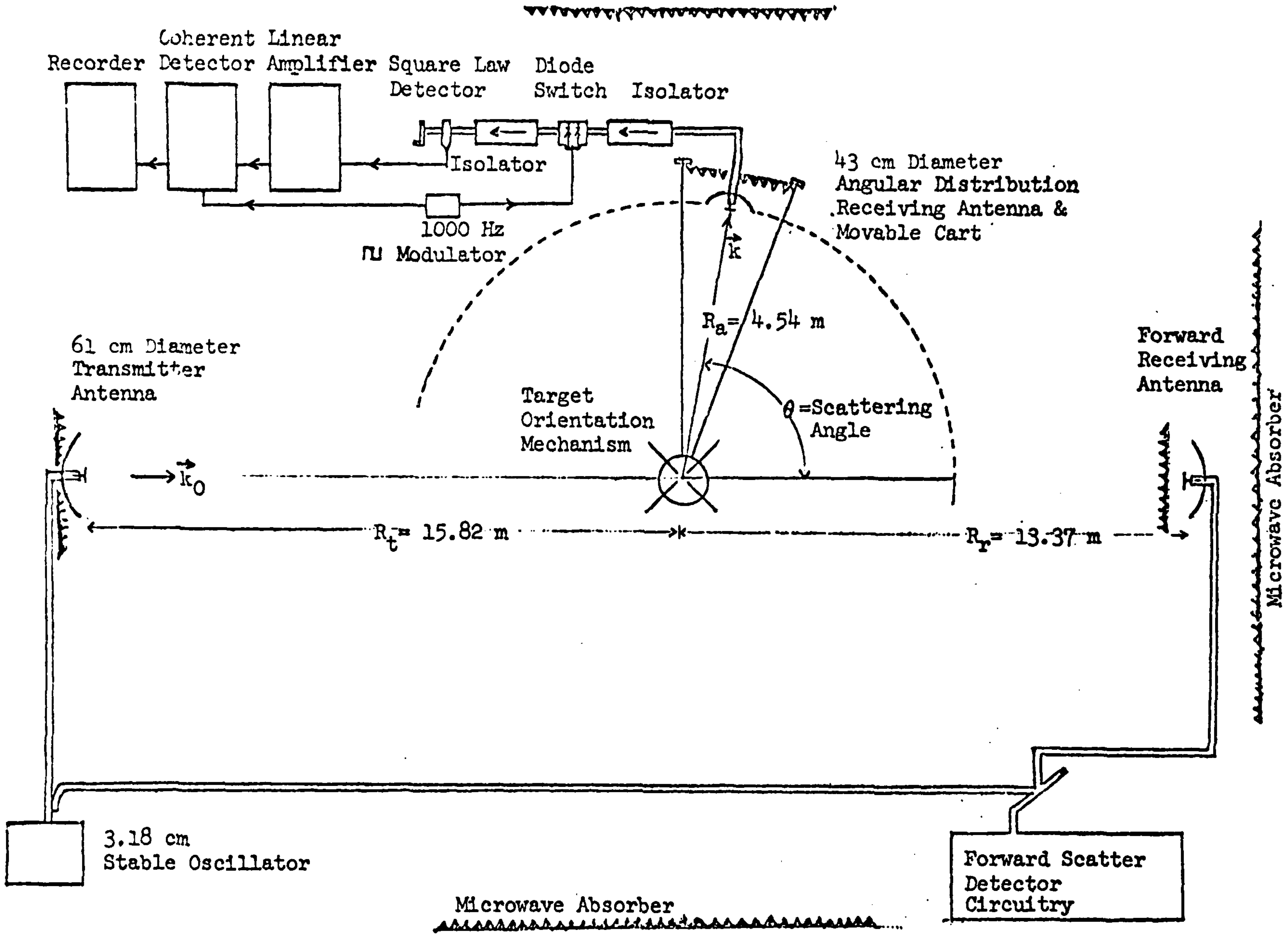

Fig. 4 Microwave circuitry, antenna diameters and ranges for angular distribution studies.

(Chapel, Peoples' Ave. Complex, Rensselaer Polytechnic Institute, Troy, N.Y.)

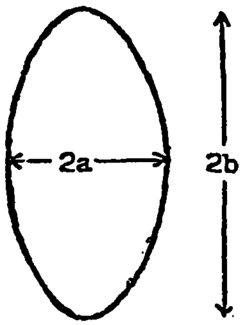

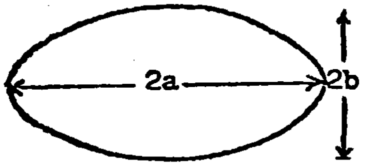

Fig. 5A Prolate Spheroid

Fig. 5B Oblate Spheroid

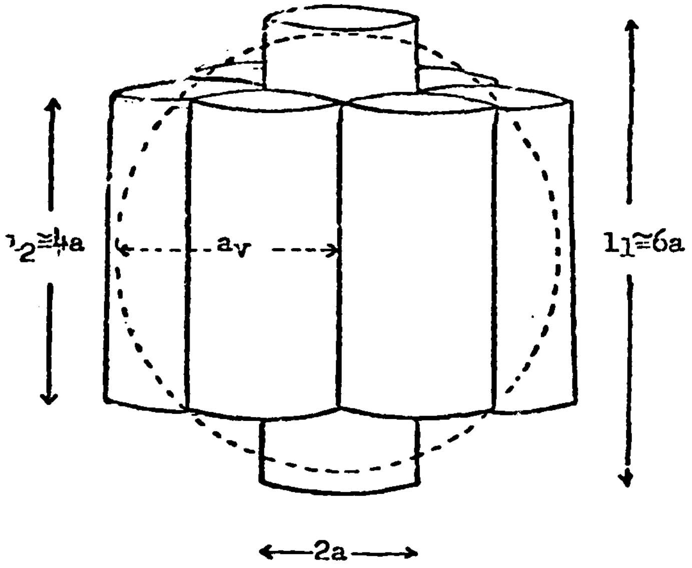

Fig. 5C Rough Particle

a_v is the radius of the equal-volume sphere.

Fig. 5 Target Shapes

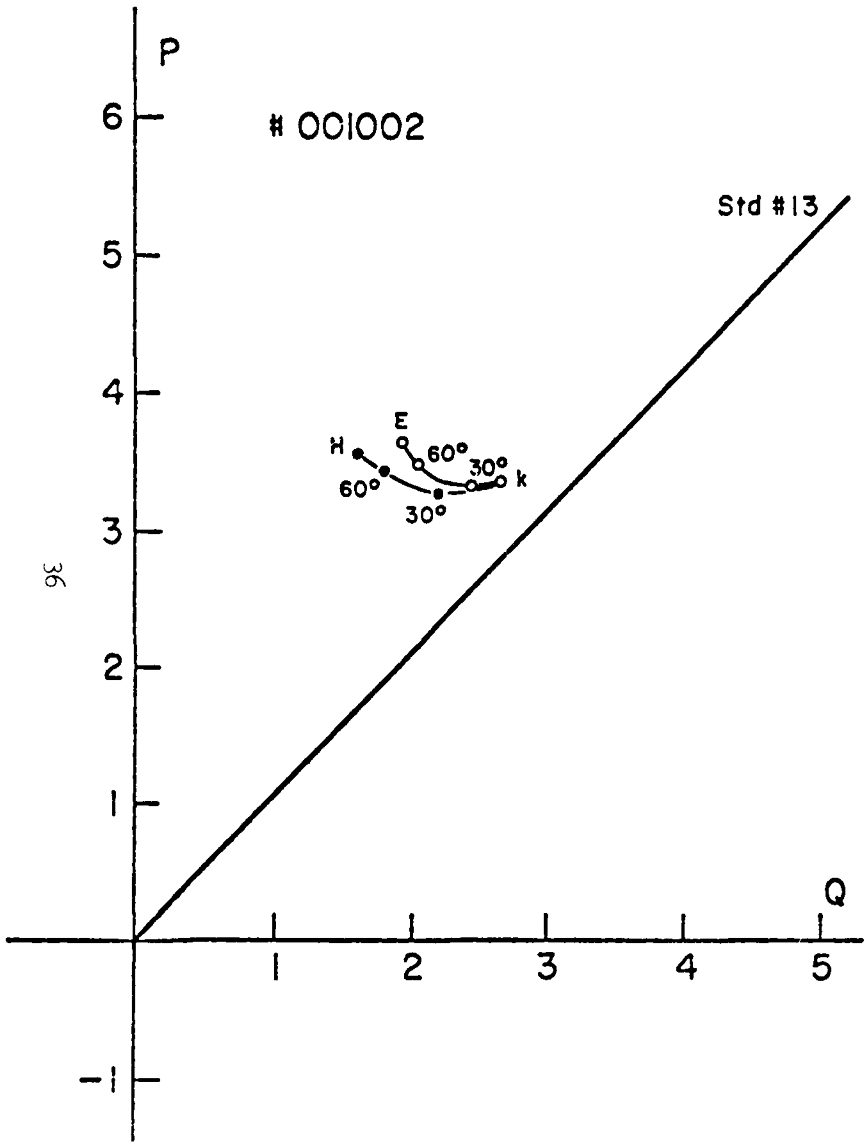

Fig. 6A An experimental forward-scattering P-Q plot for a spheroidal particle. (Size parameter x-2.688 and refractive index m=1.264)

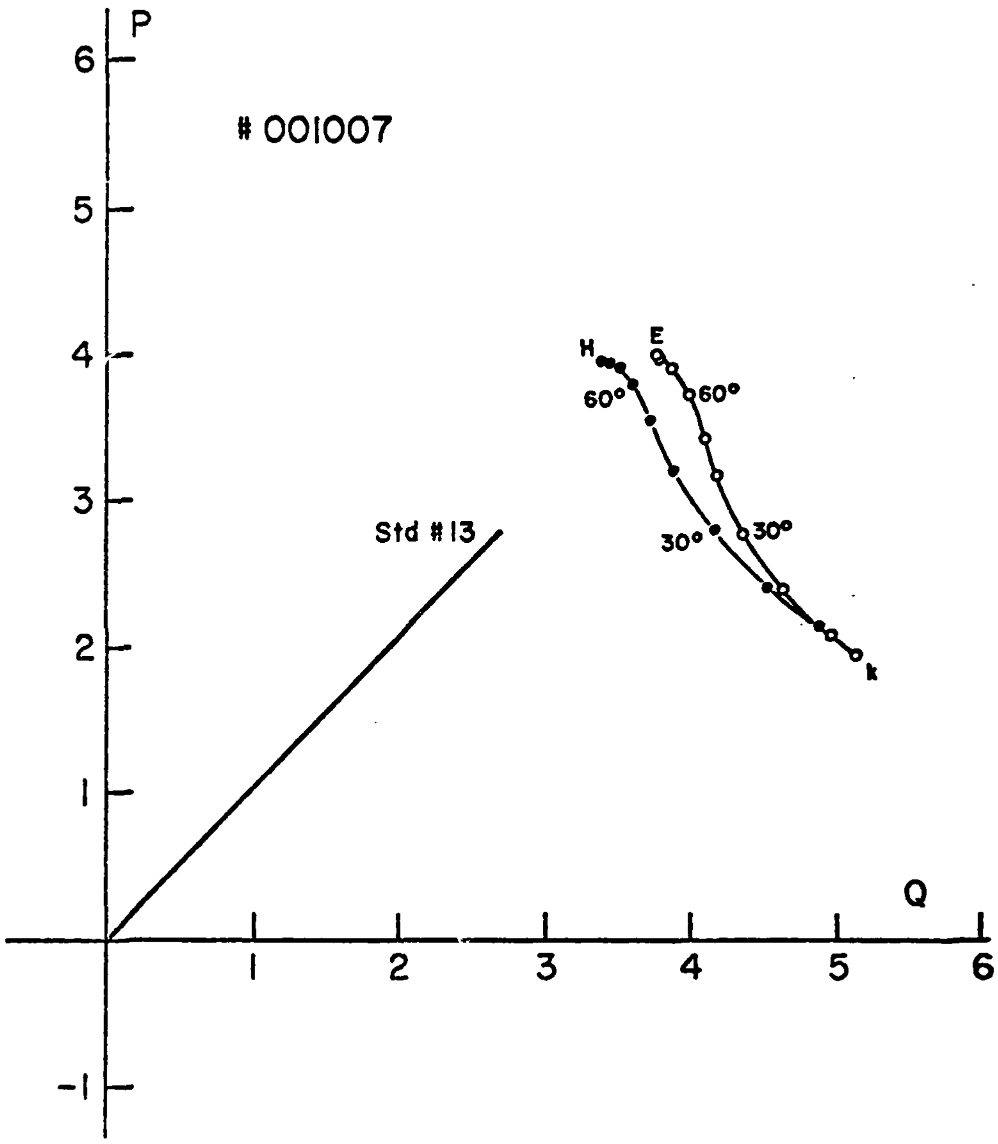

Fig. 6B An experimental forward-scattering P-Q plot for a spheroidal particle. (Size parameter x=3.726 and refractive index m=1.266.)

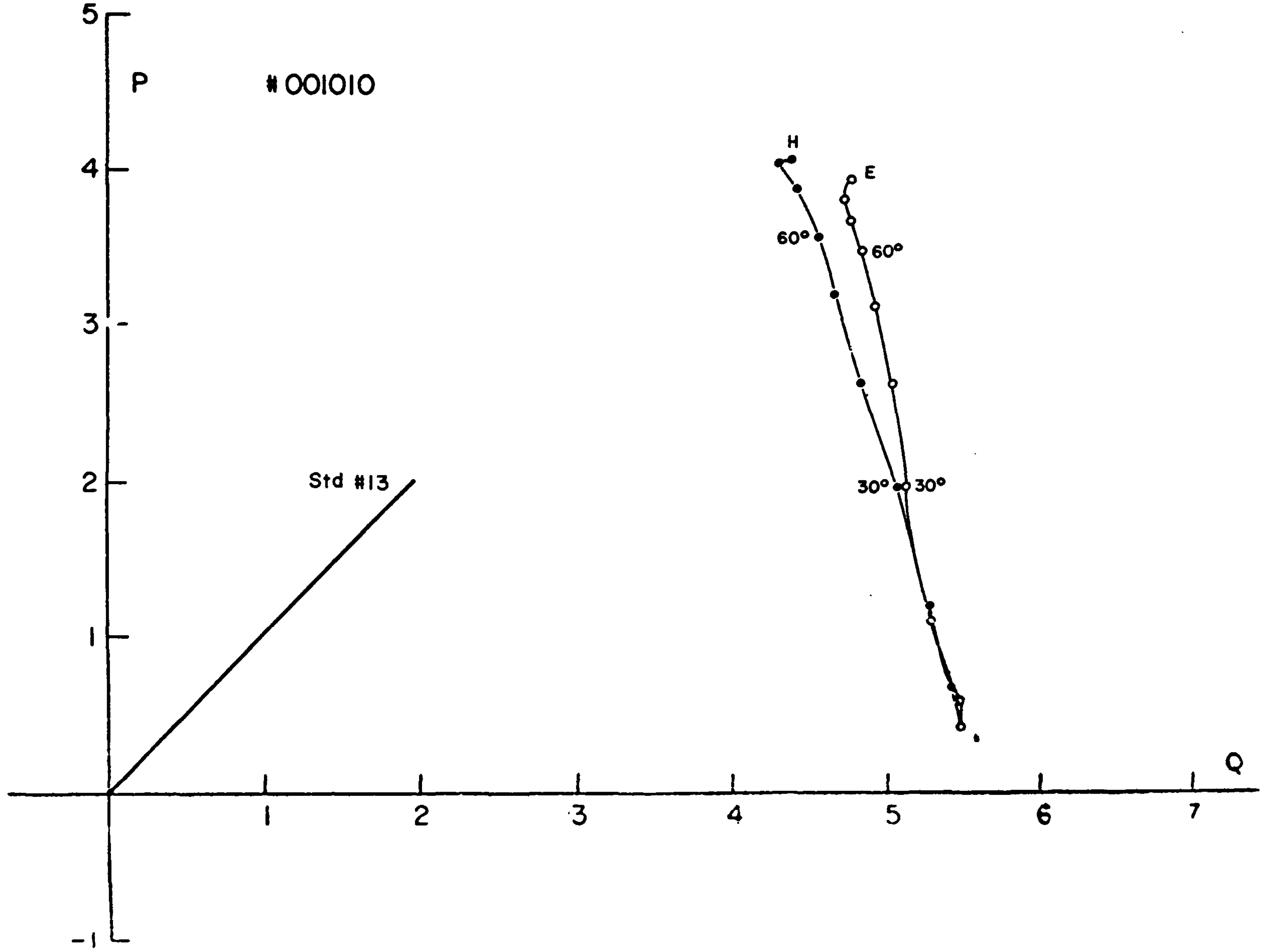

Fig. 6C An experimental forward-scattering P-Q plot for spheroidal particle. (Size parameter x=4.397 and refractive index m=1.270)

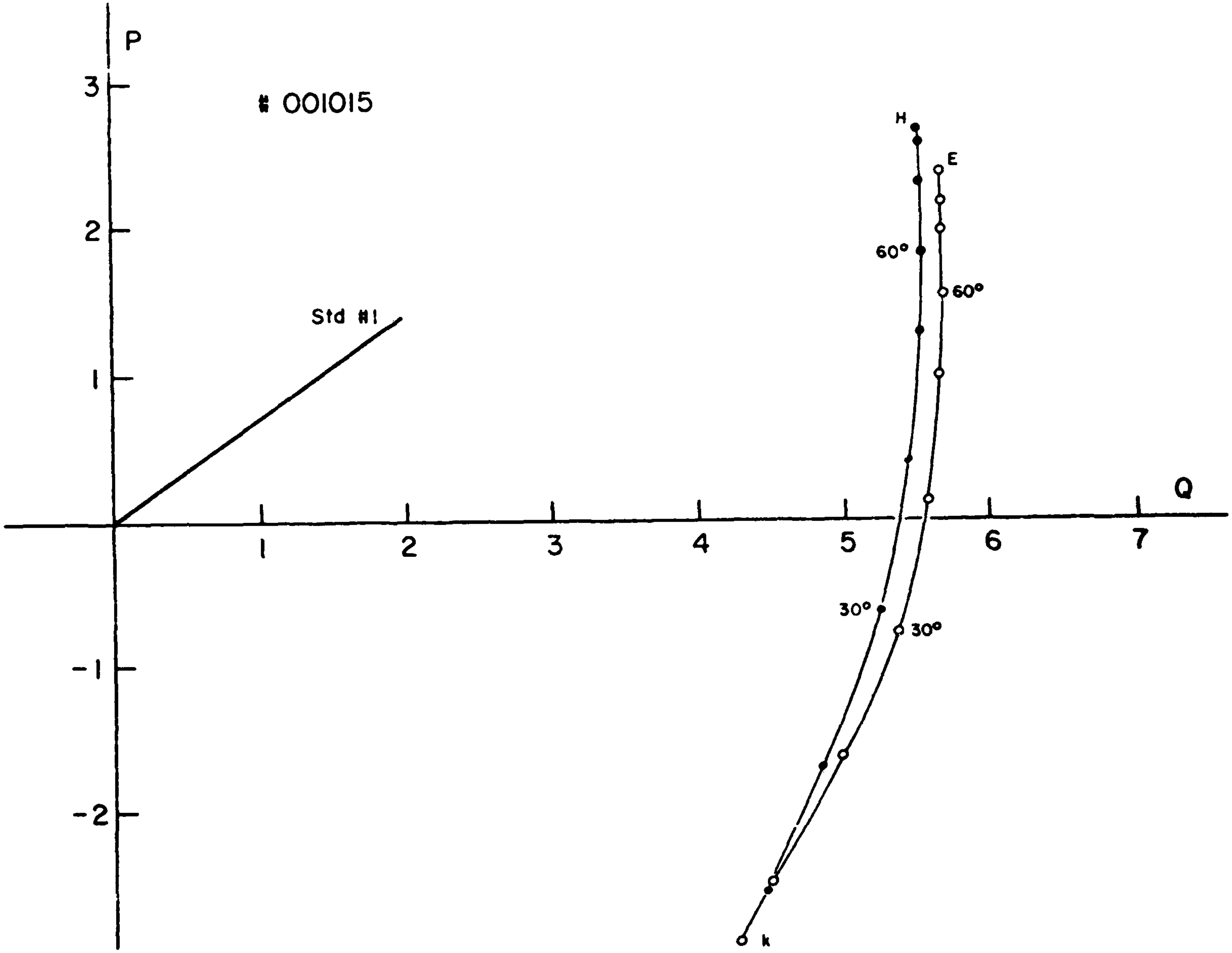

Fig. 6D An experimental forward-scattering P-Q plot for a spheroidal particle. (Size parameter x=5.960 and refractive index m=1.269)

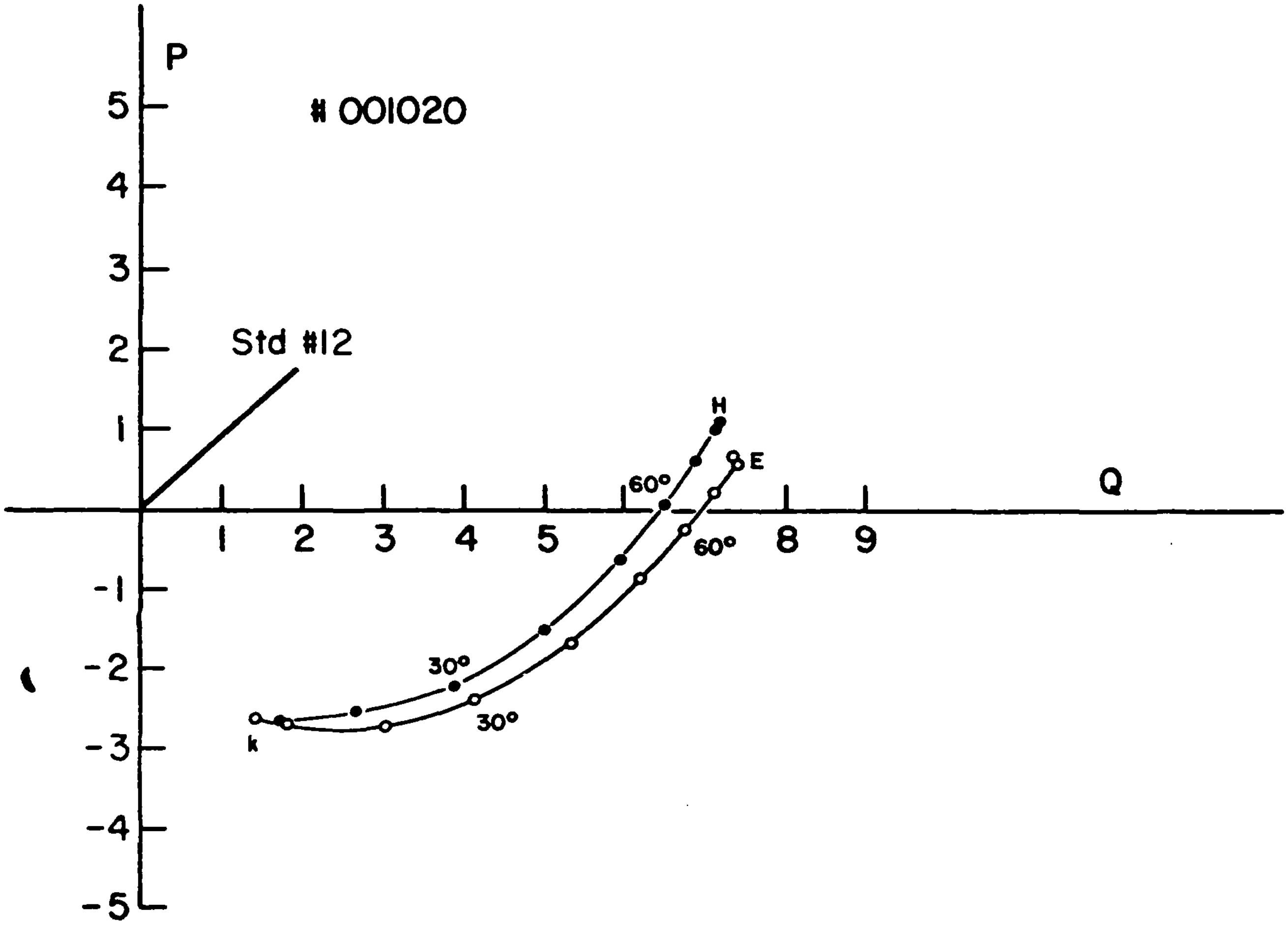

Fig. 6E An experimental forward-scattering P-Q plot for a spheroidal particle. (Size parameter x=8.076 and refractive index m-1.263)

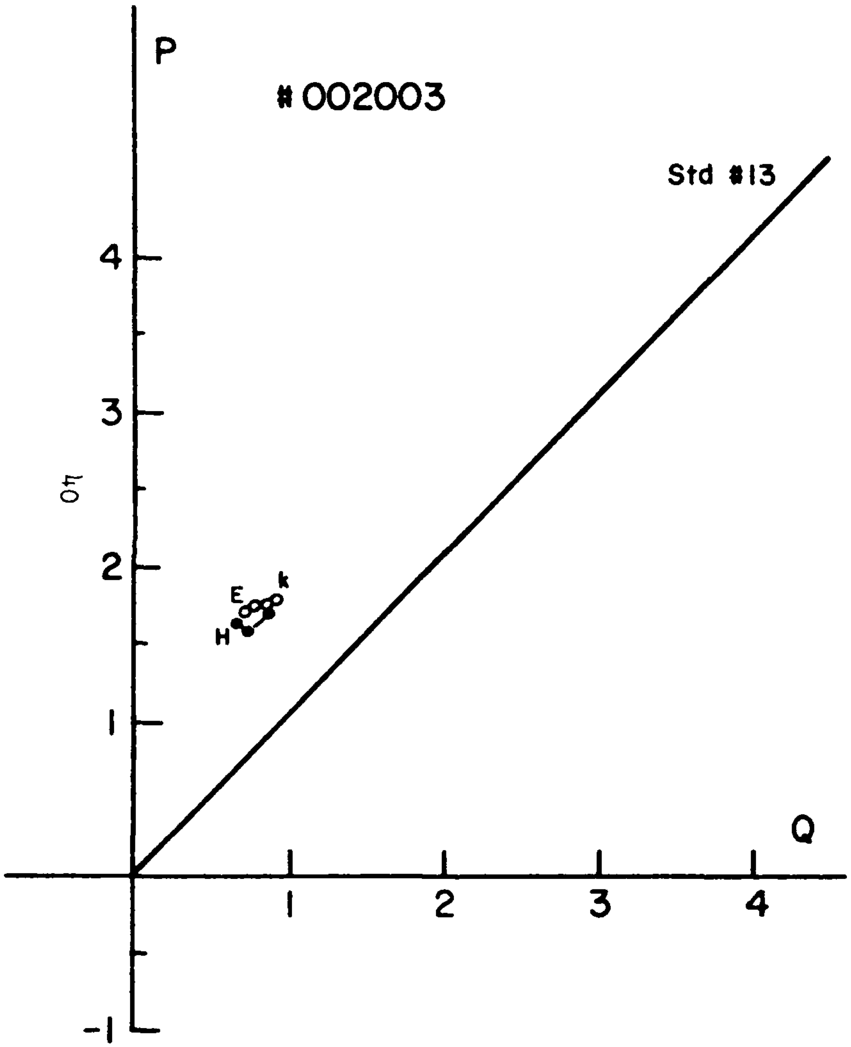

Fig. 7A An experimental forward-scattering P-Q for a spheroidal particle. (Size parameter x-2.921 and refractive index m=1.109)

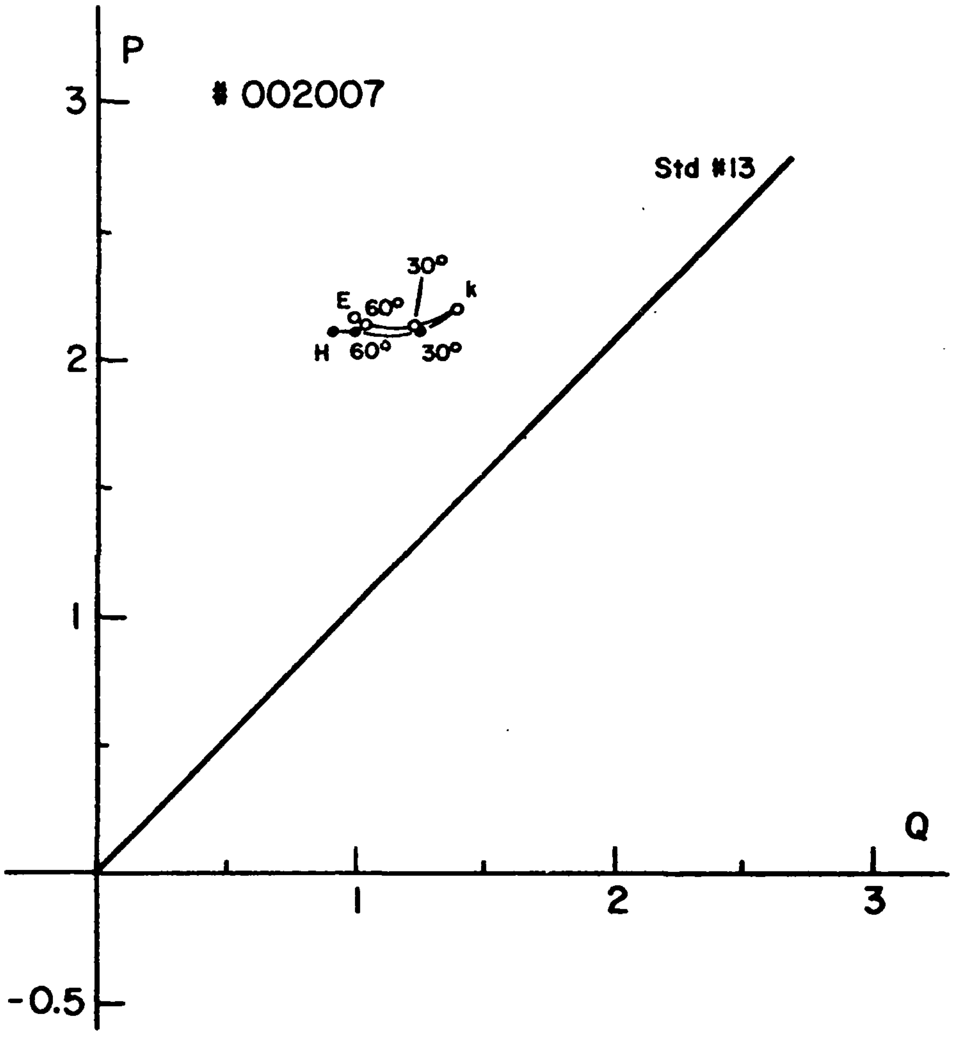

Fig. 7B An experimental forward-scattering P-Q for a spheroidal particle. (Size parameter x-3.747 and refractive index m-1.109)

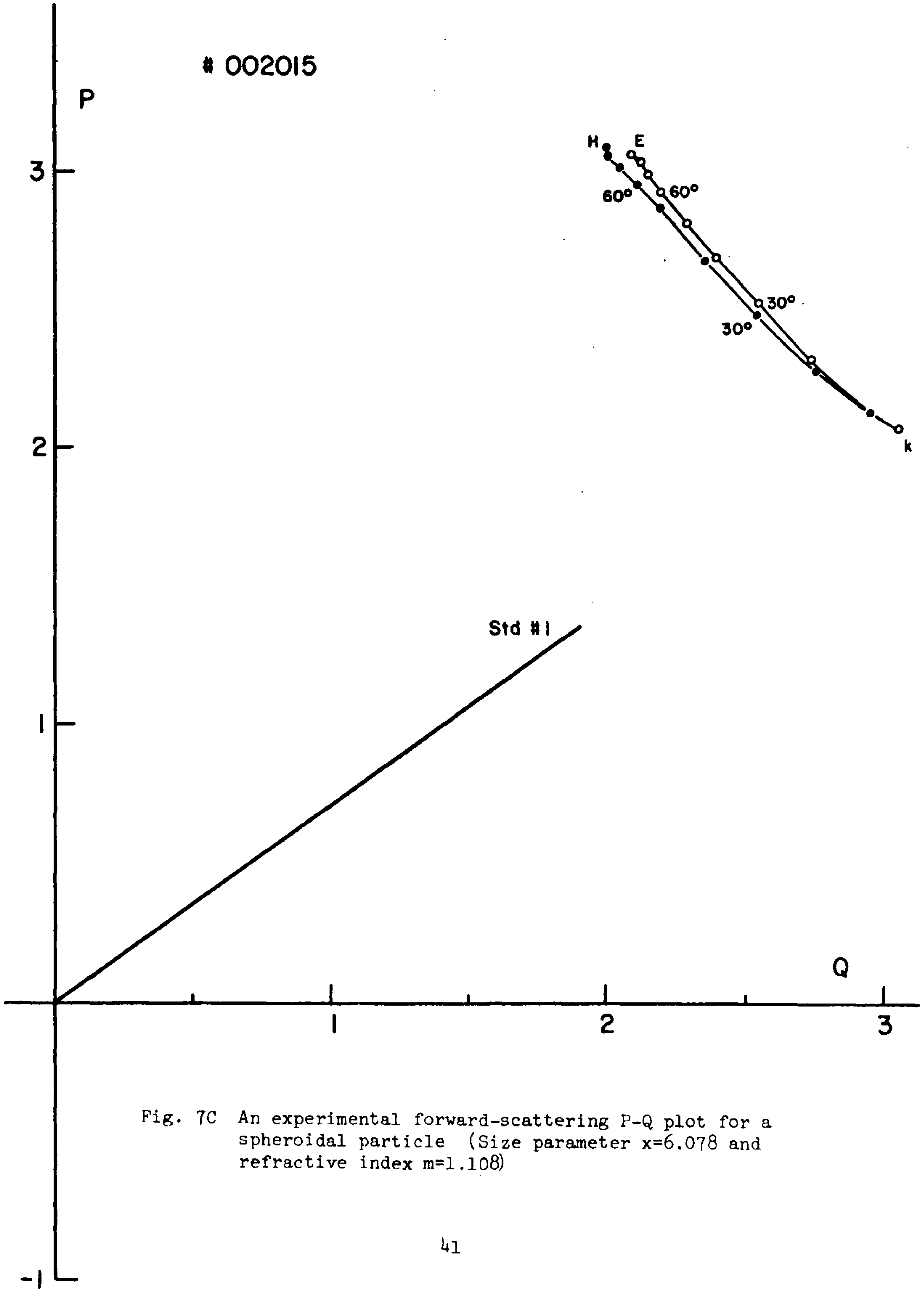

Fig. 7C An experimental forward-scattering P-Q plot for a spheroidal particle (Size parameter x=6.078 and refractive index m=1.108)

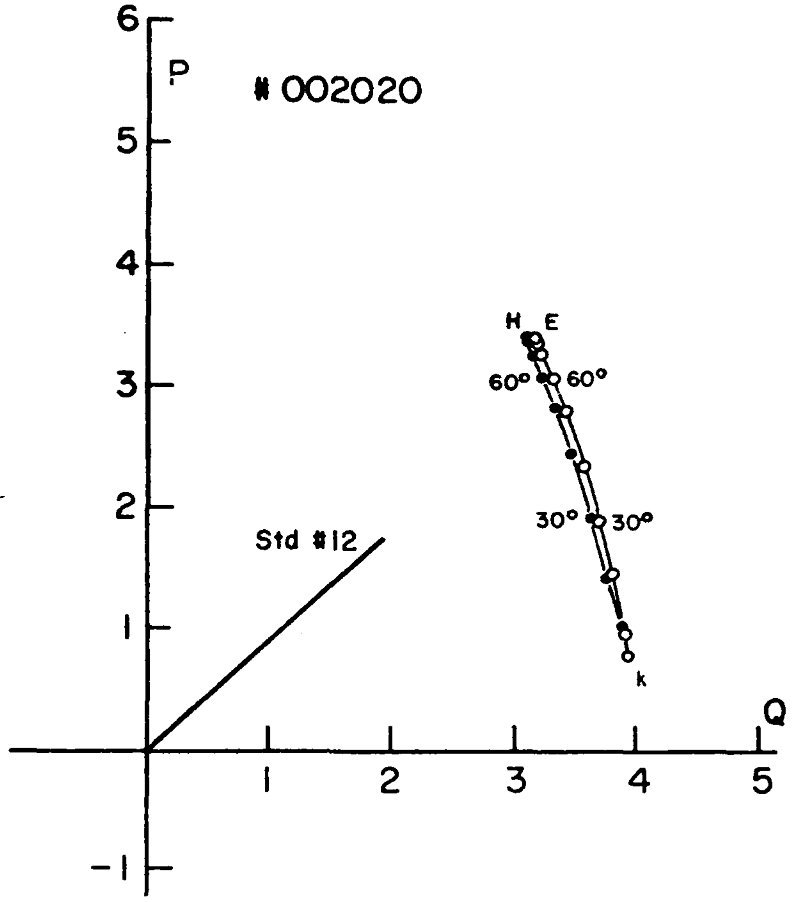

Fig. 7D An experimental forward-scattering P-Q plot for a spheroidal particle. (Size parameter x=8.076 and refractive index m=1.110)

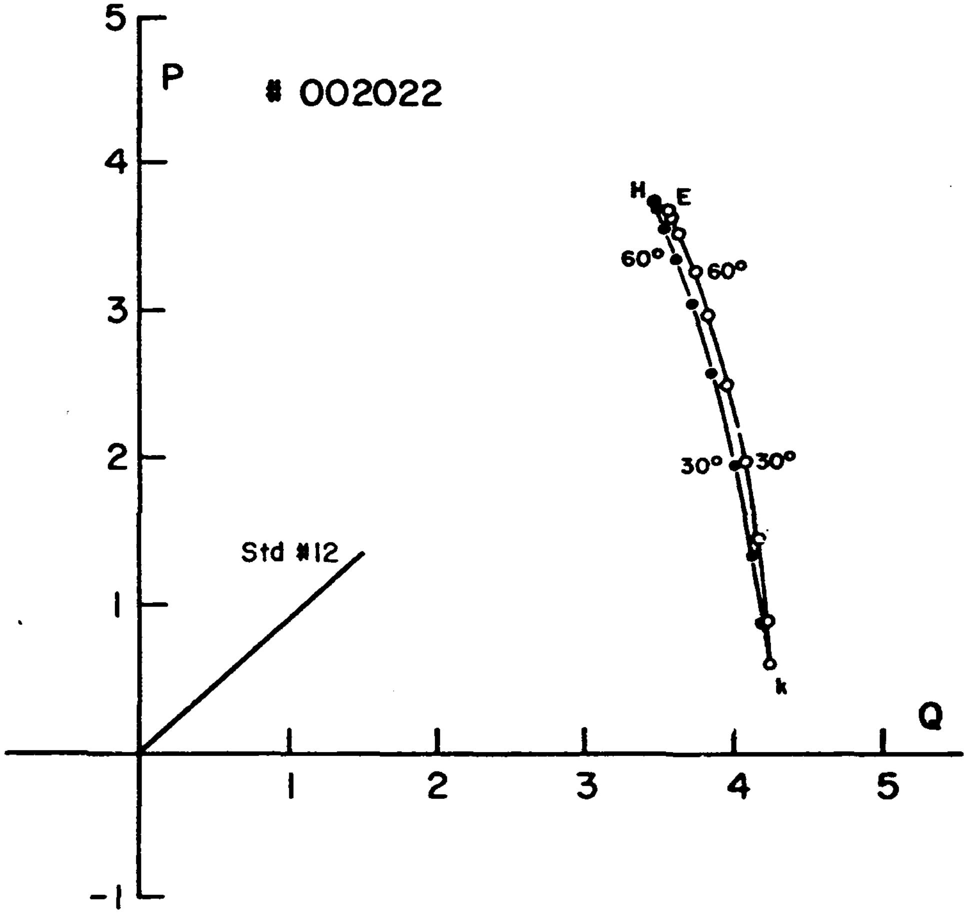

Fig. 7E An experimental forward-scattering P-Q plot for a spheroidal particle (Size parameter x=8.881 and refractive index m=1.111)

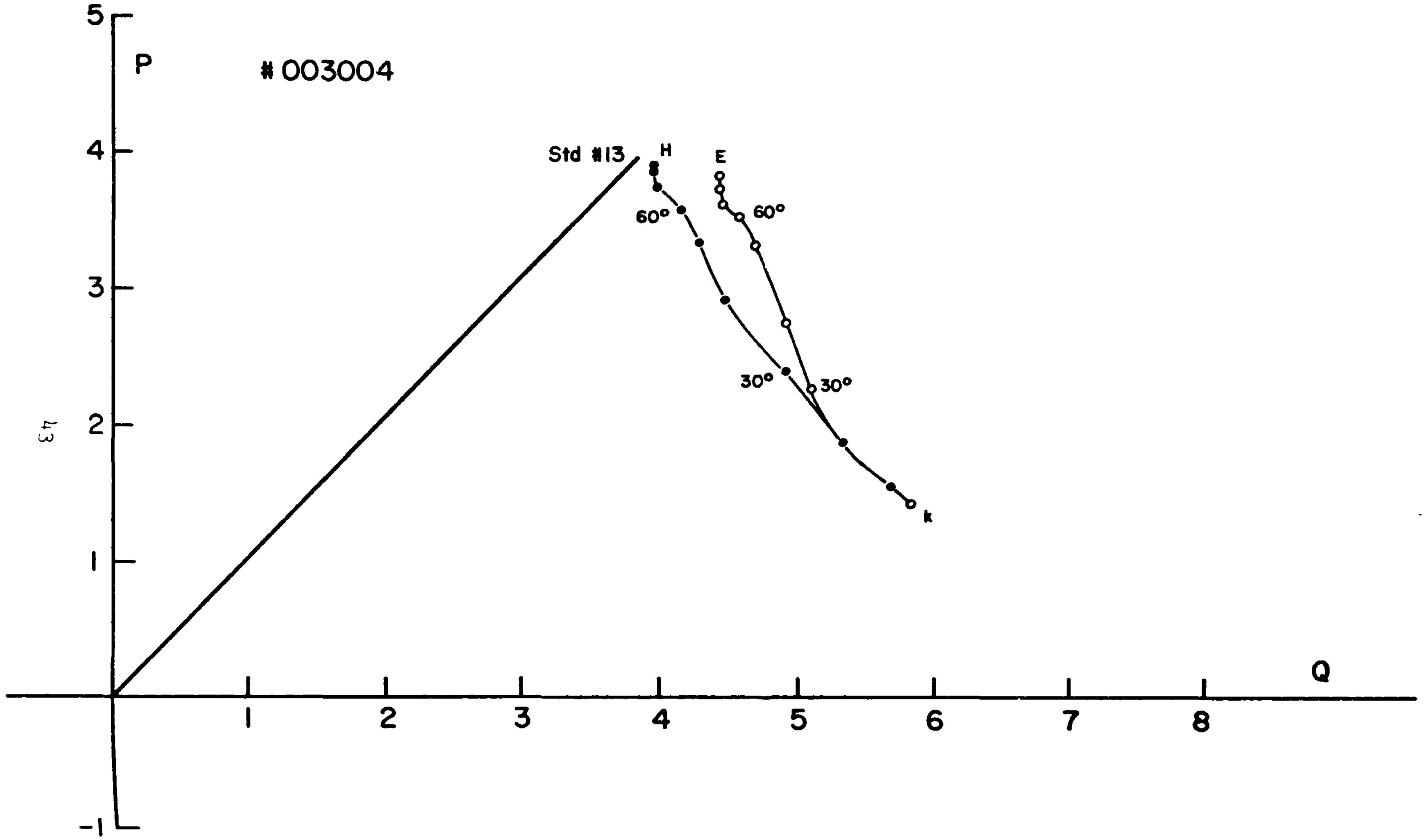

Fig. 8A An experimental forward-scattering P-Q plot for a spheroidal particle. (Size parameter x=3.134 and refractive index m=1.361)

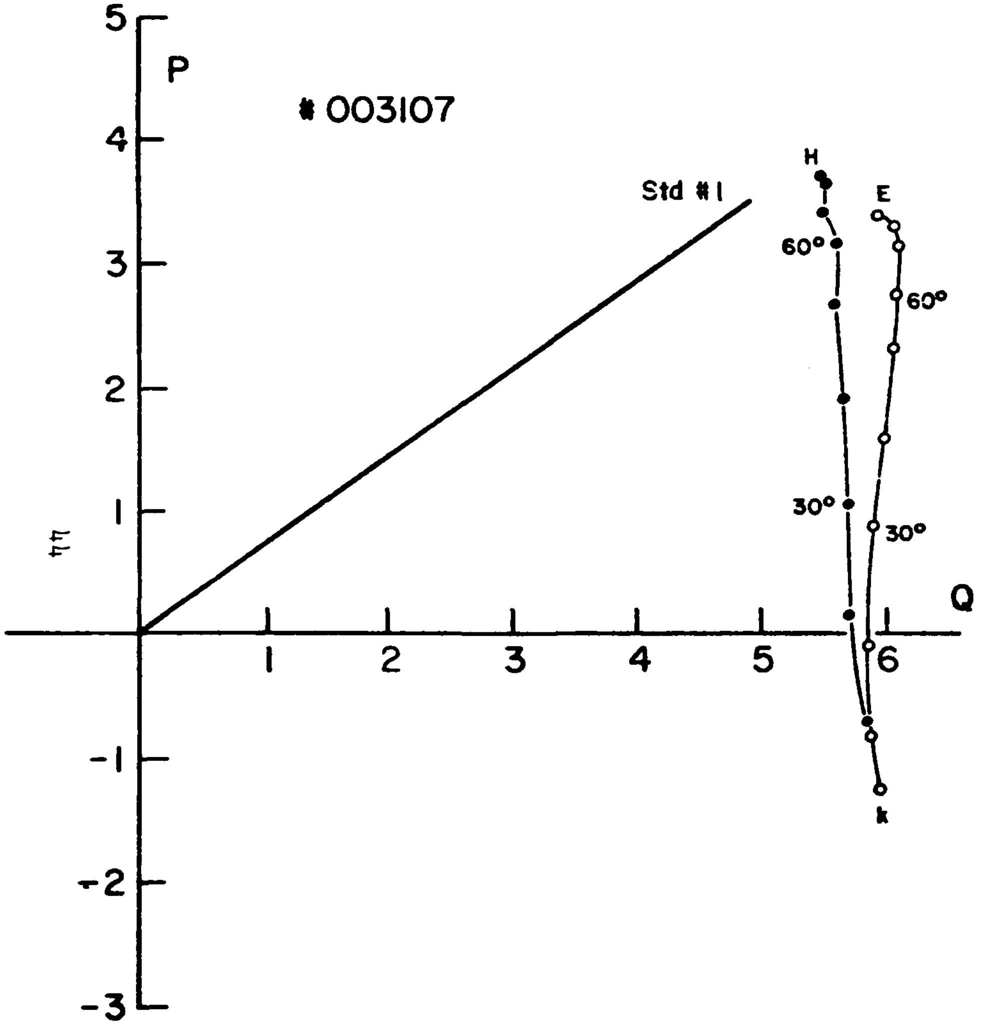

Fig. 8B An experimental forward-scattering P-Q plot for a spheroidal particle. (Size parameter x=3.778 and refractive index m=1.371)

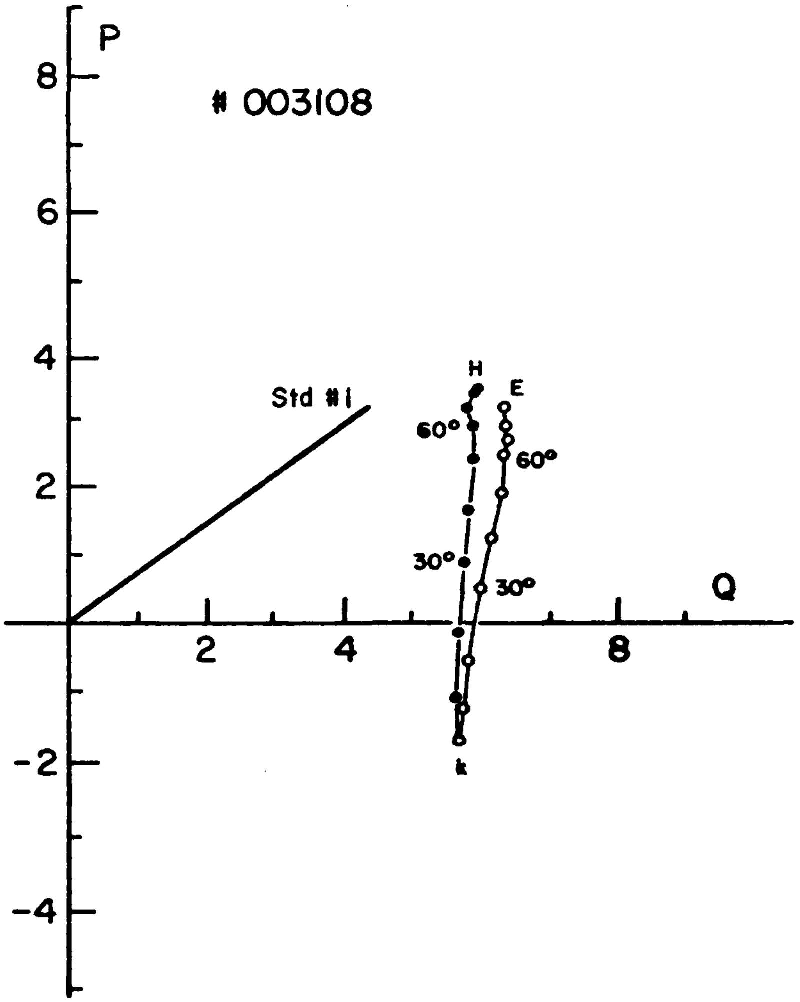

Fig. 8C An experimental forward-scattering P-Q plot for a spheroidal particle. (Size parameter x=3.961 and refractive index m=1.374)

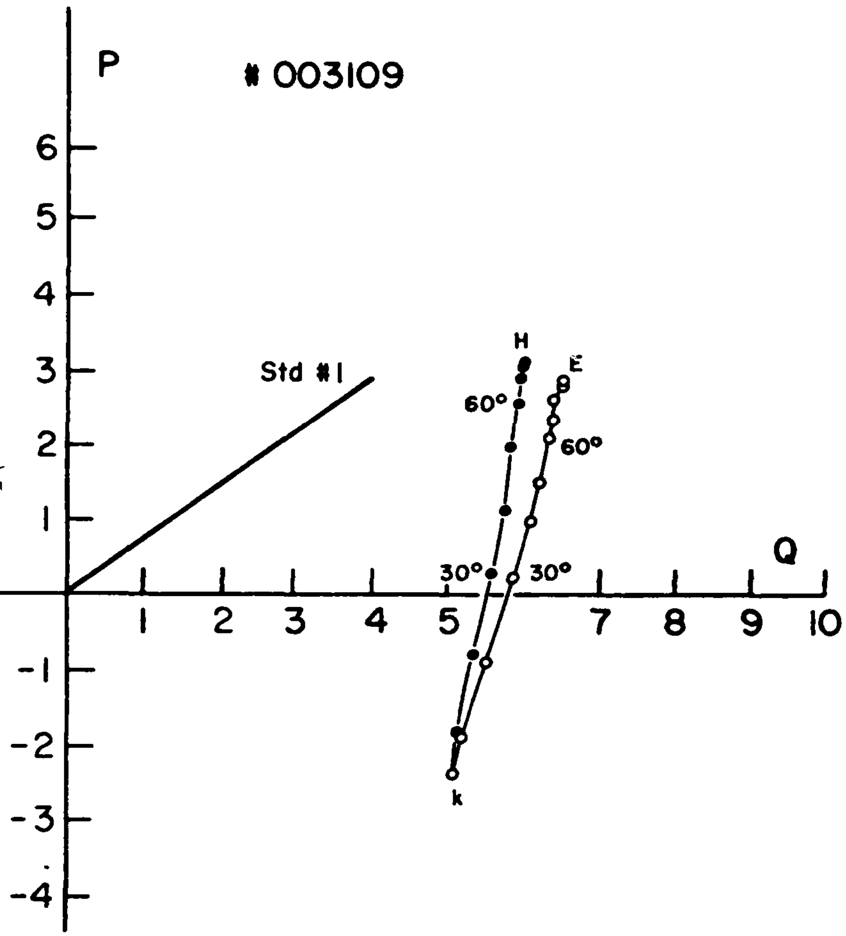

Fig. 8D An experimental forward-scattering P-Q plot for a spheroidal particle (Size parameter x-4.166 and refractive index m=1.372)

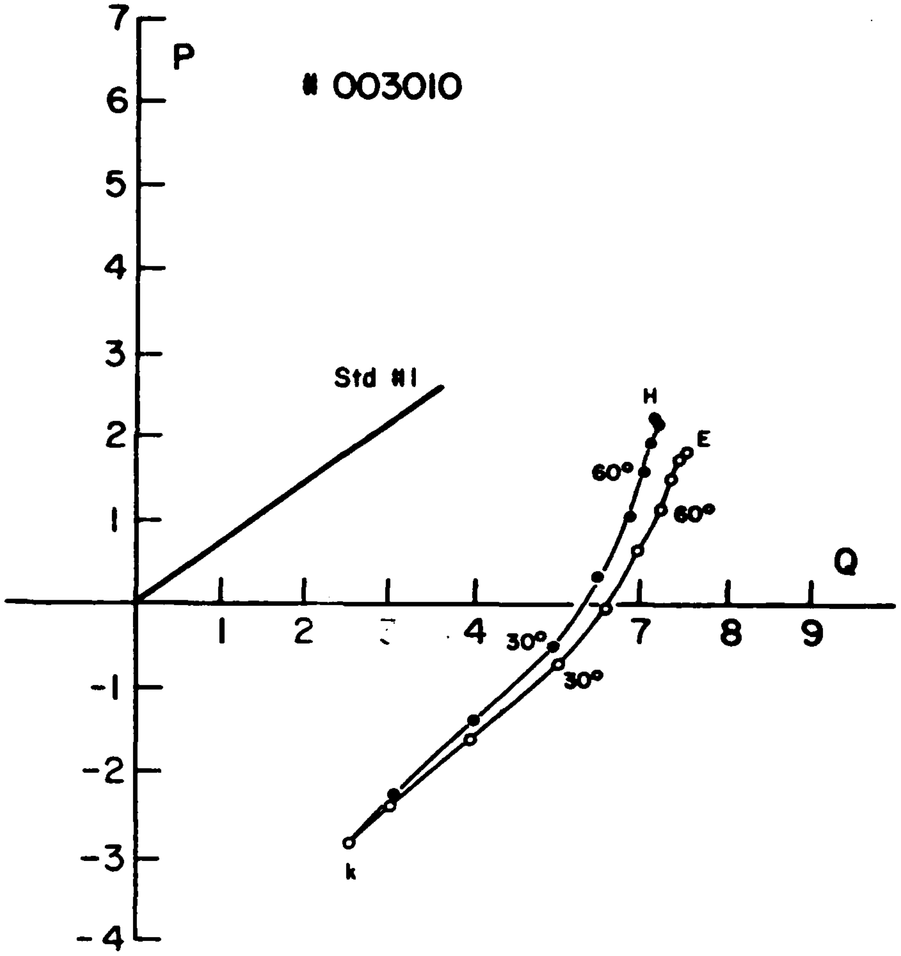

Fig. 8E An experimental forward-scattering P-Q plot for a spheroidal particle (Size parameter x=4.401 and refractive index m=1.370)

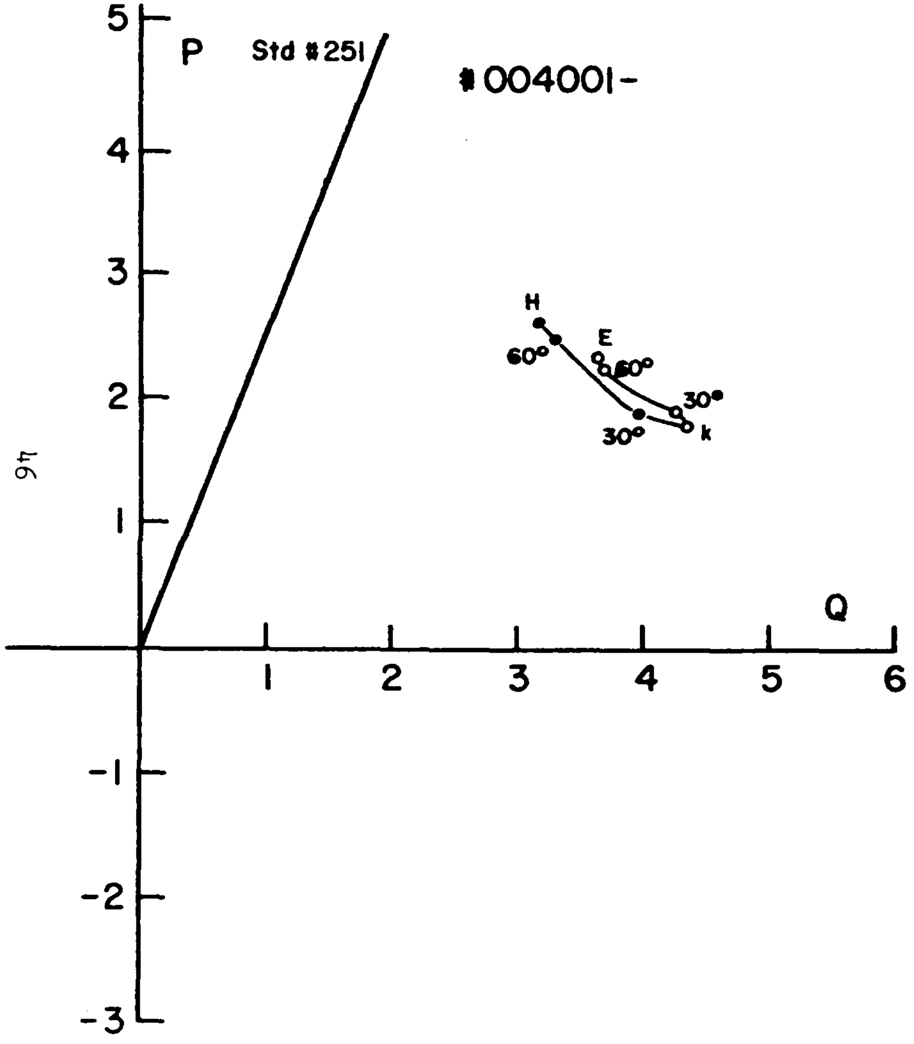

Fig. 9A An experimental forward-scattering P-Q plot for a spheroidal particle. (Size parameter x=2.291 and refractive index m=1.33-i0.05)

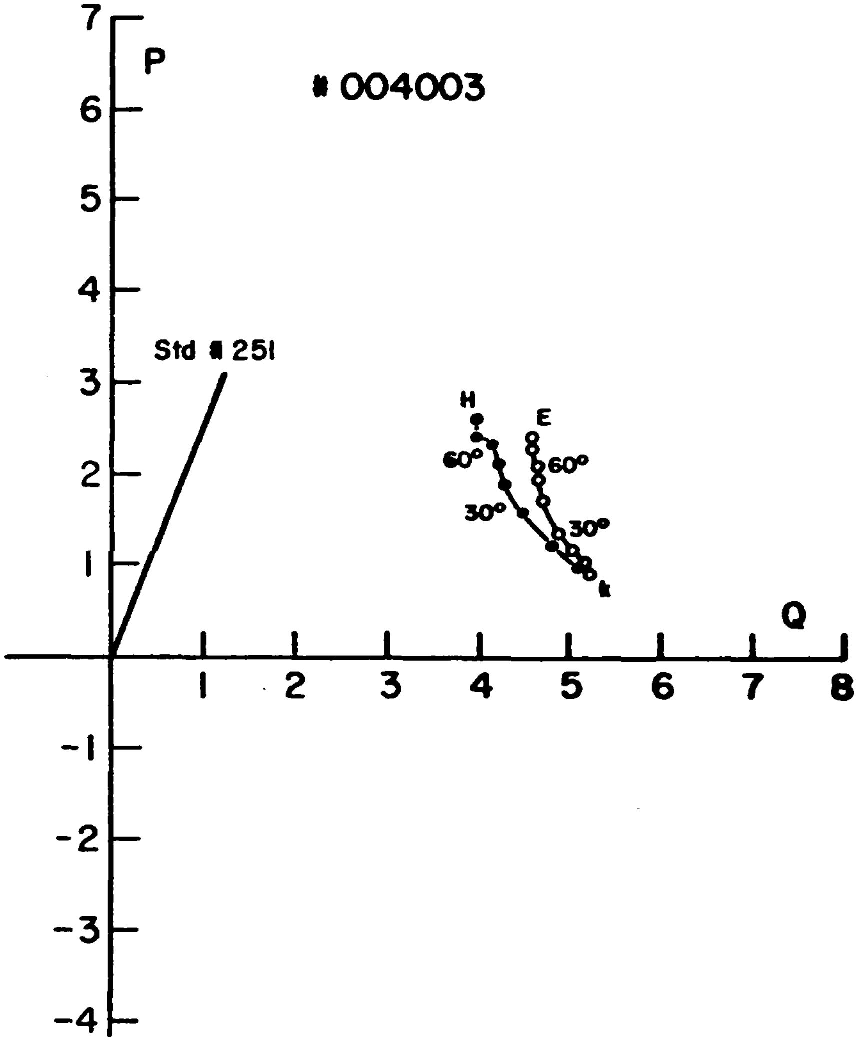

Fig. 9B An experimental forward-scattering P-Q plot for a spheroidal particle. (Size parameter x=2.907 and refractive index m=1.33-i0.05)

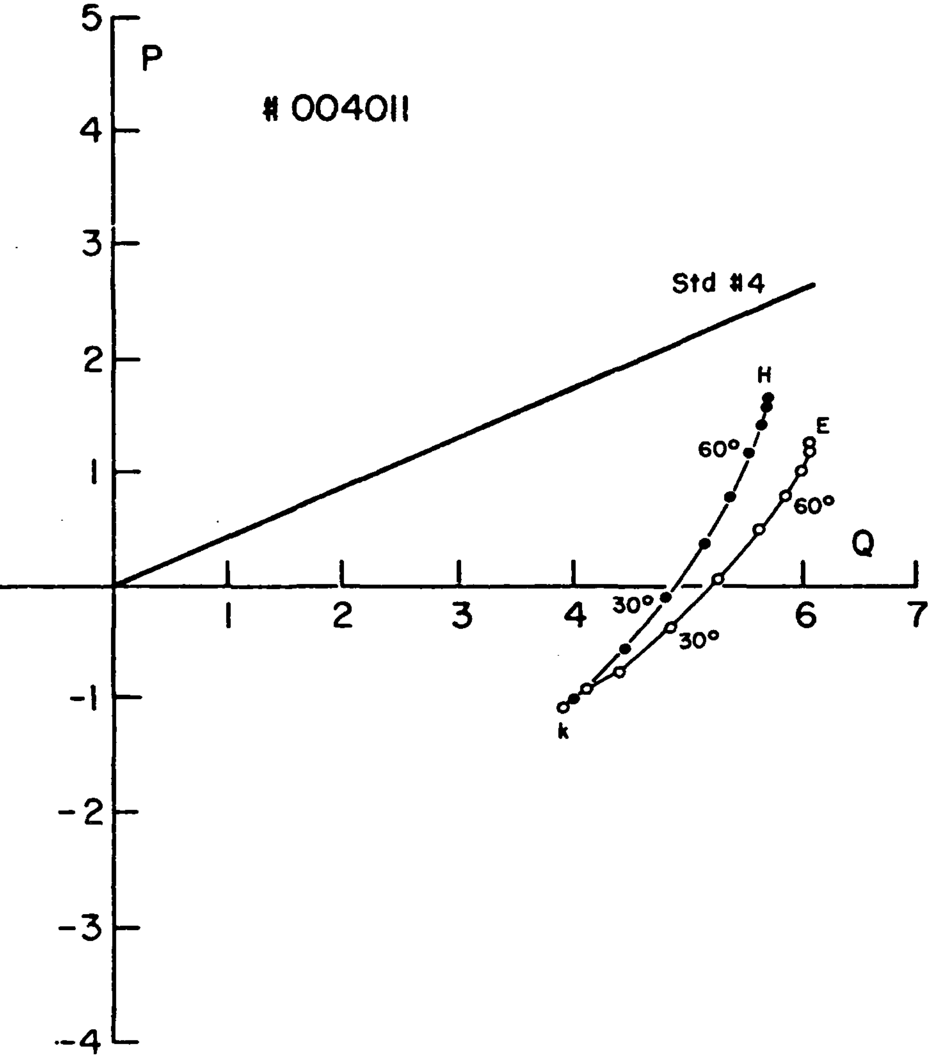

Fig. 9C An experimental forward-scattering P-Q plot for a spheroidal particle. (Size parameter x=4.642 and refractive index m=1.33-io.05)

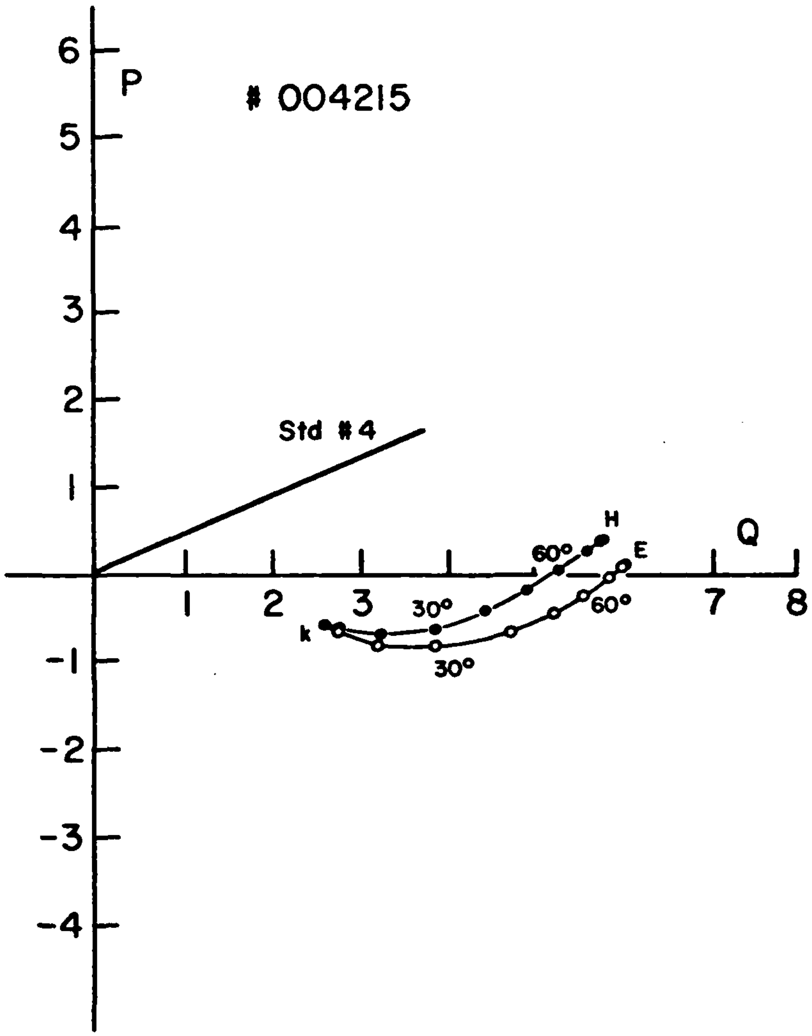

Fig. 9D An experimental forward-scattering P-Q for a spheroidal particle. (Size parameter x=5.972 and refractive index m=1.33-io.05)

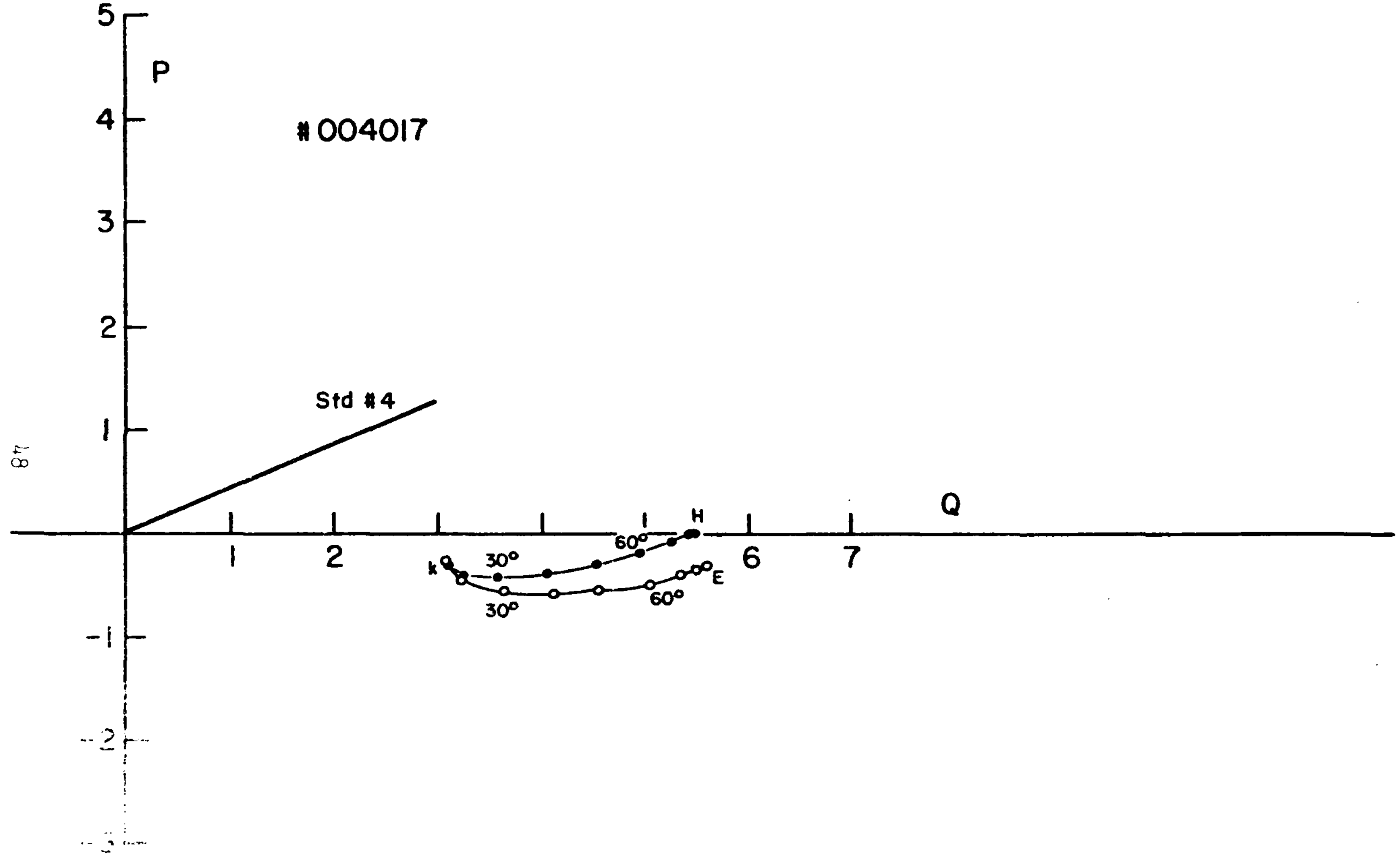

Fig. [illegible] An experimental forward-scattering P-Q plot for a spheroidal particle. (Size parameter $x=6.689$ and refractive index $m=1.33-i0.05$)

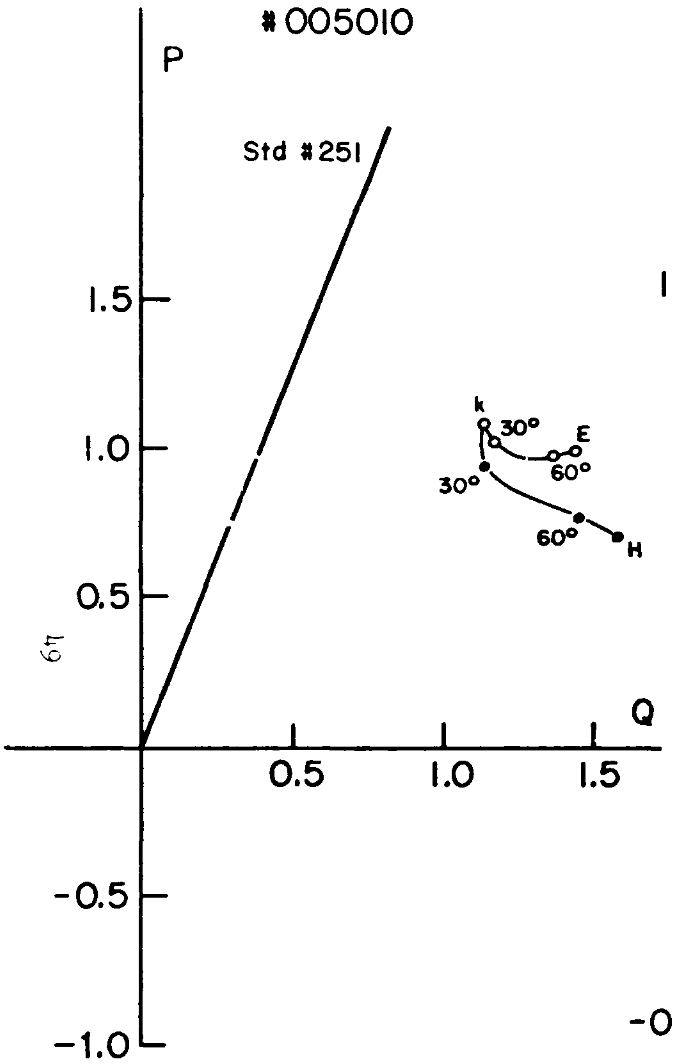

Fig. 10A An experimental forward-scattering P-Q plot for a spheroidal particle. (Size parameter x=3.558 and refractive index m=1.33-i0.05)

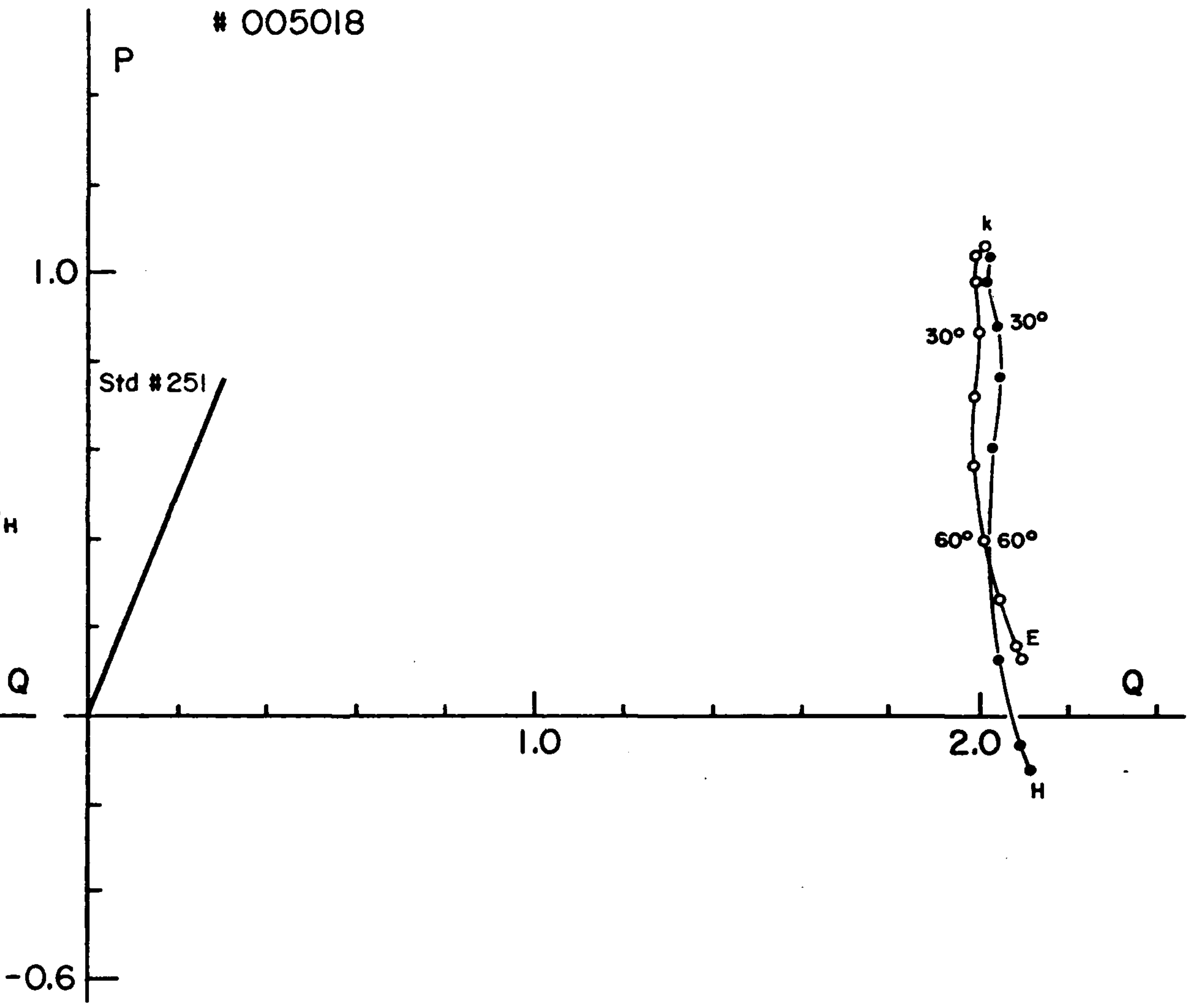

Fig. 10B An experimental forward-scattering P-Q plot for a spheroidal particle. (Size parameter x=5.888 and refractive index m=1.33-i0.05)

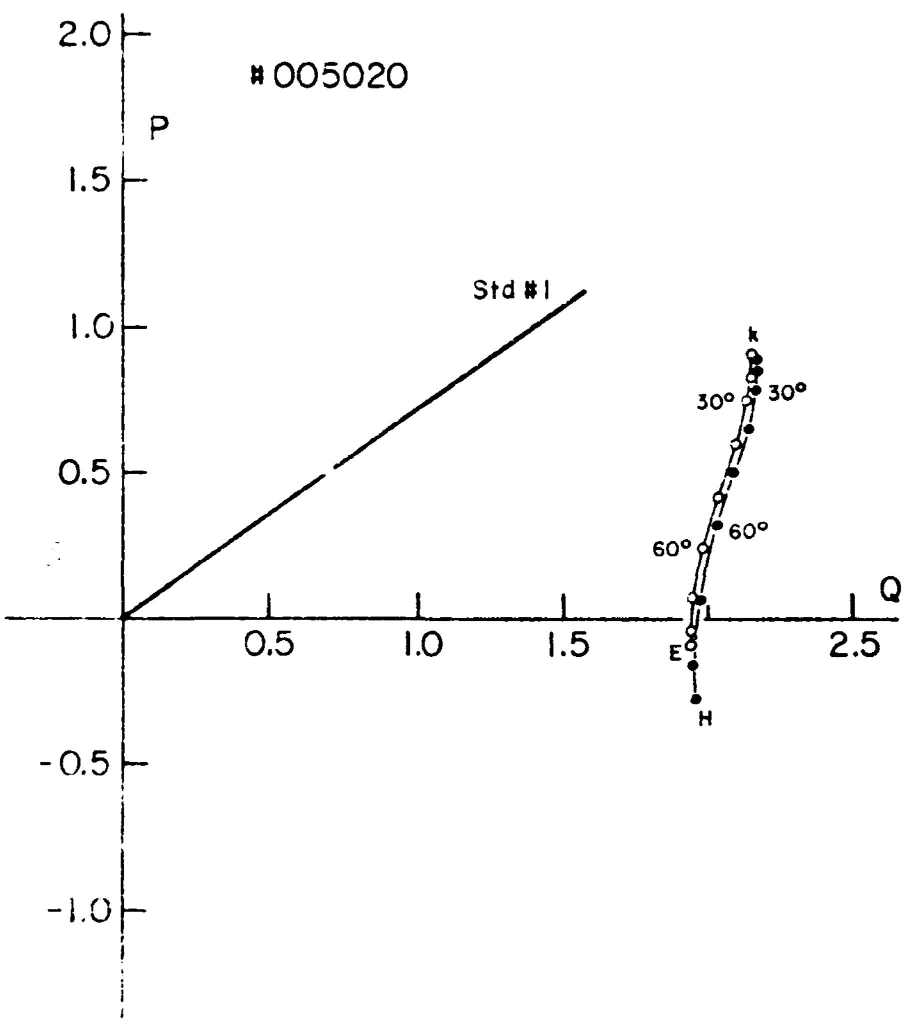

[illegible] forward-scattering P-Q plot for a
[illegible] (Size parameter x=[illegible] and
[illegible])

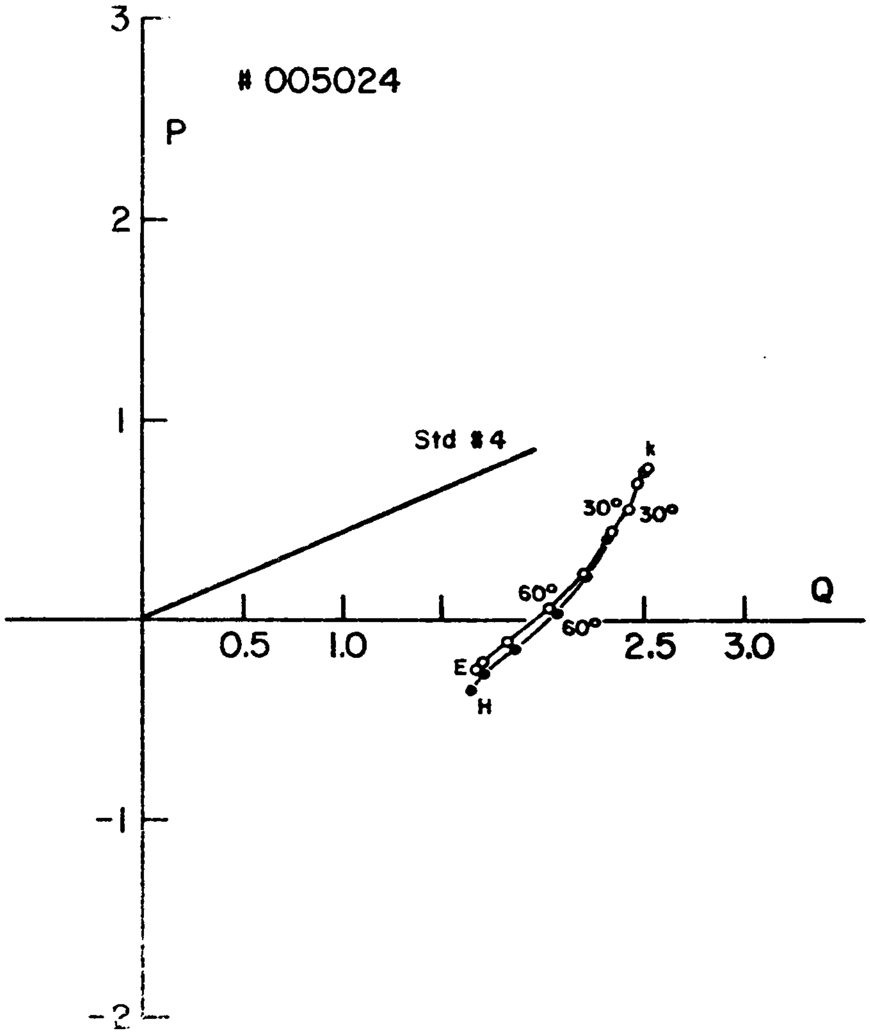

Fig. 10D An experimental forward-scattering P-Q plot for a spheroidal particle (Size parameter x=8.241 and refractive index m=1.33-i0.05)

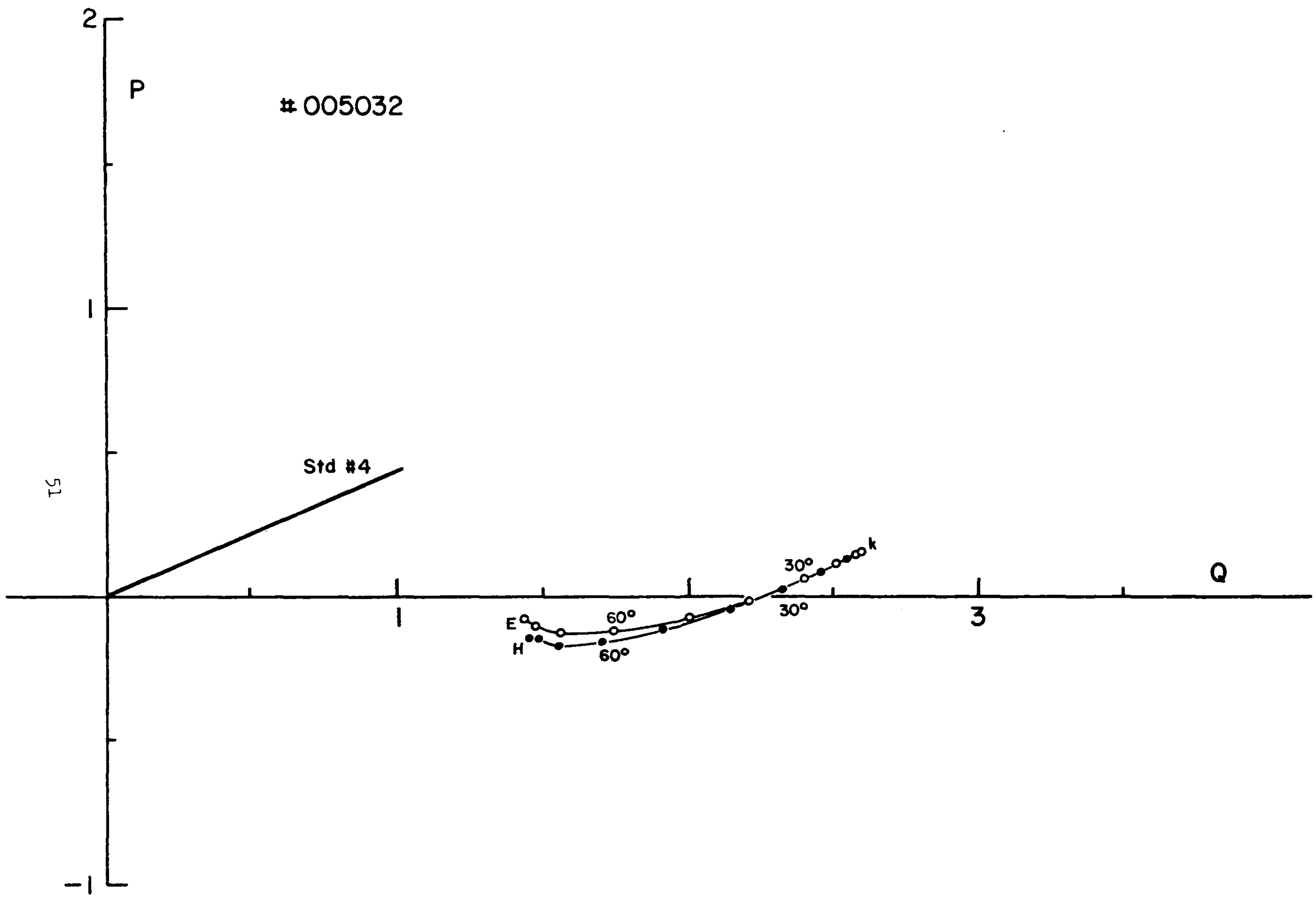

Fig. 10E An experimental forward-scattering P-Q plot for a spheroidal particle. (Size parameter x=11.408 and refractive index m=1.33-i0.05)

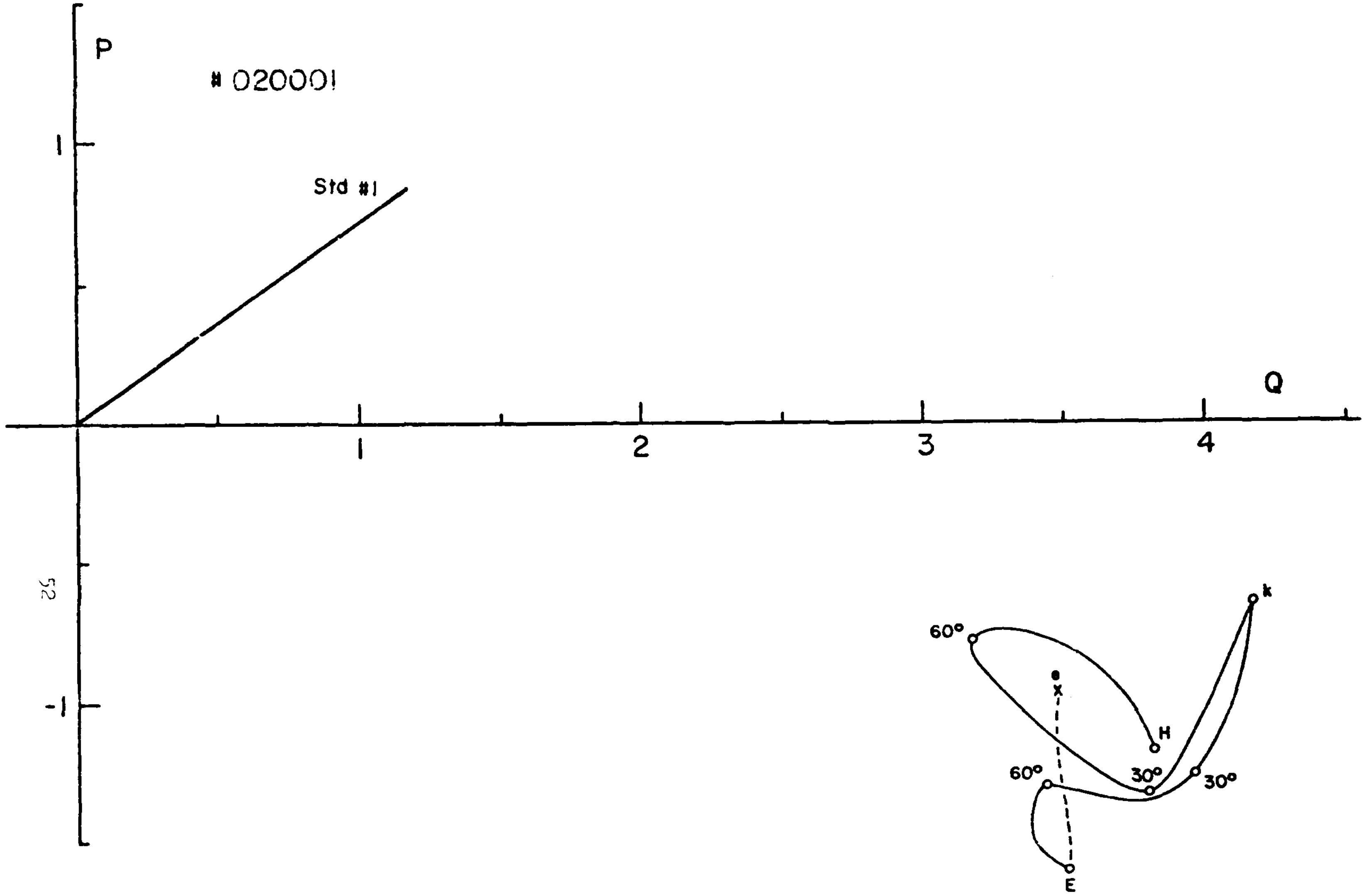

Fig. 11A An experimental forward-scattering P-Q plot for a rough particle (Cf Fig. 5C and Table IV). This displays the dependence of the complex forward-scattering amplitude S(0) on the target orientation angle as the latter is continously varied (Cf Fig. 1). A vector from the origin to each point on these curves represents S(0) at that orientation; the tilt from the P-axis is the phase shift of the forward-scattered wave, while the length is $|S(0)|$ as measured against that of the standard sphere of known $|S(0)|$ (Cf Table I). Since the particle lacks cylindrical symmetry, continous target rotations were made in 3 discreet ways: k-E rotation=target axis swept in $\vec{k}_o-\vec{E}_o$ plane of the incident wave; k-H rotation=axis swept in $\vec{k}_o-\vec{H}_o$ plane; and E-e rotation =30° rotation about the axis at $\vec{E}_o$ orientation. In particular, k, E and H denote, respectively, the orientations in which the particle-fixed plane containing the axis and the largest geometrical cross section is parallel to $\vec{k}_o-\vec{E}_o$, $\vec{E}_o-\vec{H}_o$ and $\vec{k}_o-\vec{H}_o$ planes, in addition to the axis itelf being parallel to $\vec{k}_o$, $\vec{E}_o$ and $\vec{H}_o$. The projection of the S(0) vector at each orientation on the calibrated Q-axis gives the extinction efficiency, the total cross section divided by πa_v^2 at that orientation. πa_v^2 is the radius of the equal-vol sphere. ($x_v=ka_v=7.717$ and $m=1.356$)

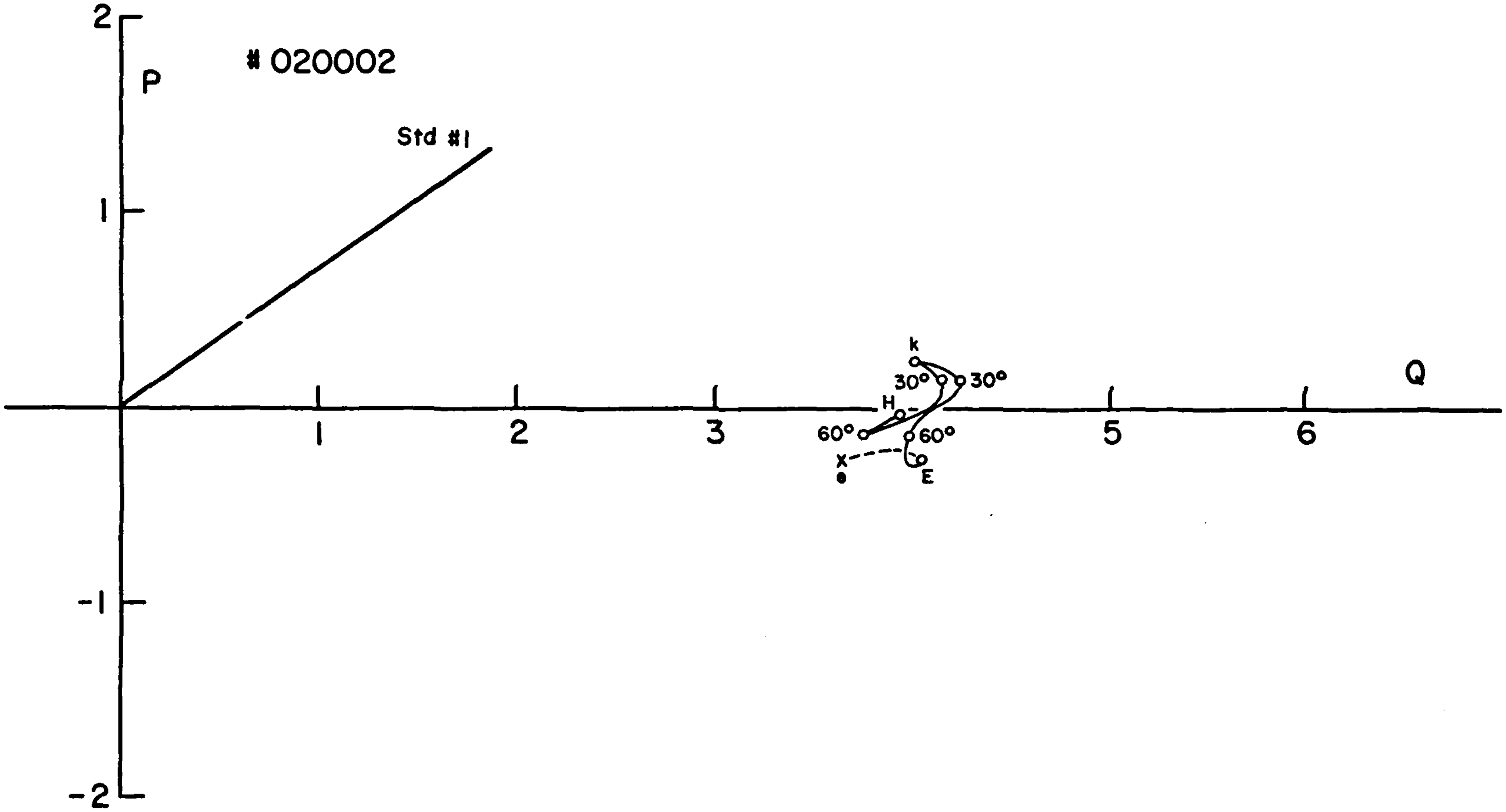

Fig. 11B Same as in Fig 11A except that the target parameters are x_V=6.108; m=1.362

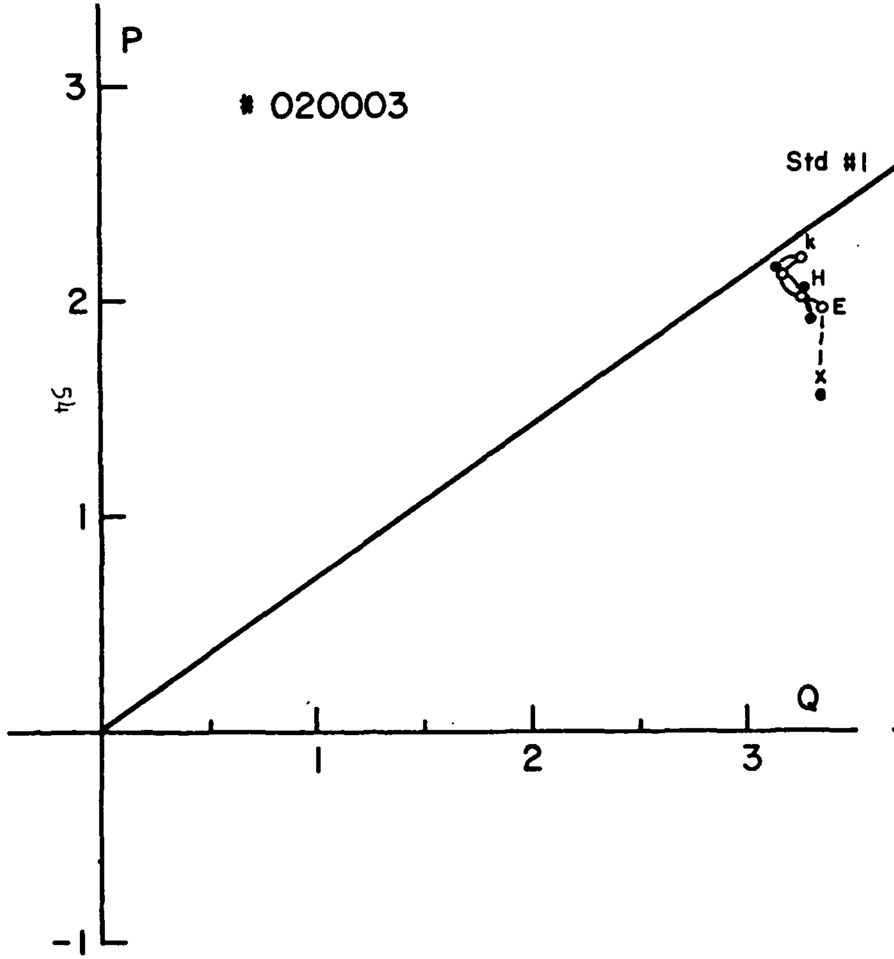

Fig. 11C Same as Fig. 11A except that target parameters are x_V=4.314; m=1.354

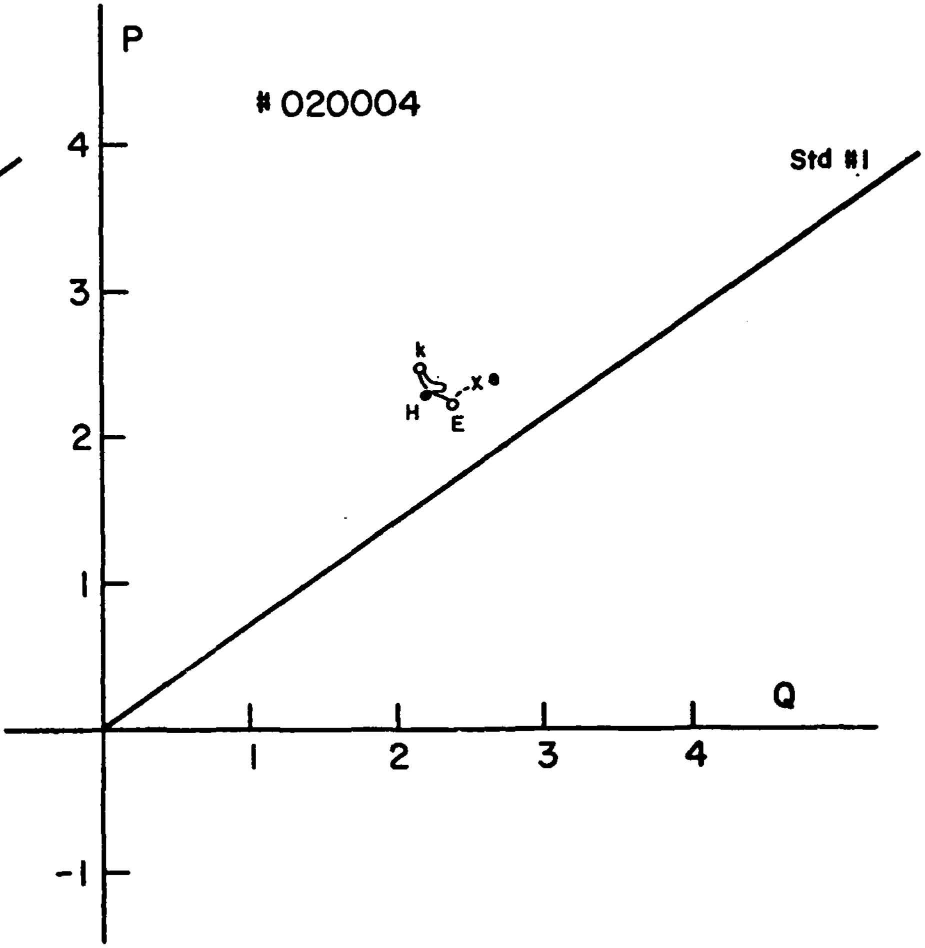

Fig. 11D Same as Fig. 11A except that target parameters are x_V=3.554; m=1.833

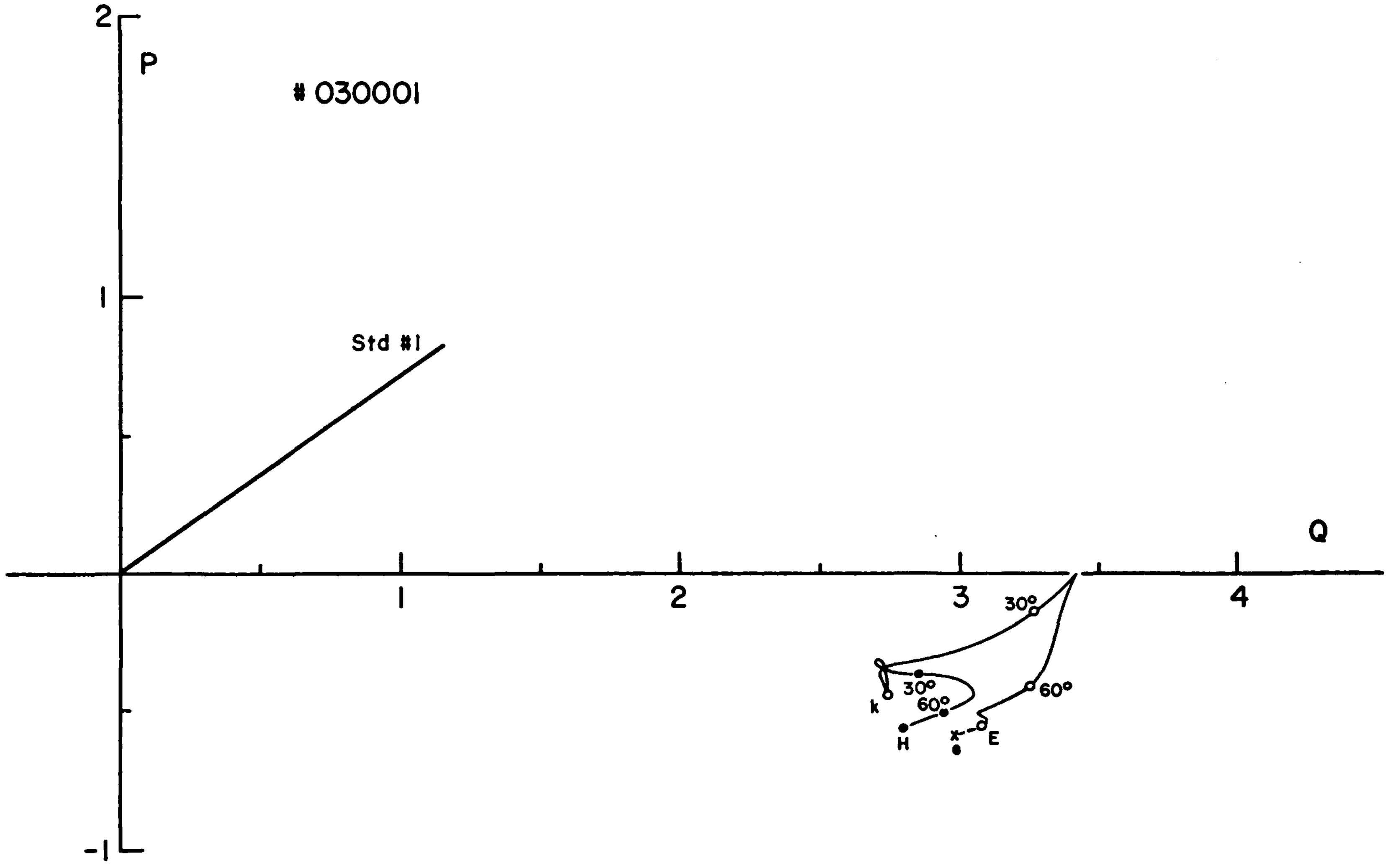

Fig. 12A Same as in Fig. 11A except that the target parameters are x_V=7.756; m=∞

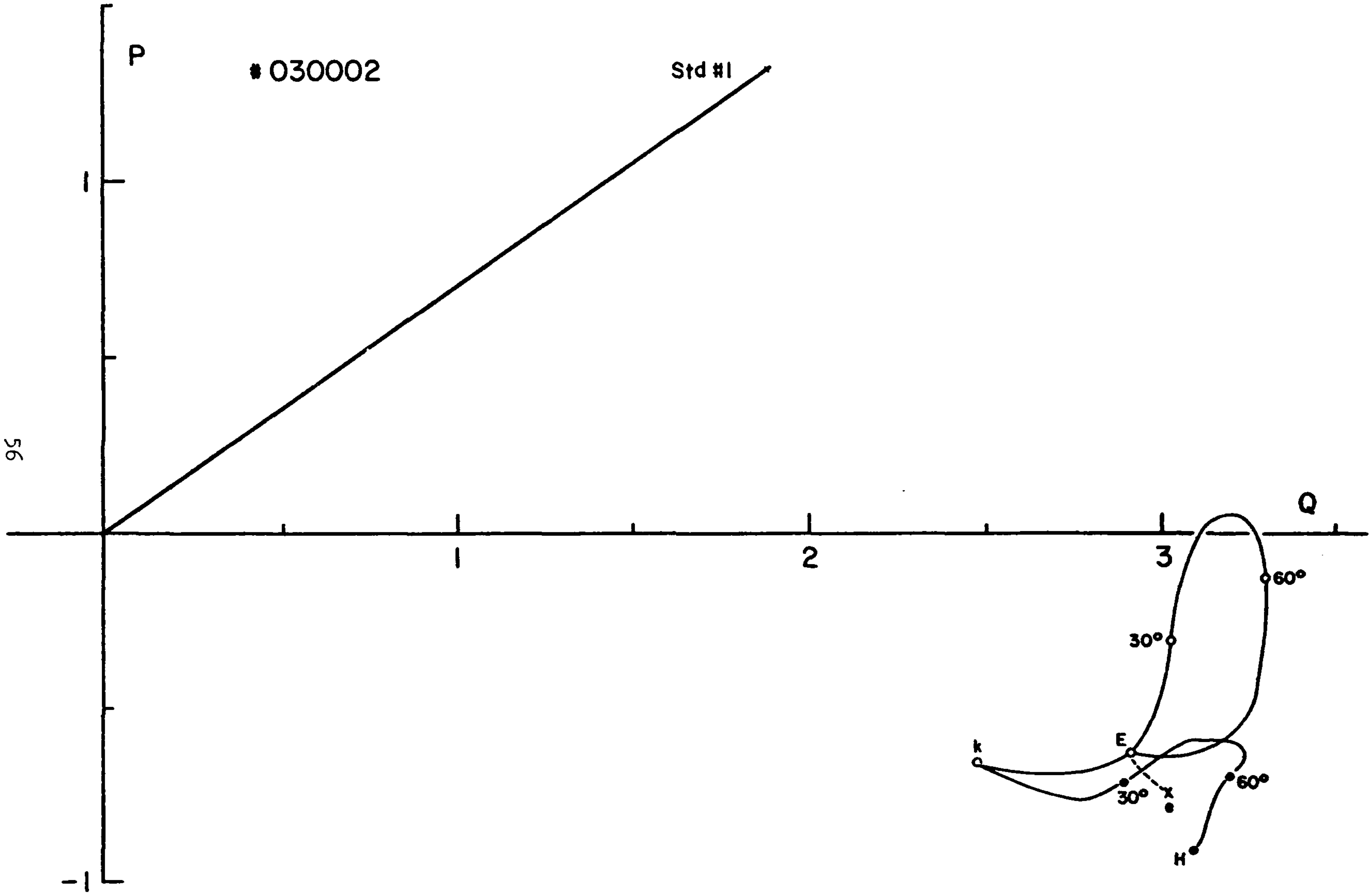

Fig. 12B Same as in Fig 11A except that the target parameters are x_V=6.107; m=∞

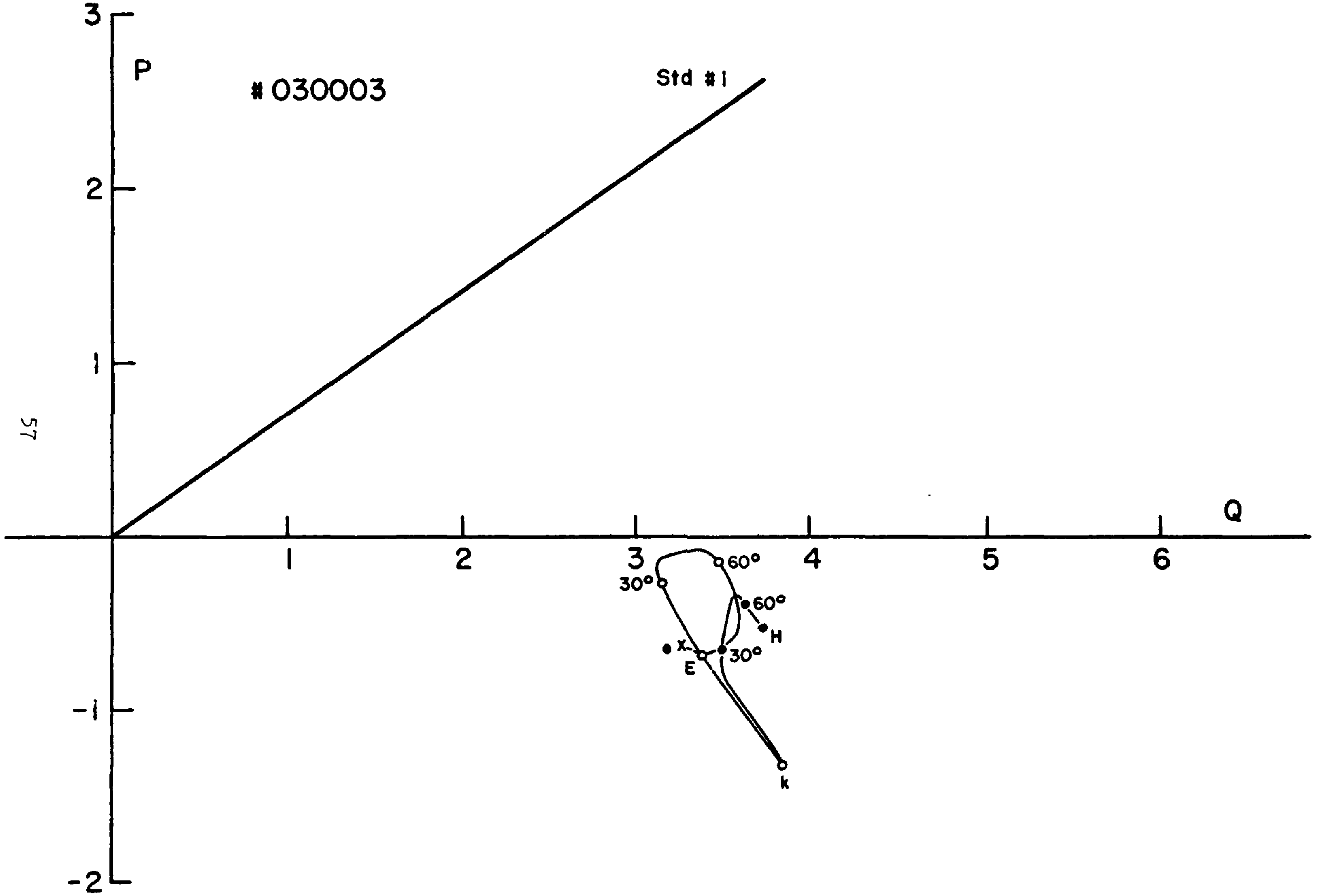

Fig. 12C Same as in Fig. 11A except that the target parameters are $x_V=4.329$; $m=\infty$

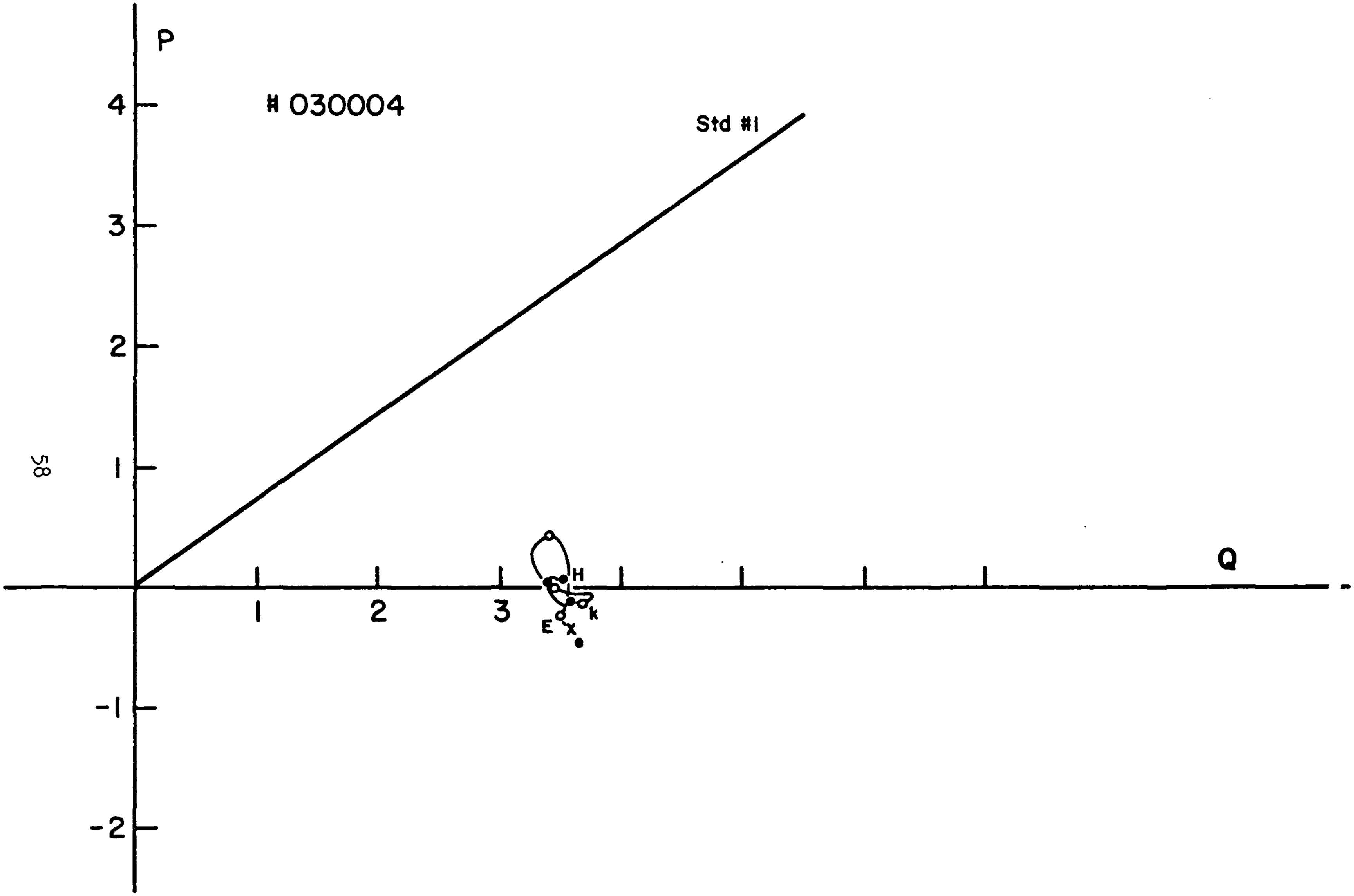

Fig. 12D Same as in Fig. 11A except that the target parameters are x_V=3.570; m=∞

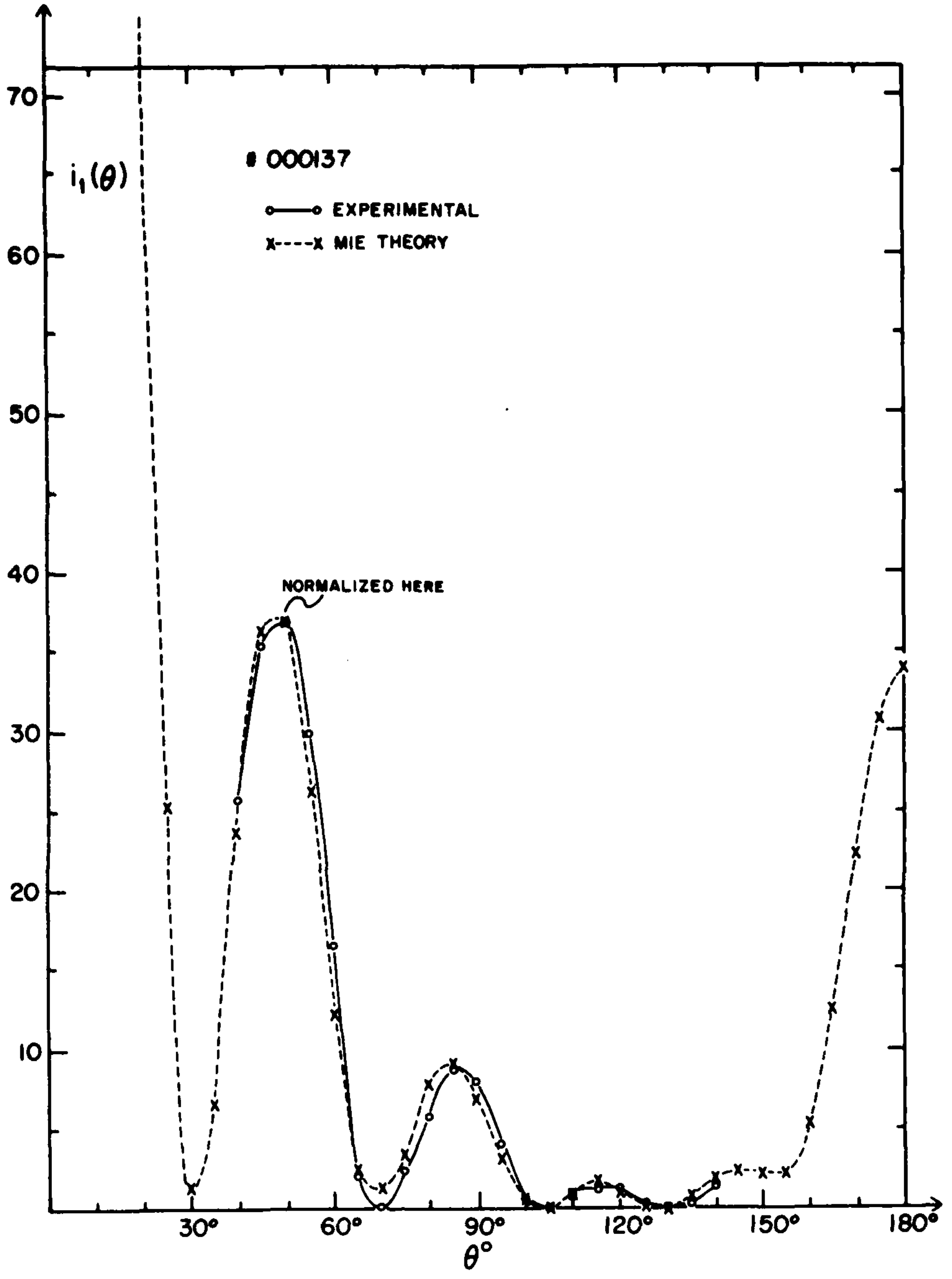

Fig. 13A Angular distribution $i_1(\theta)$ plotted against the scattering angle θ for a spherical particle. $i_1(\theta)$ is the component of intensity of the scattered wave along the direction perpendicular to the scattering plane, the plane formed by $\vec{k}_o$ and $\vec{k}$ in Fig. 1. Polarization of the incident wave is also perpendicular and the target has a size parameter $x=4.978$ and a refractive index $m=1.610-i0.004$ (Table I). The solid curve connects the experimental points measured by the device shown in Fig. 4, while the dashed curve is the Mie theory prediction with the same x and with $m=1.610$, normalized at $\theta=50^{o}$. A minimum number of absorbers were used on the floor and the side walls.

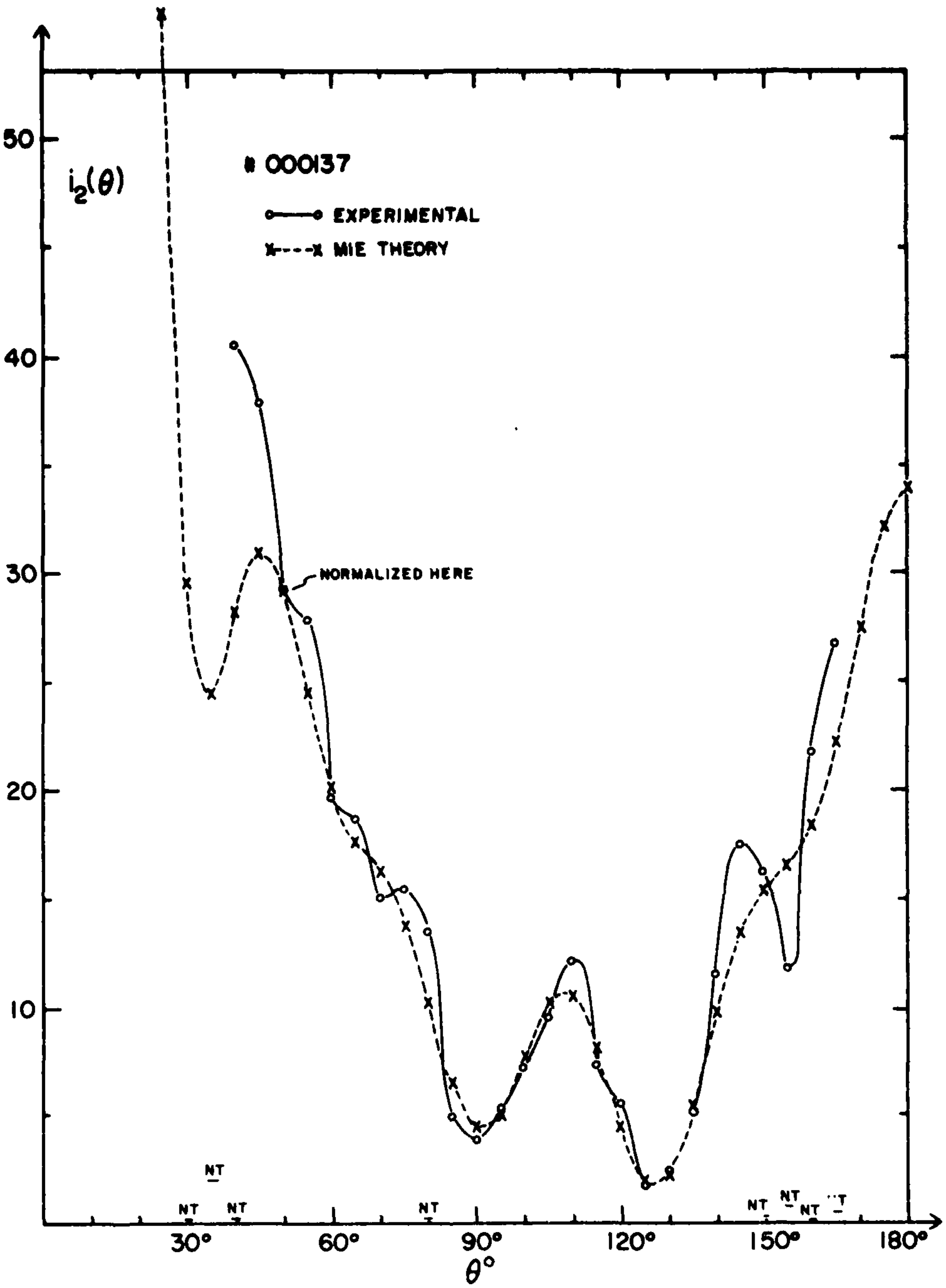

Fig. 13B Angular distribution $i_2(\theta)$ plotted against the scattering angle θ for the same particle as in Fig. 13A. $i_2(\theta)$ is the component of scattered intensity parallel to the scattering plane. Incident polarization is also parallel, and the same device as in Fig. 4 is used to obtain the experimental points along the solid curve. The dashed curve is the Mie theory result for $x=4.978$ and $m=1.610$, normalized at $\theta=50^{\circ}$. The background intensity level in the absence of the target is shown by NT at some scattering angles. A minimum number of microwave absorbers were placed on the floor and on the side walls.

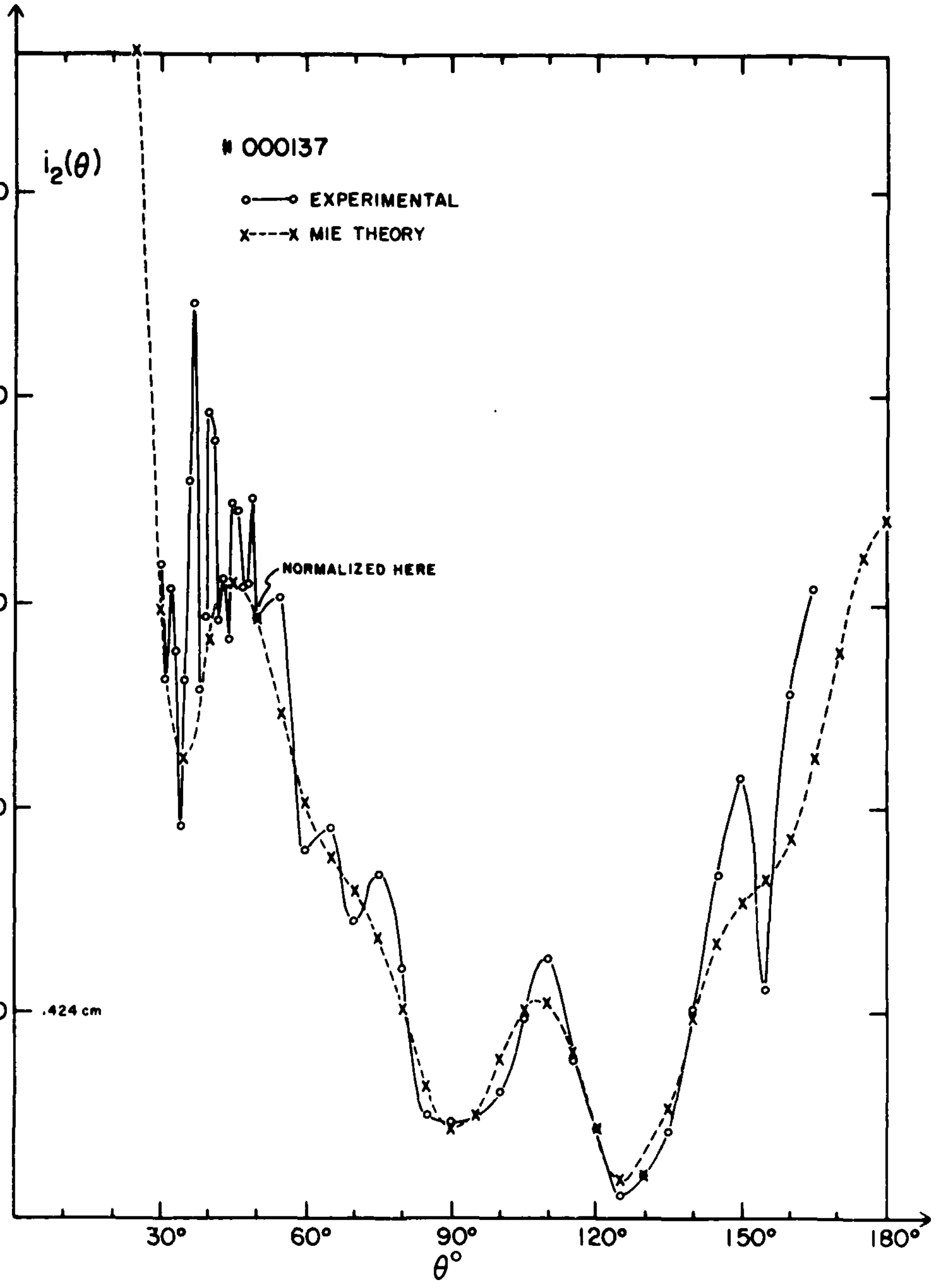

Fig. 13C Same $i_1(\Theta)$ vs Θ plot as in Fig. 13B except that the number of absorbers on the side wall opposite the receiver antenna was increased. Notice that over $30^o \leq \Theta \leq 50^o$ the measurement were made at $\Delta\Theta=1^o$ intervals to show the combined effect of background radiation and the uneven floor.

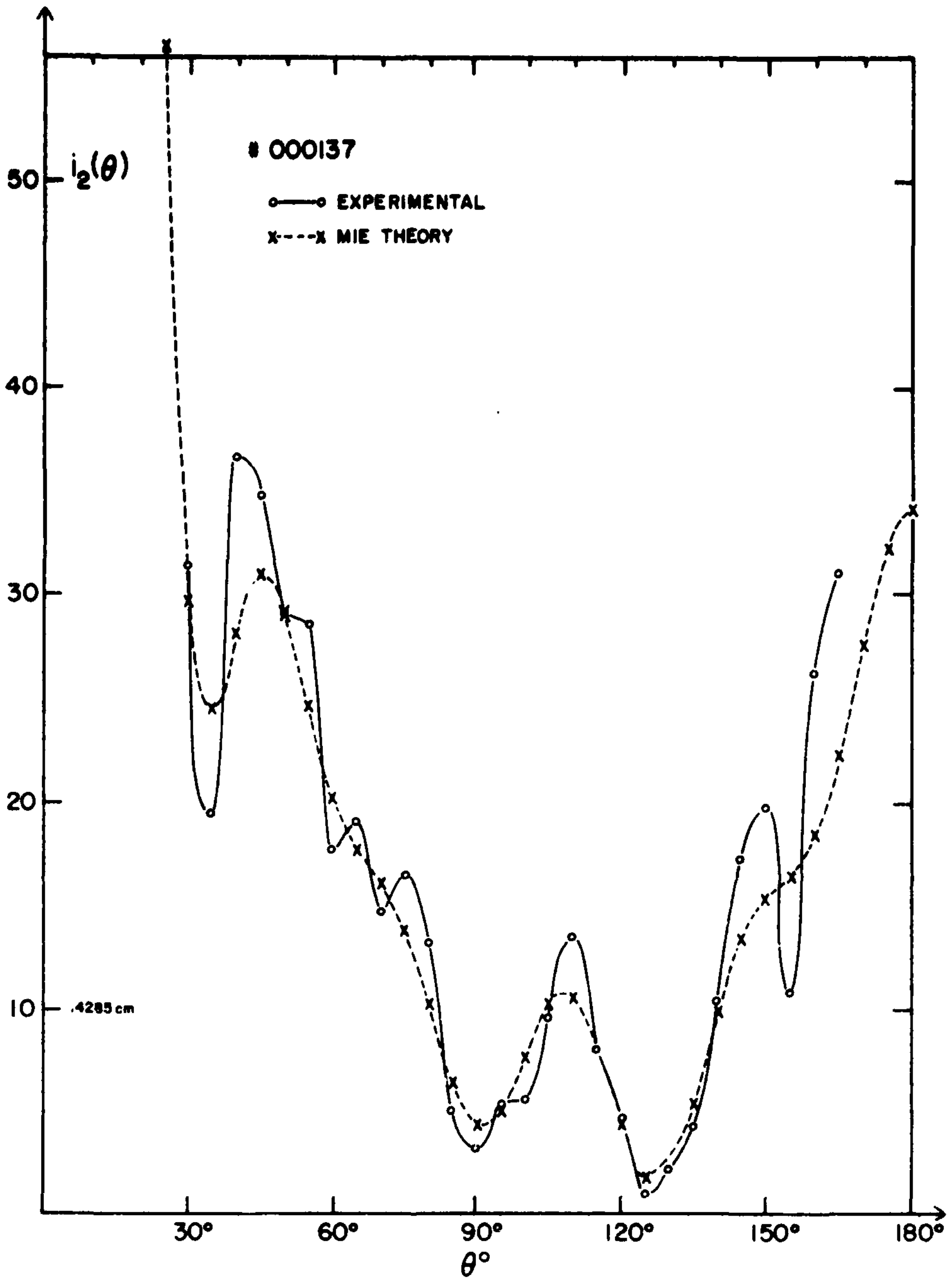

Fig. 13D Same $i_2(\theta)$ vs θ plot as in Figs. 13B and 13C except that the critical portions of the side wall and the floor were covered by absorbers wherever possible.

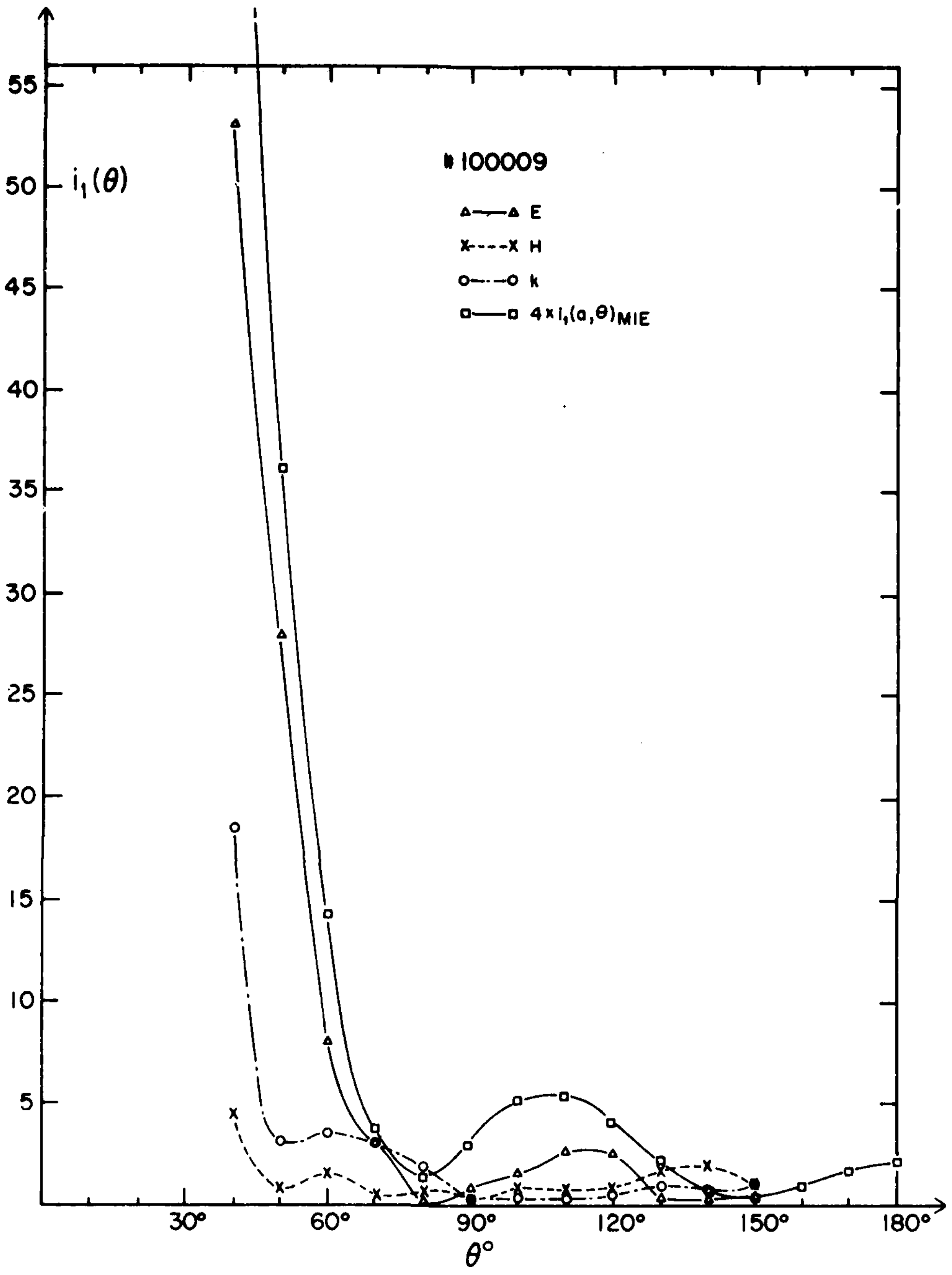

Fig. 14A Intensity of scattering $i_1(\theta)$ plotted against the scattering angle θ for a spheroidal particle. $i_1(\theta)$ is the intensity perpendicular to the scattering plane, a plane formed by $\vec{k}_o$ and $\vec{k}$ vectors in Fig. 1, and the incident wave polarization is also perpendicular to this plane. The experimental set-up used is shown in Fig. 4. At each θ, $i_1(\theta)$ was measured for 3 principal orientations of the spheroid, $\underline{k}$, E and H, in which the symmetry axis is parallel to $\vec{k}_o$, $\vec{E}_o$ and $\vec{H}_o$ of the incident radiation, respectively. The spheroid has the size parameter (a=semiminor axis) ka=2.507 and a refractive index m=1.610-i0.004 (Cf. Table V). The Mie theory prediction of $4x\ i_1(\theta)$ for a sphere with the same a and with m=1.610, is also shown as a separate curve.

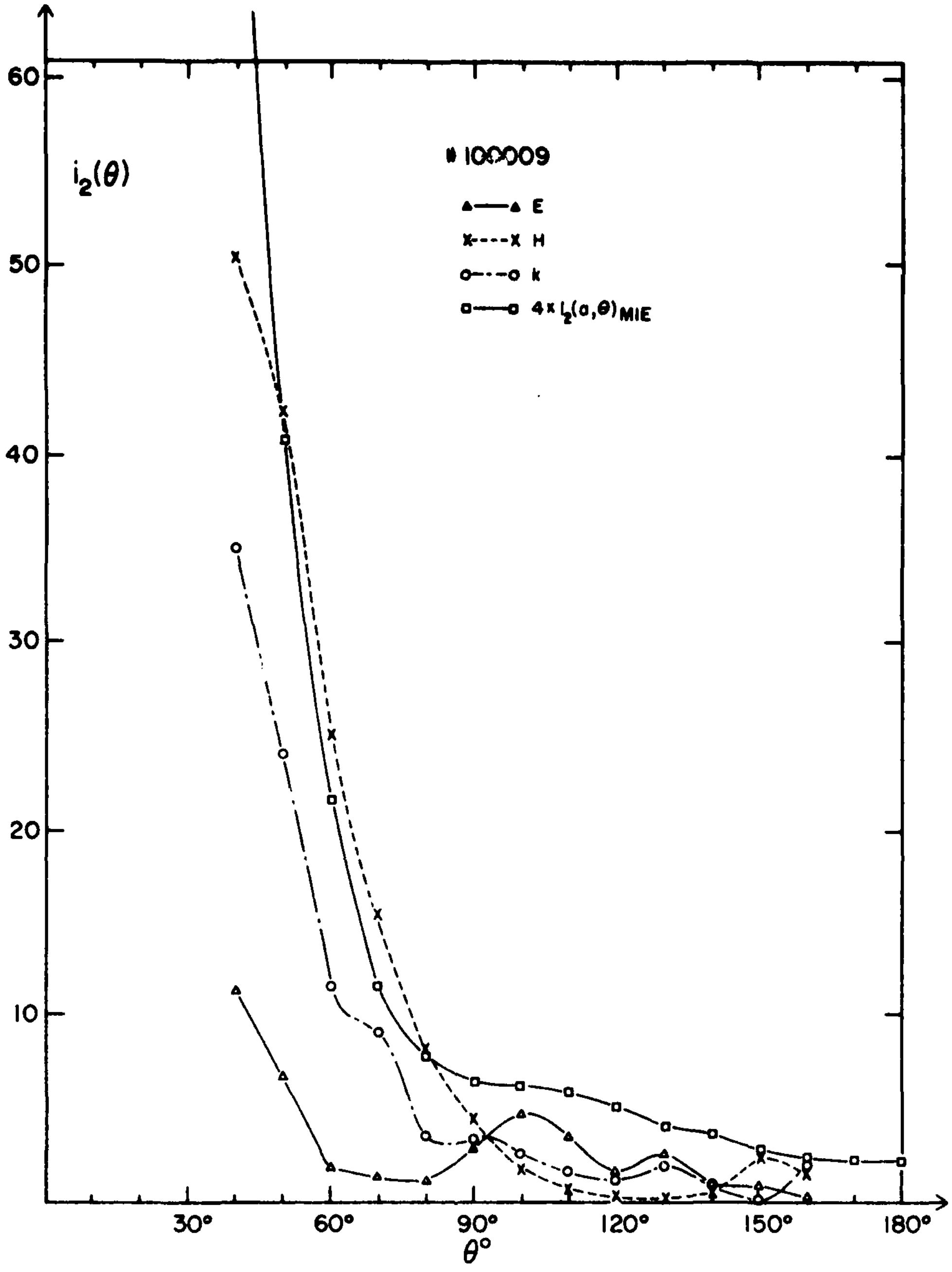

Fig. 14B The intensity of scattering $i_2(\theta)$ plotted against the scattering angle θ for a spheroidal particle. $i_2(\theta)$ is the intensity parallel to the scattering plane, as was the incident polarization. Same notations as in Fig. 14A are used to indicate the target orientations. The target parameters are ka=2.507 and m-1.610-i0.004. The Mie theory prediction of 4x $i_2(\theta)$ for a sphere with the same a and with m=1.610 is also shown as a separate curve.

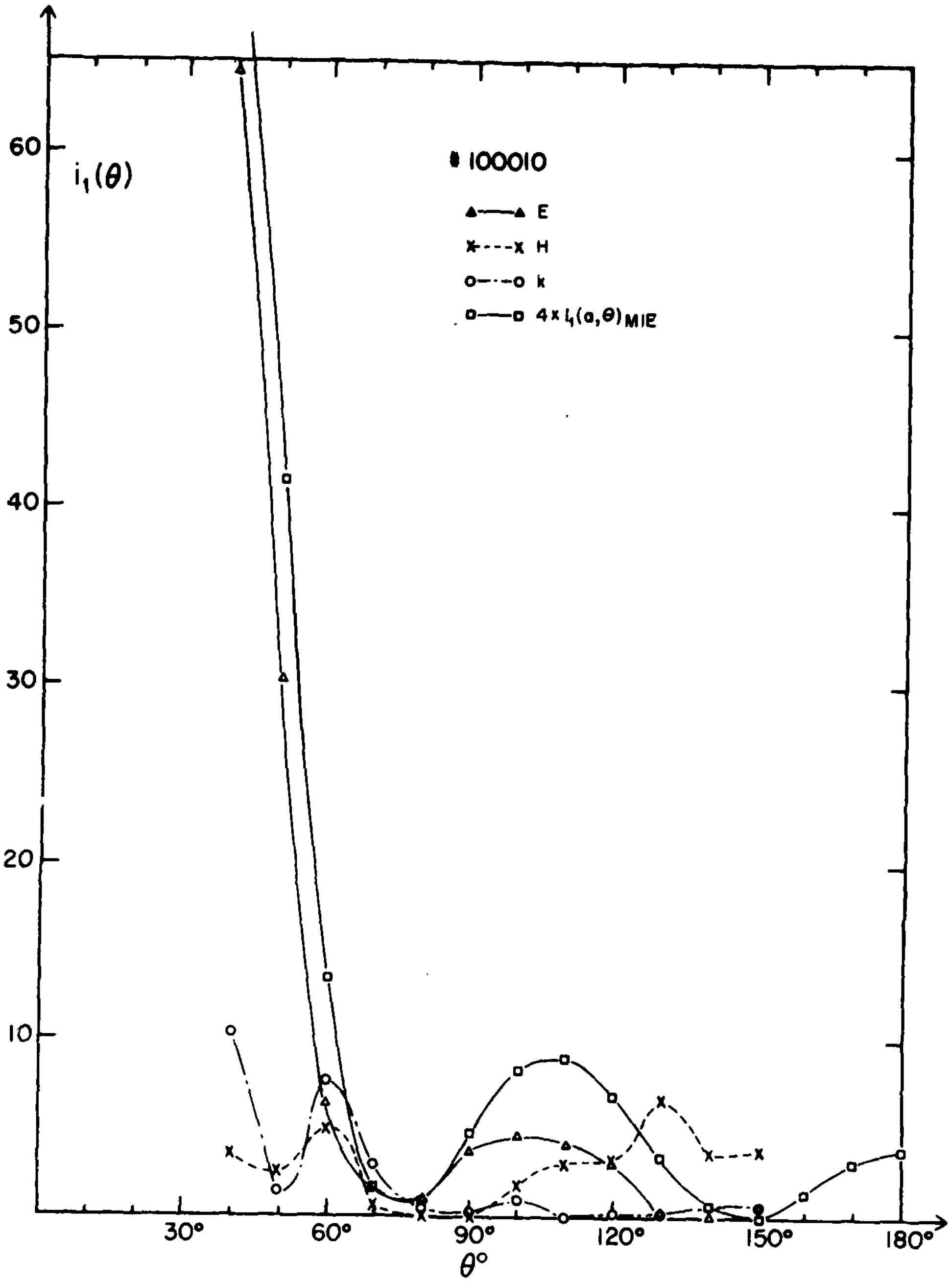

Fig. 15A Same $i_1(\theta)$ vs θ plot as in Fig. 14A, except that the size of the spheroid is such that ka=2.718.

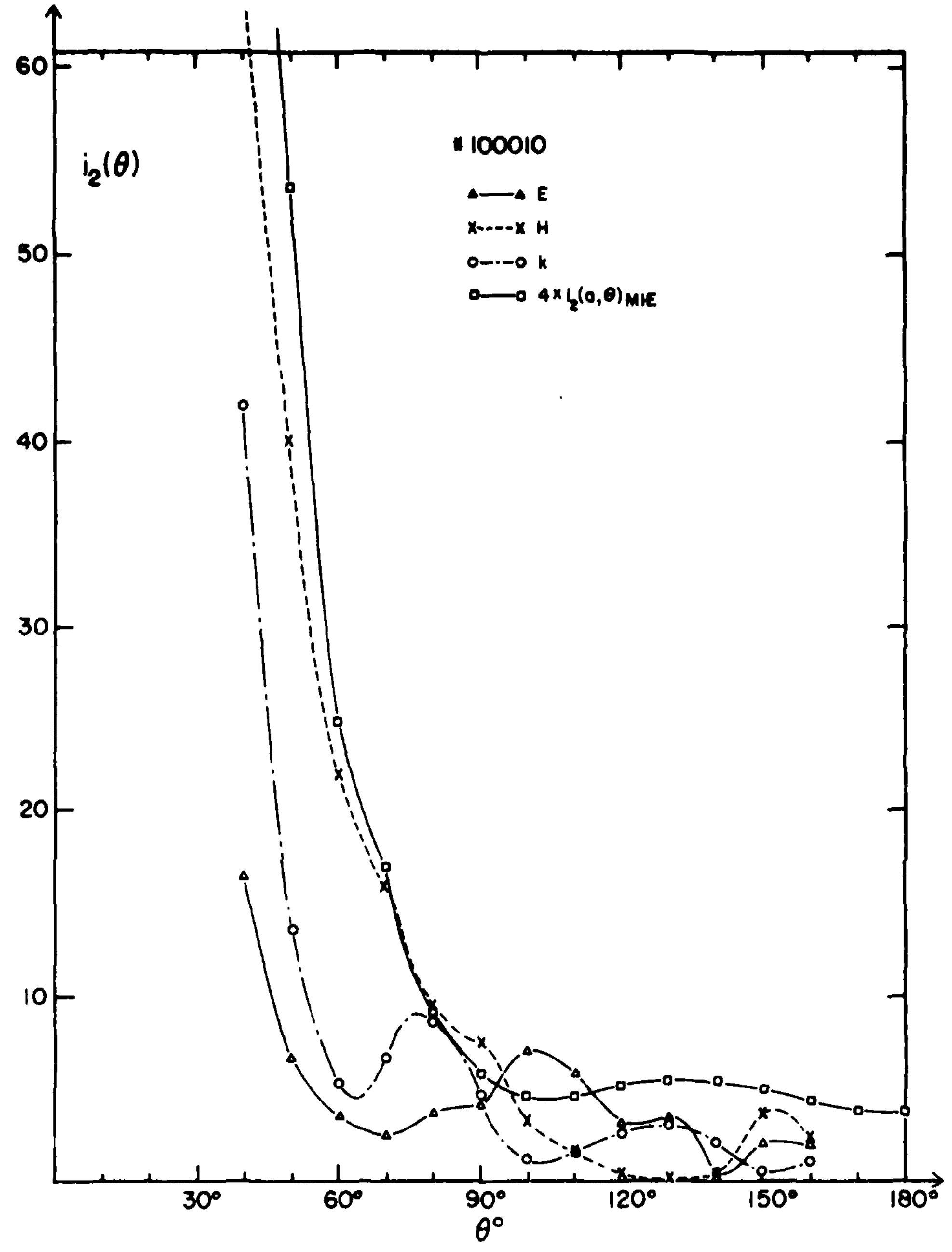

Fig. 15B Same $i_2(\theta)$ vs θ plot as in Fig. 14B, except that the size of the spheroid is such that ka=2.718.

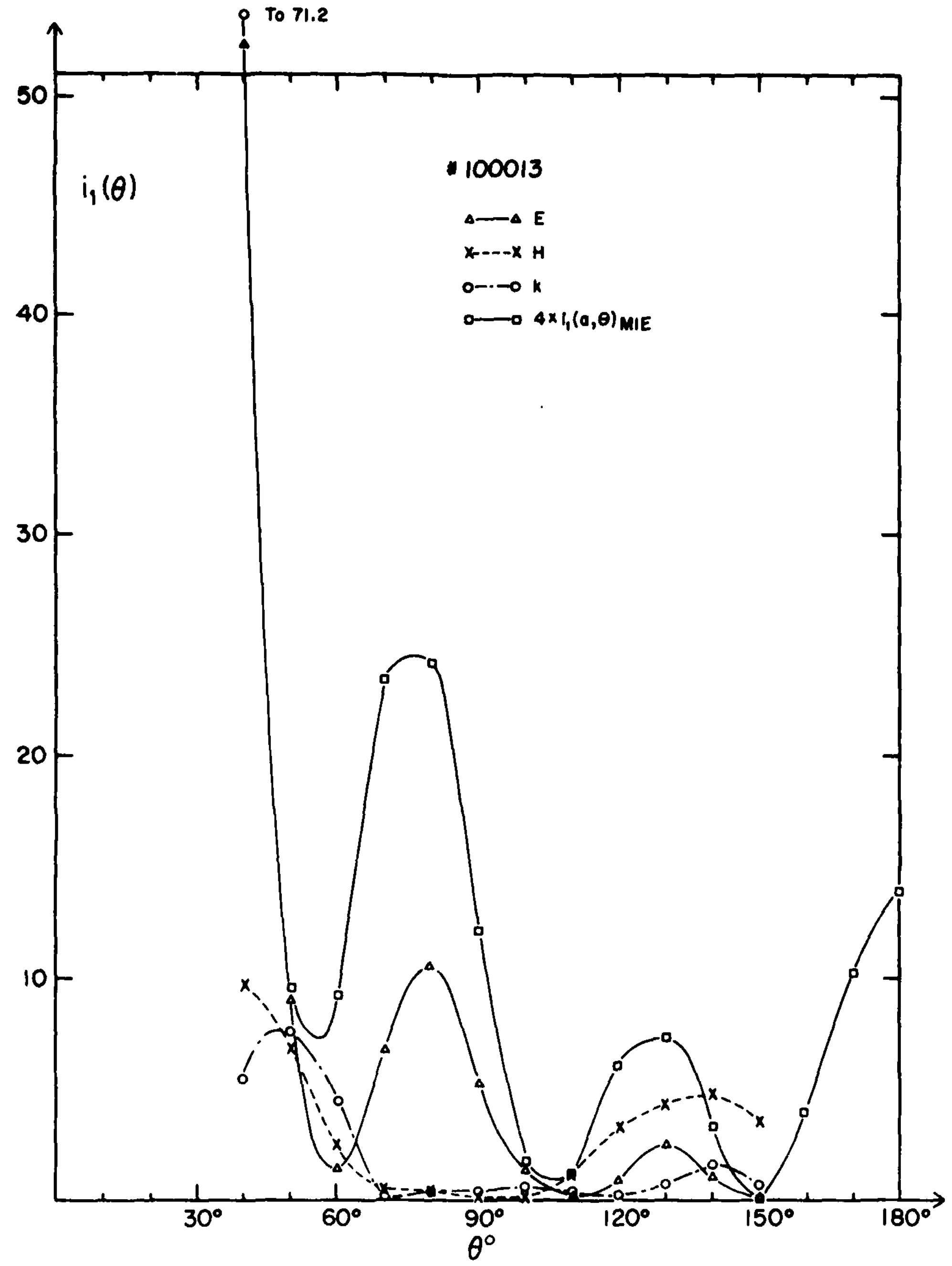

Fig. 16A Same $i_1(\theta)$ vs θ plot as in Fig.14A, except that the size of the spheroid is such that ka=3.359.

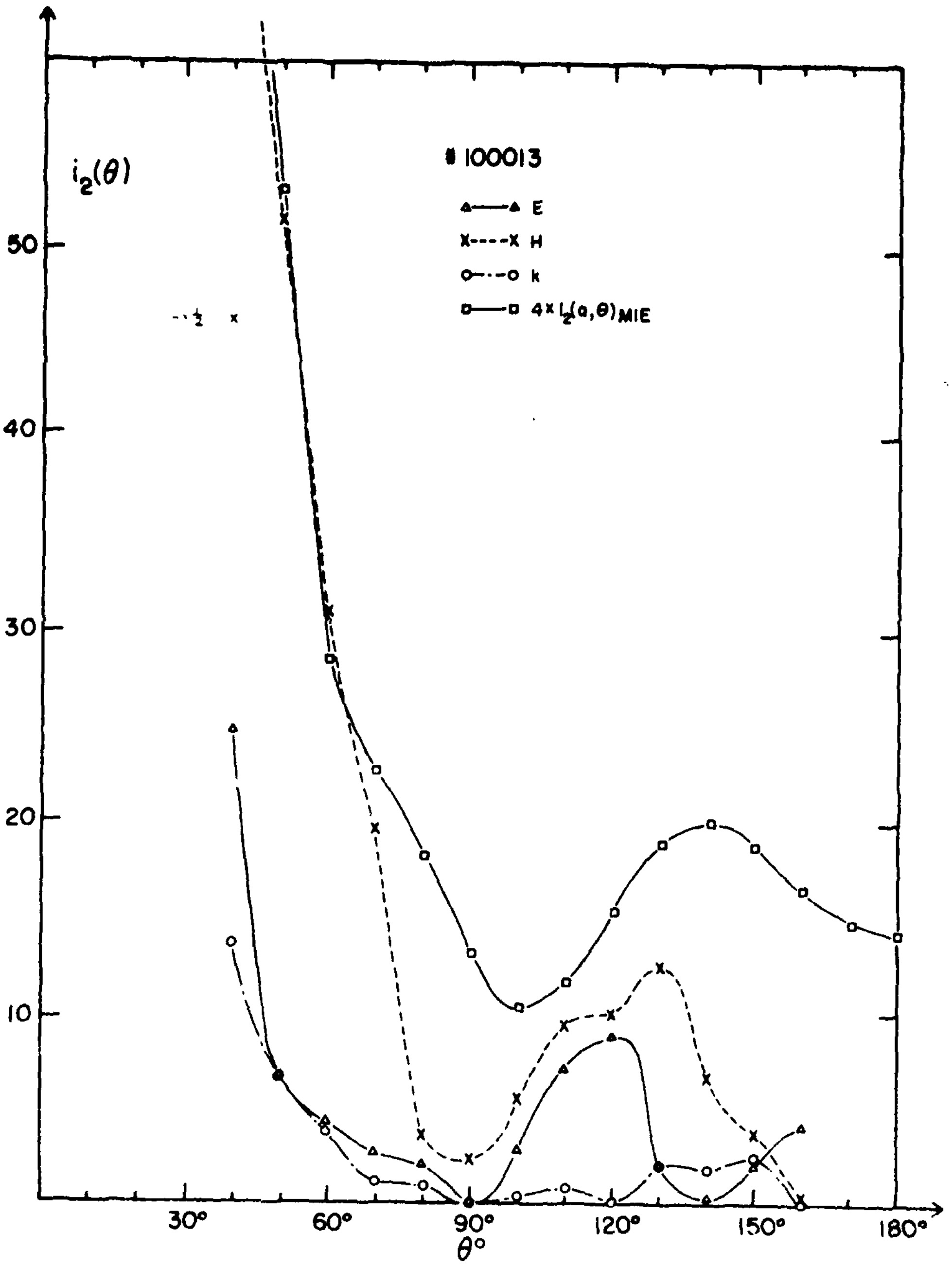

Fig. 16B Same $i_2(\theta)$ vs θ plot as in Fig. 14B except that the size of the spheroid is such that ka=3.359.

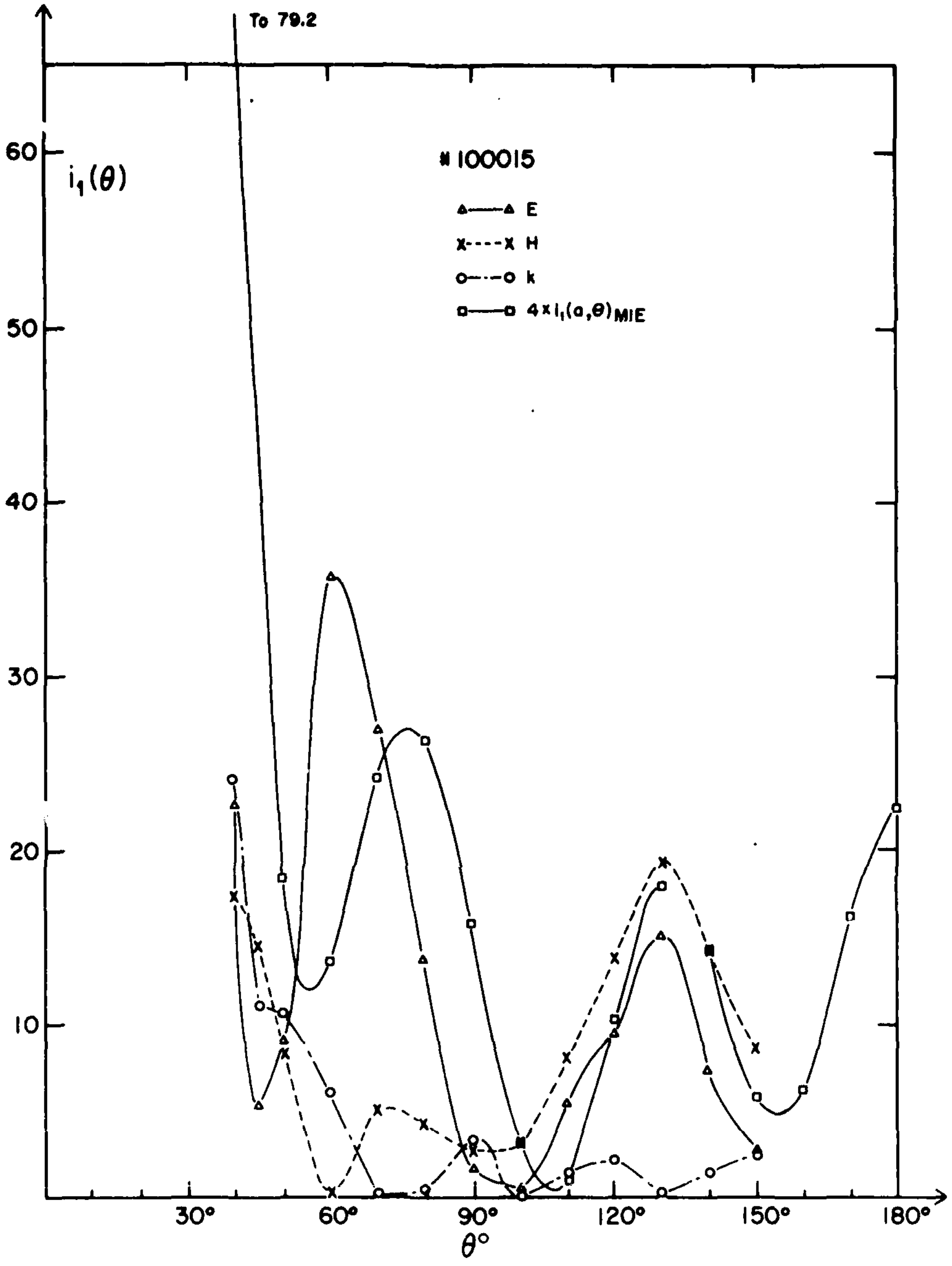

Fig. 17A Same $i_1(\theta)$ vs Θ plot as in Fig. 14A, except that the size of the spheroid is such that ka=3.754.

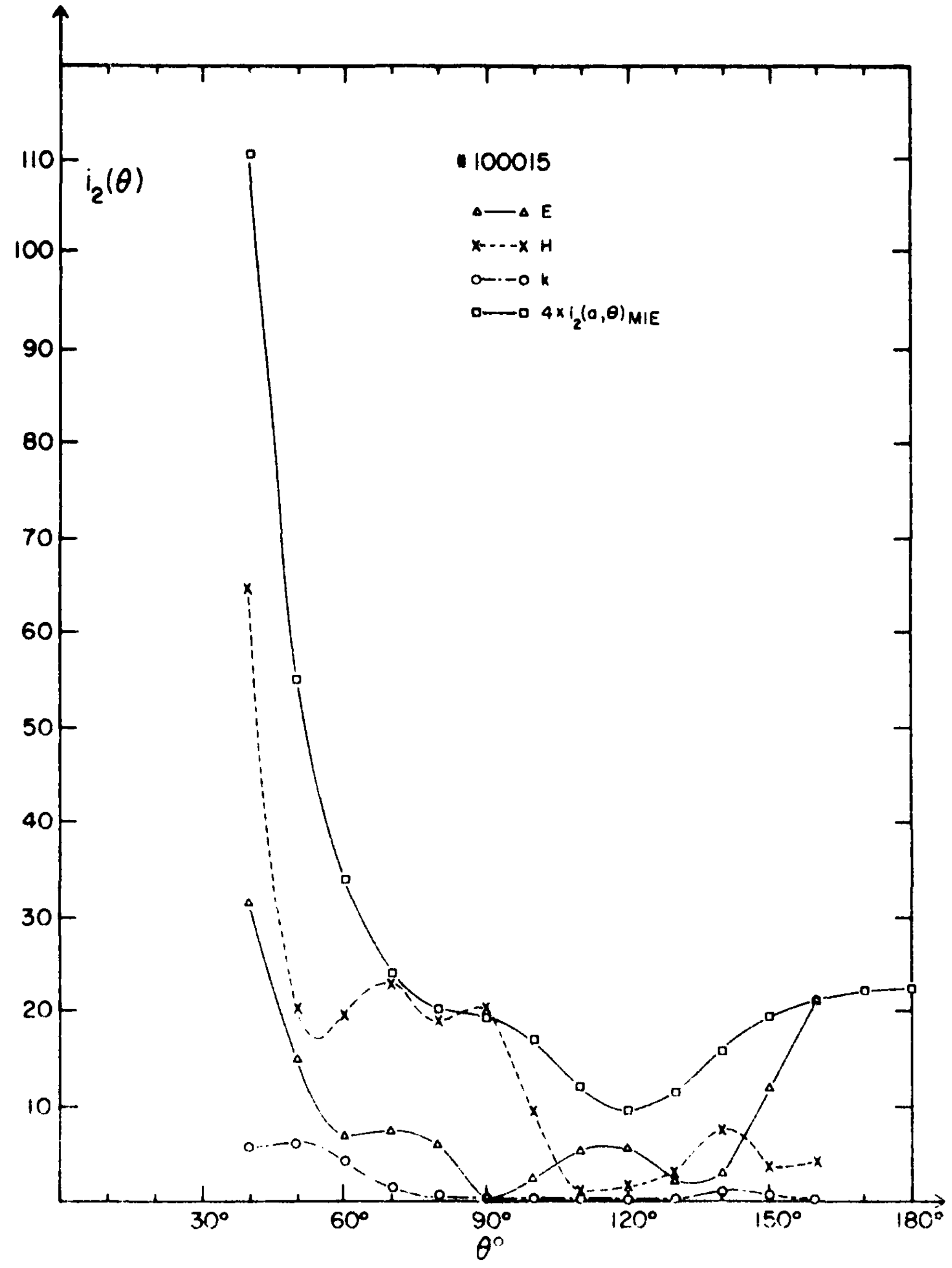

Fig. 15B Same $i_2(\theta)$ vs θ plot as in Fig. 14B, except that the size of the spheroid is such that ka=3.754.

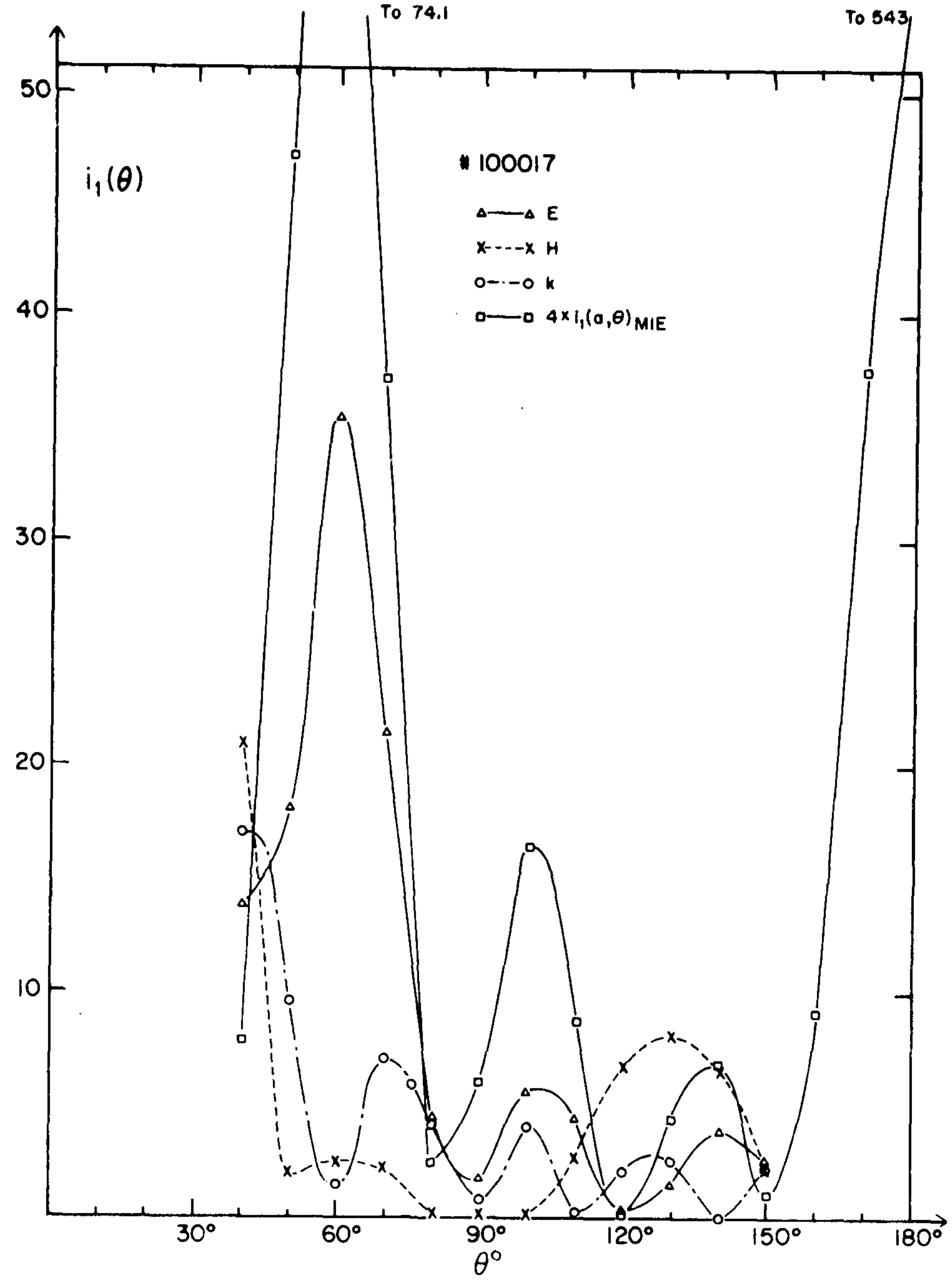

Fig. 18A Same $i_1(\theta)$ vs θ plot as in Fig. 14A, except that the size of the spheroid is such that ka=4.175.

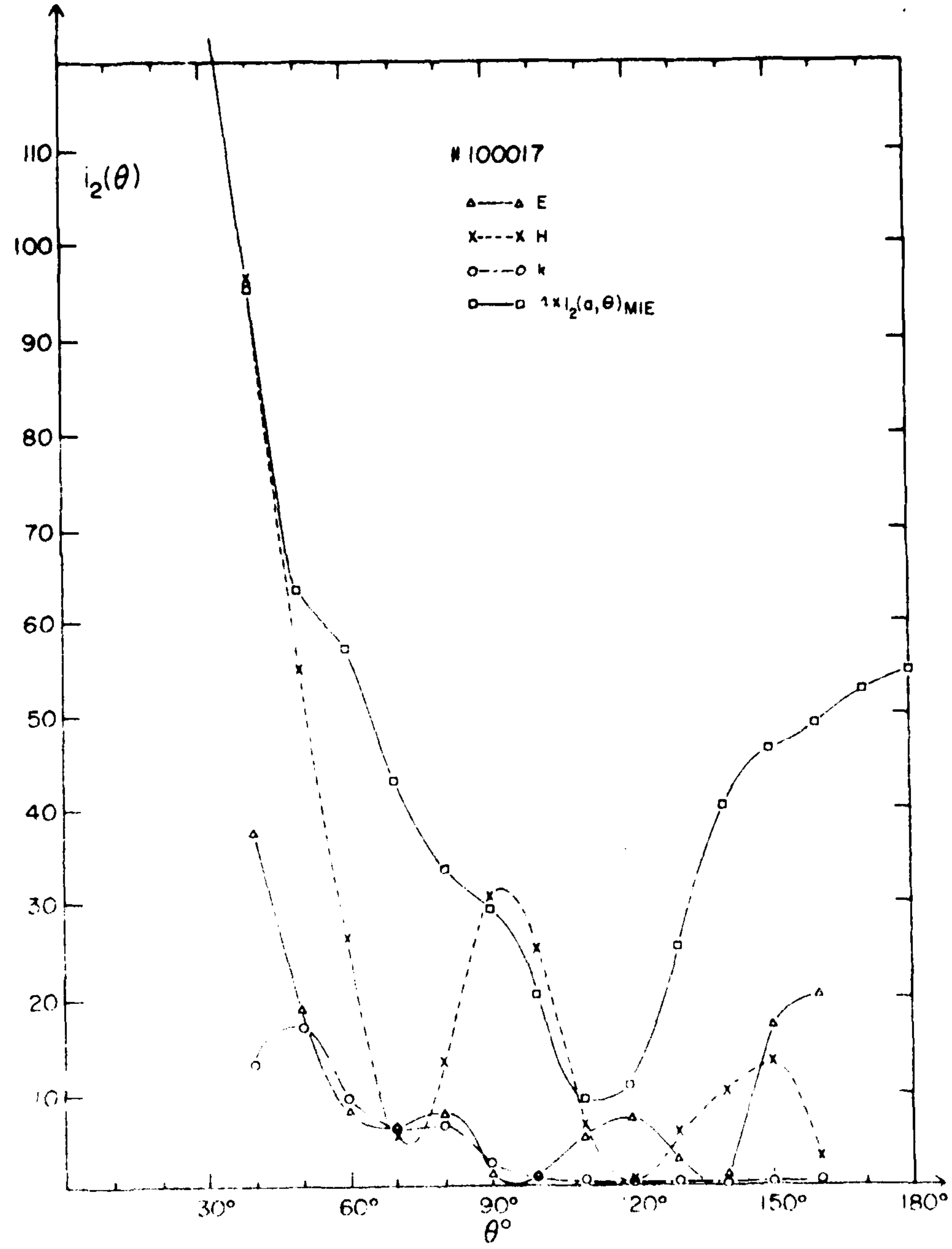

[illegible] Same [illegible] plotted in Fig. [illegible] except that the [illegible] concentric [illegible] such that ka = 4.175.

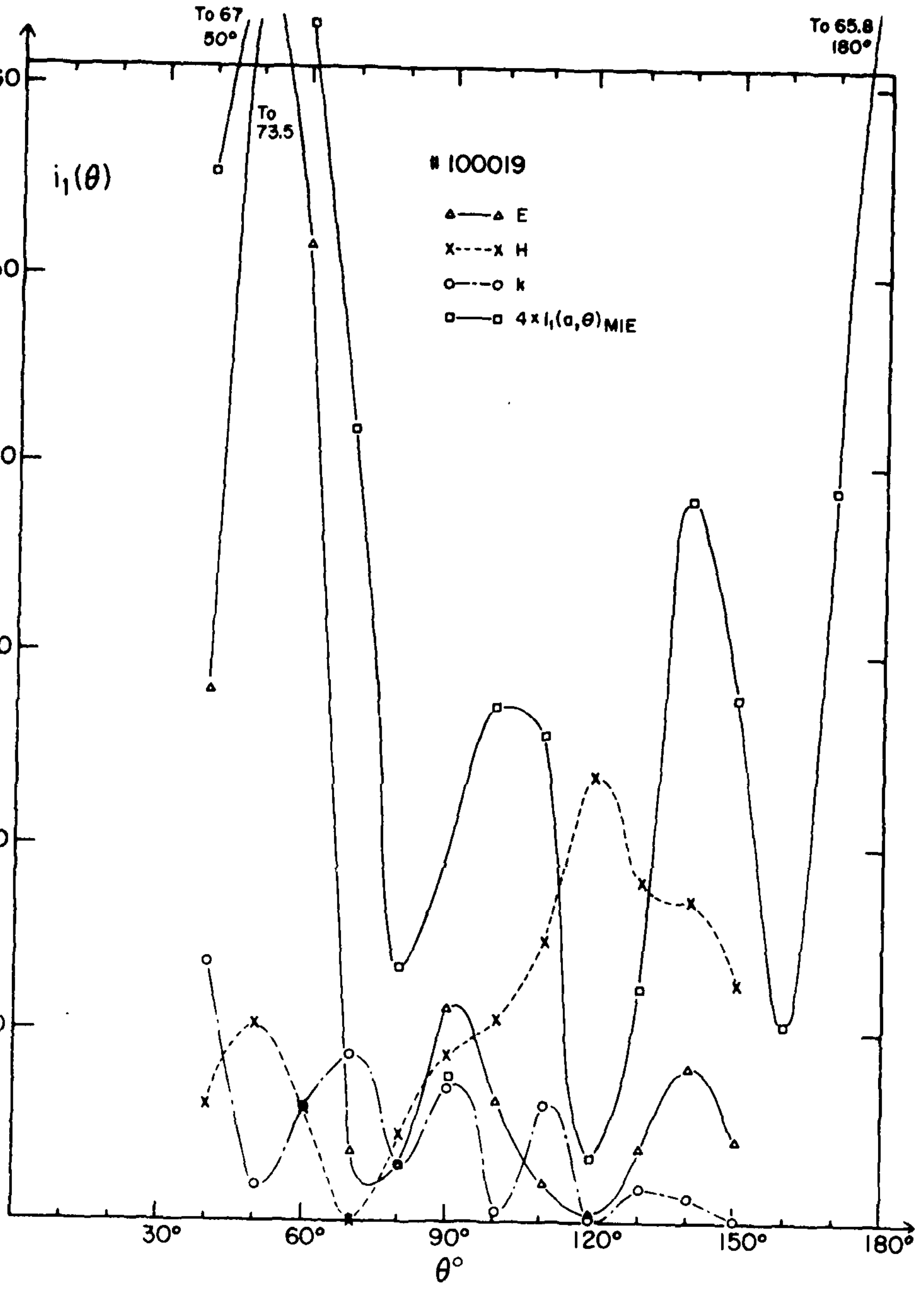

Fig. 19A Same $i_1(\theta)$ vs θ plot as in Fig. 14A, except that the size of the spheroid is such that ka=4.609.

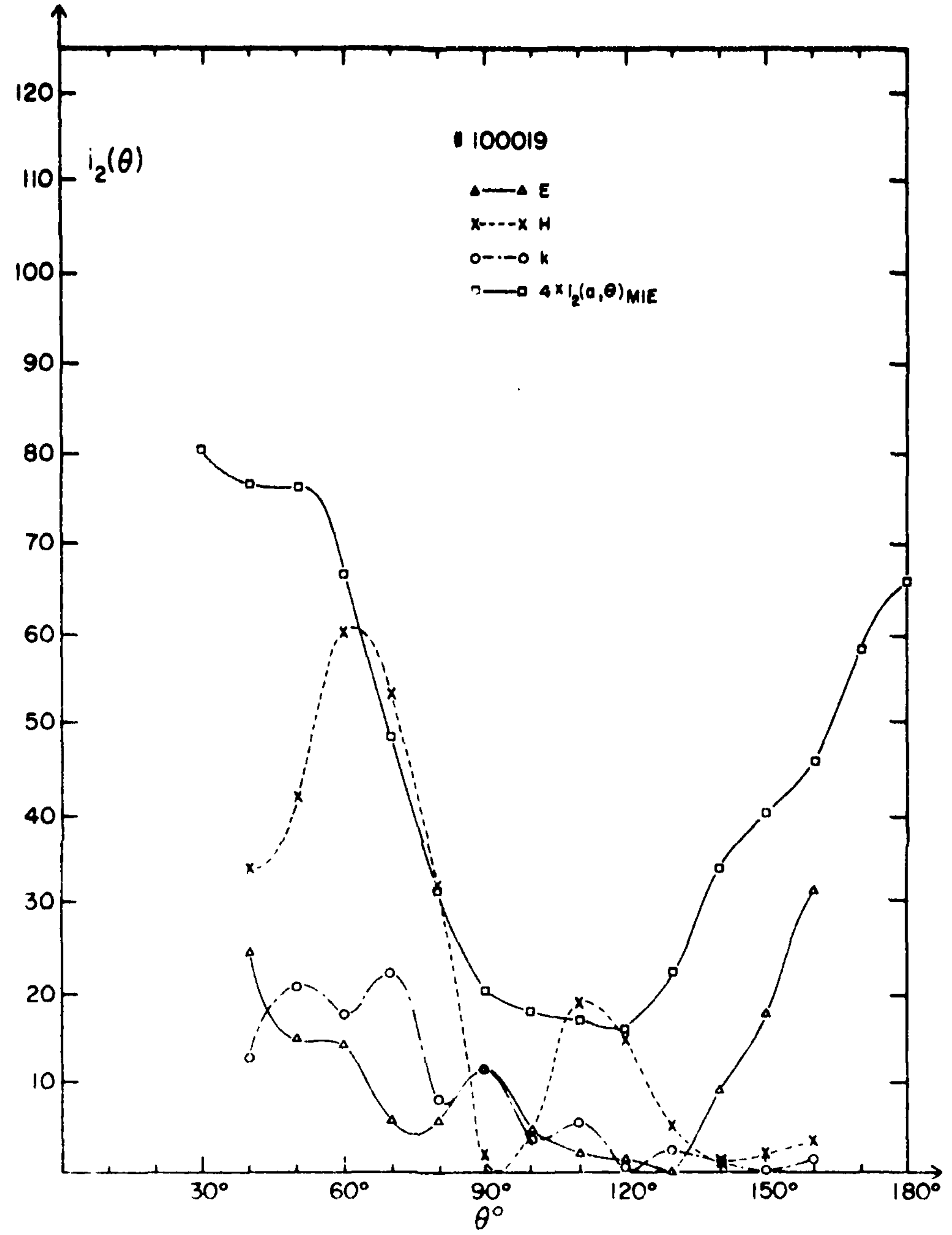

Fig. 19B Same $i_2(\theta)$ vs θ plot as in Fig. 14B, except that the size of the spheroid is such that ka=4.609.

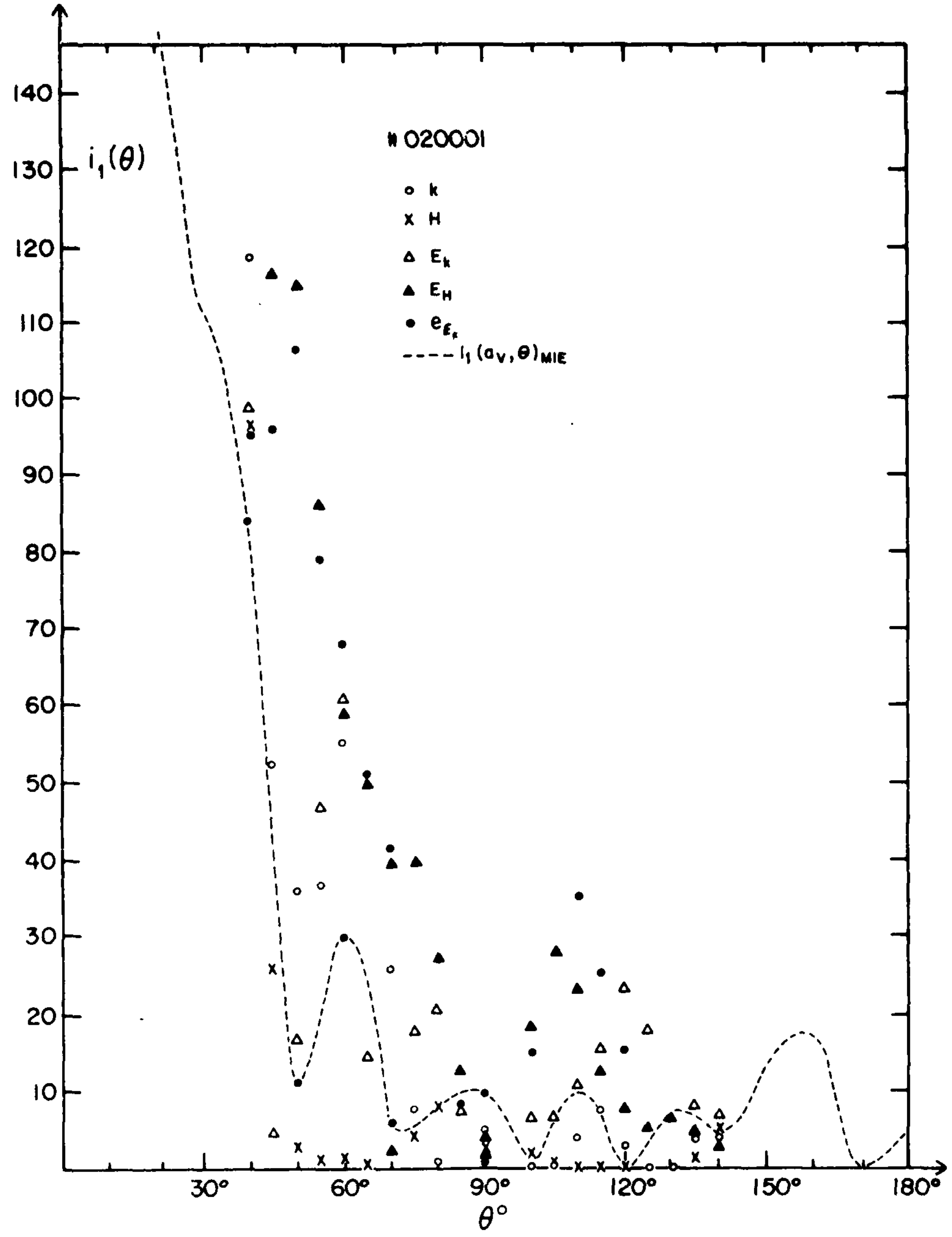

Fig. 20A Intensity of scattering $i_1(\theta)$ plotted against the scattering angle θ for a rough particle (Fig. 5C). $i_1(\theta)$ is the intensity component perpendicular to the scattering plane, a plane formed by $\vec{k}_o$ and $\vec{k}$ vectors in Fig. 1, and is also chosen to be a horizontal plane in the laboratory. The incident-wave polarization is also perpendicular and the target has a size parameter $x_V=ka_V=7.717$ and a refractive index m=1.356. The same notation as in forward-scattering (Fig. 11A) are used to indicate the target orientations k, E, and H. Suffixed notations E_k and E_H indicate, respectively, the same E orientation depending on whether this E was attained from the k or H orientation initially. e_{E_k} denotes that orientation reached from the E_k orientation by a 30° azimuthal rotation. The Mie theory prediction of $i_2(\theta)$ for a smooth sphere with the same radius a_V and refractive index m as this rough particle is also shown as a dotted curve.

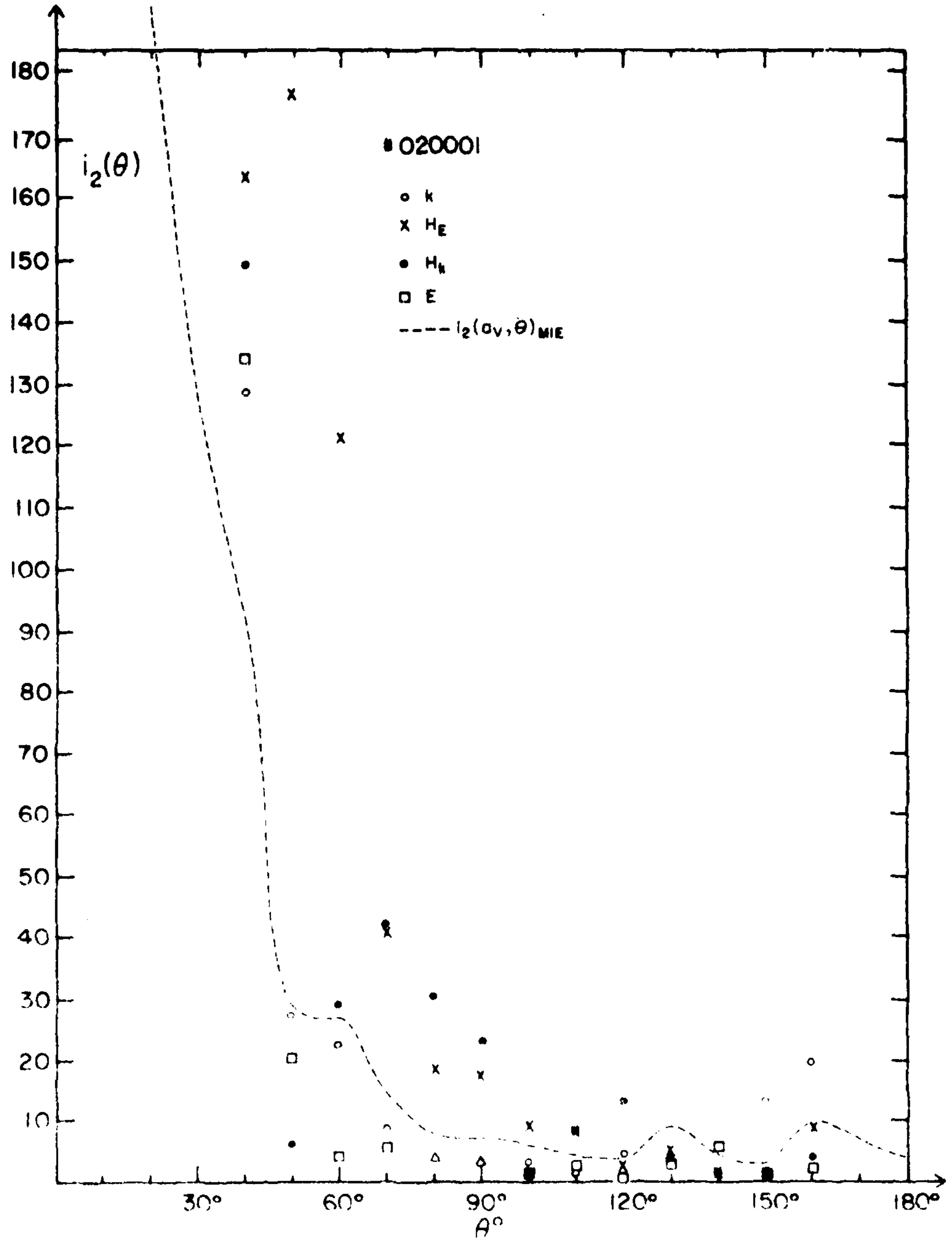

Fig. 20B Intensities of scattering $i_2(\theta)$ plotted against the scattering angle θ for a rough particle (Fig. 5C). $i_2(\theta)$ is the intensity component parallel to the scattering plane, the yz plane in Fig. 1. The incident wave polarization is also parallel and the target is the same as in Fig. 20A. Similar target-orientation notation as in Fig. 20A applies here. Mie theory result of $i_2(\theta)$ for the equal volume and equal-refractive-index smooth sphere is shown as a dotted curve.

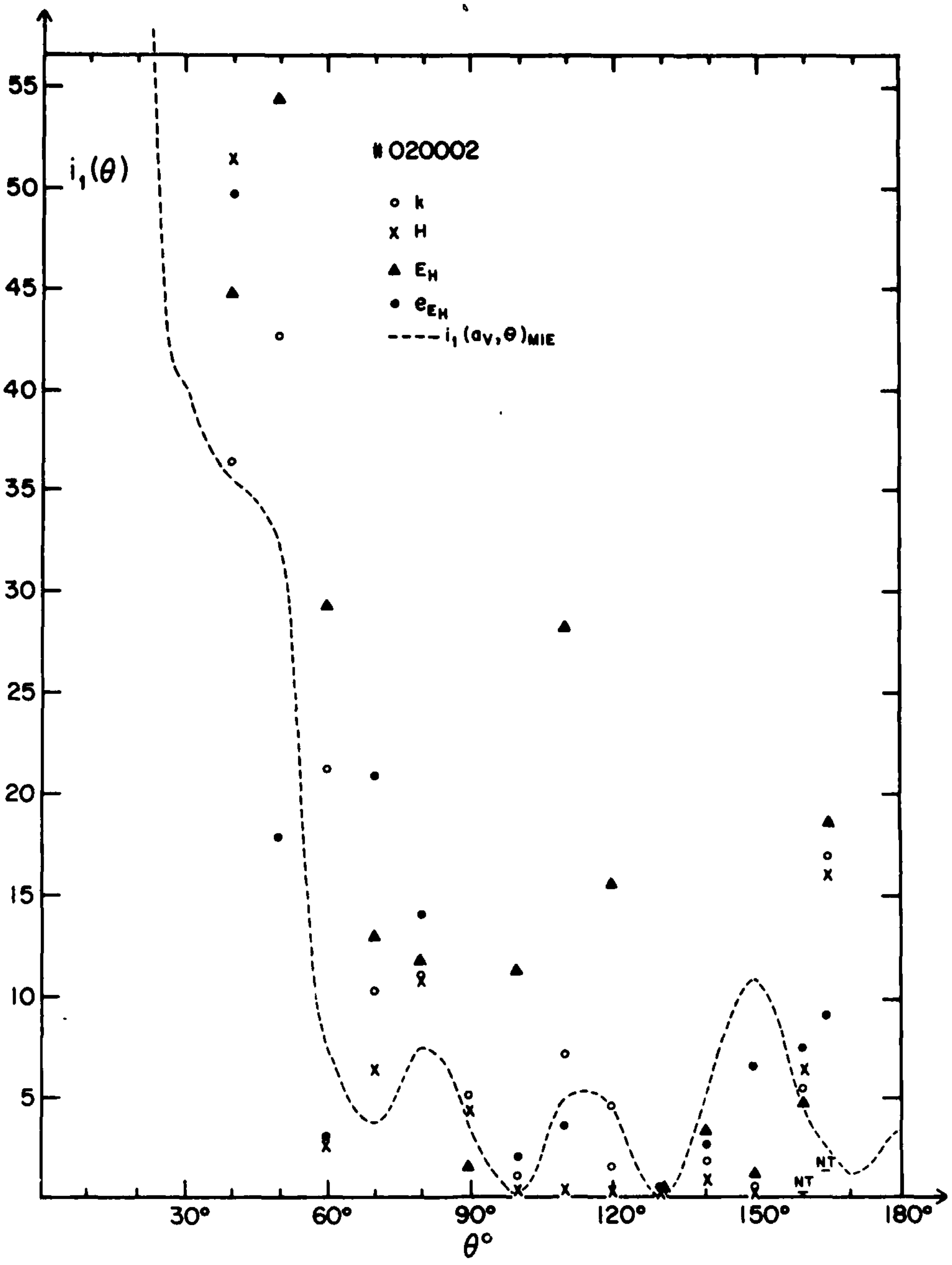

Fig. 21A Same $i_1(\theta)$ vs θ plot as in Fig. 20A, except that this rough particle has target parameters x_V=6.108, m=1.362.

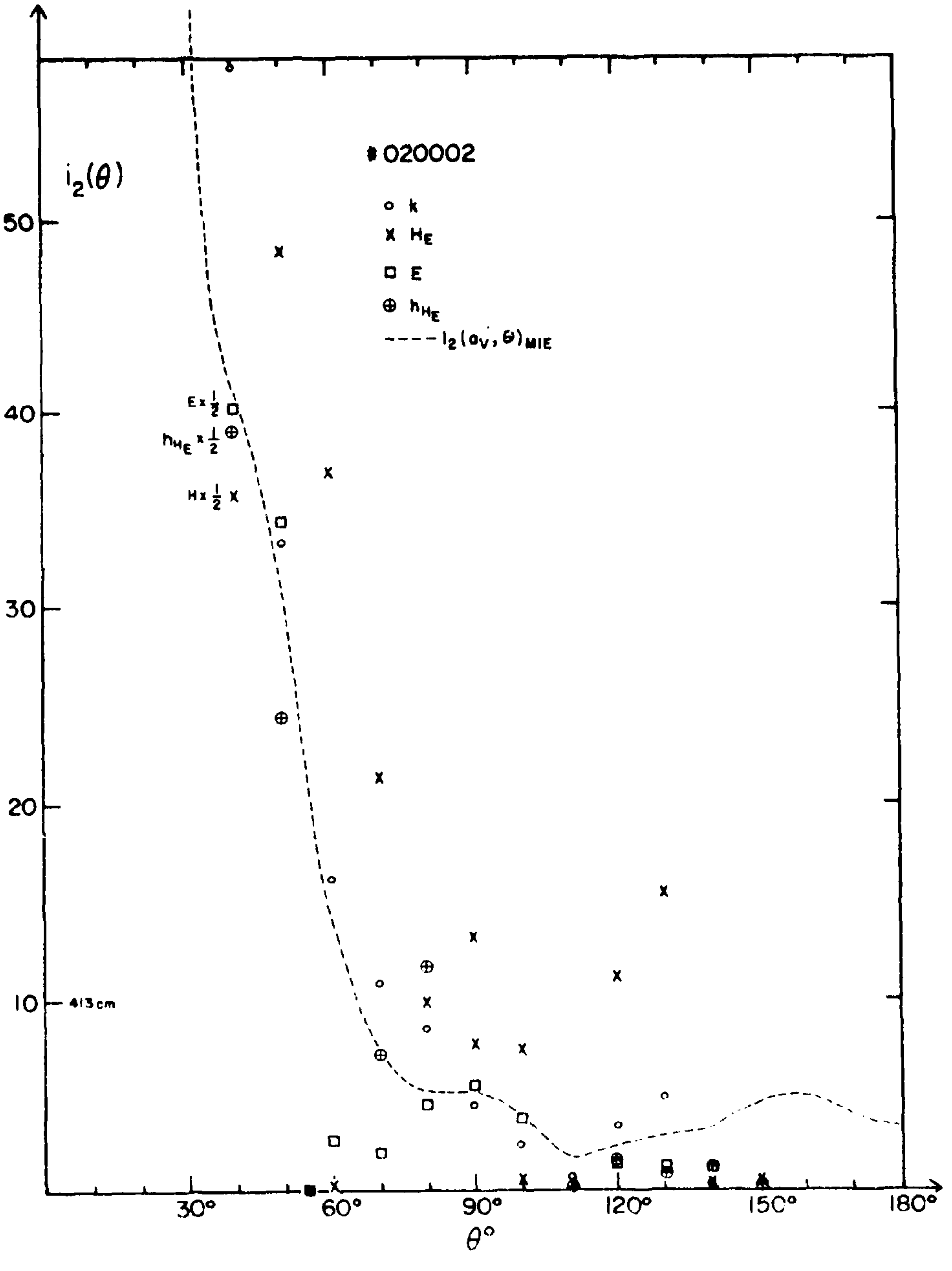

Fig. 21B Same $i_2(\theta)$ vs θ plot as in Fig. 20B, except that the rough particle has target parameters x_V=6.108, m=1.362

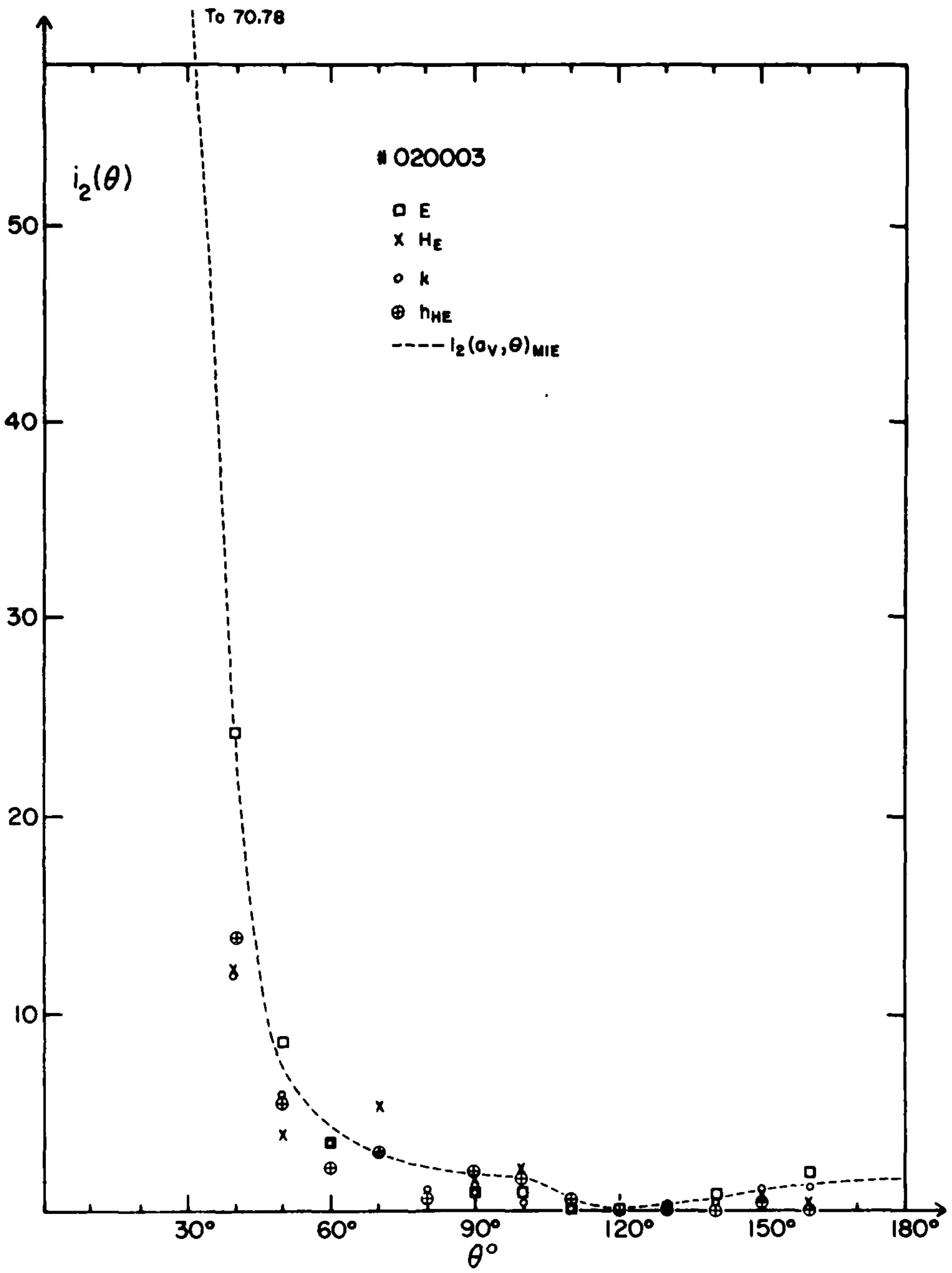

Fig. 22A Same $i_2(\theta)$ vs θ plot as in Fig. 20B except that this rough particle has target parameters $x_V=4.314$, $m=1.354$.

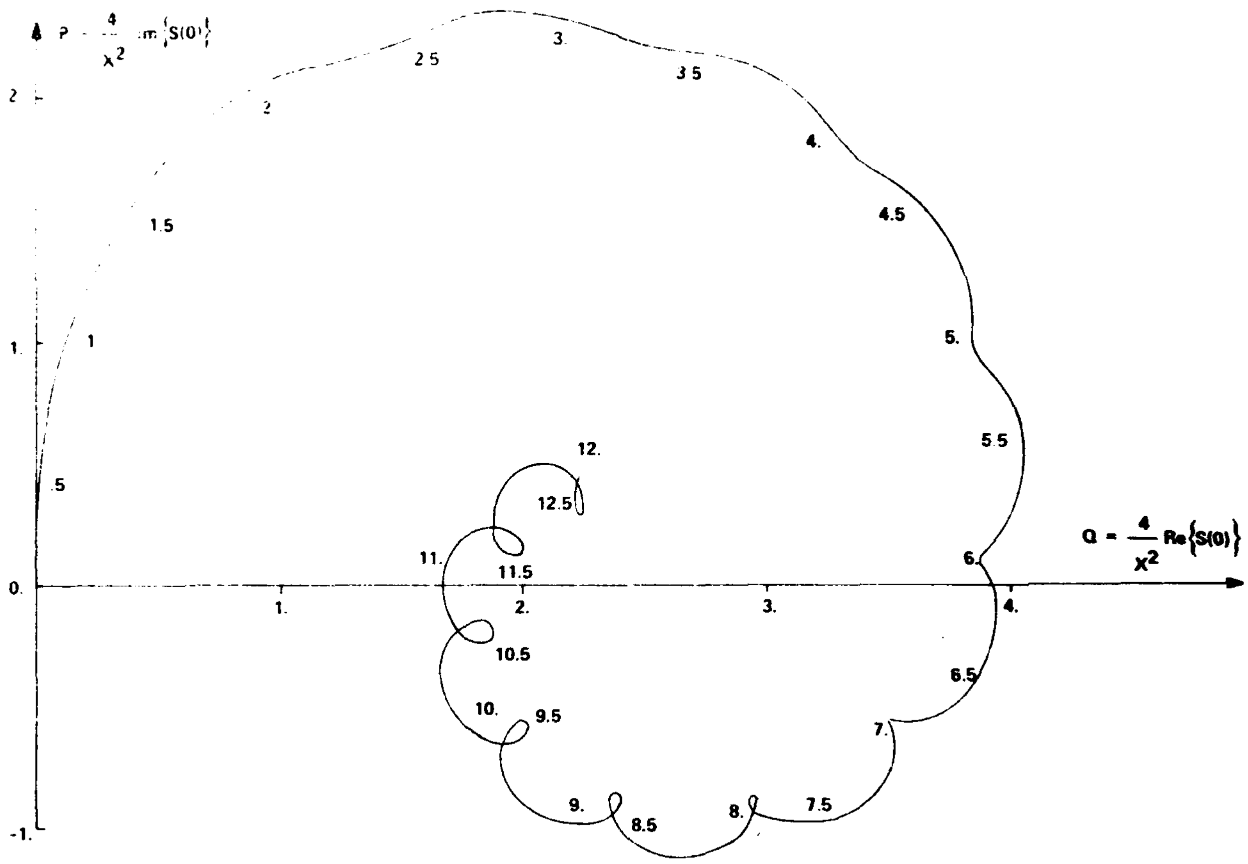

Fig. 23A P-Q plot as function of size x, the running number, for spherical particles by Mie theory. m=1.365.

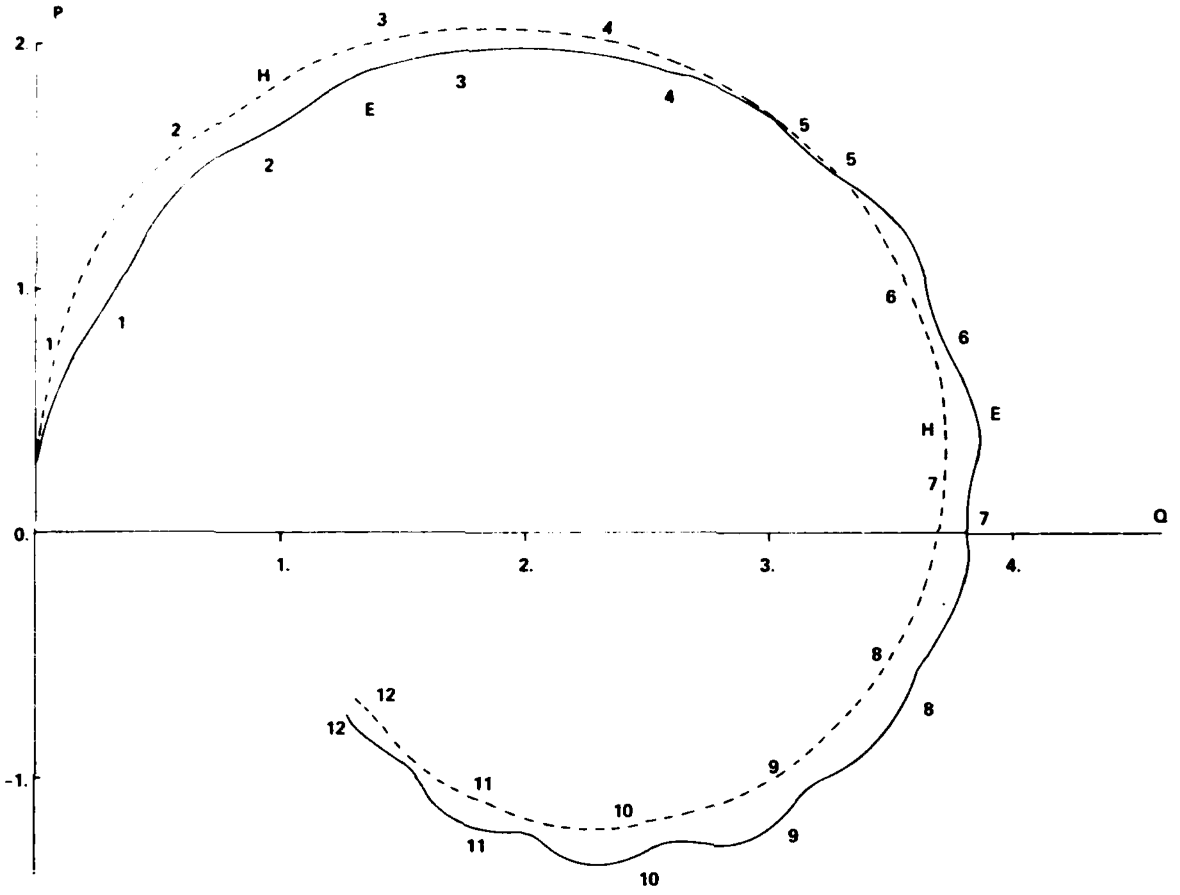

Fig. 23B P-Q plot as function of size x, the running number, for infinite dielectric cylinders (theoretical). m=1.2664. Two perpendicular incidence cases E and H are considered, in which the incident polarization is parallel and perpendicular to the cylinder axis respectively.

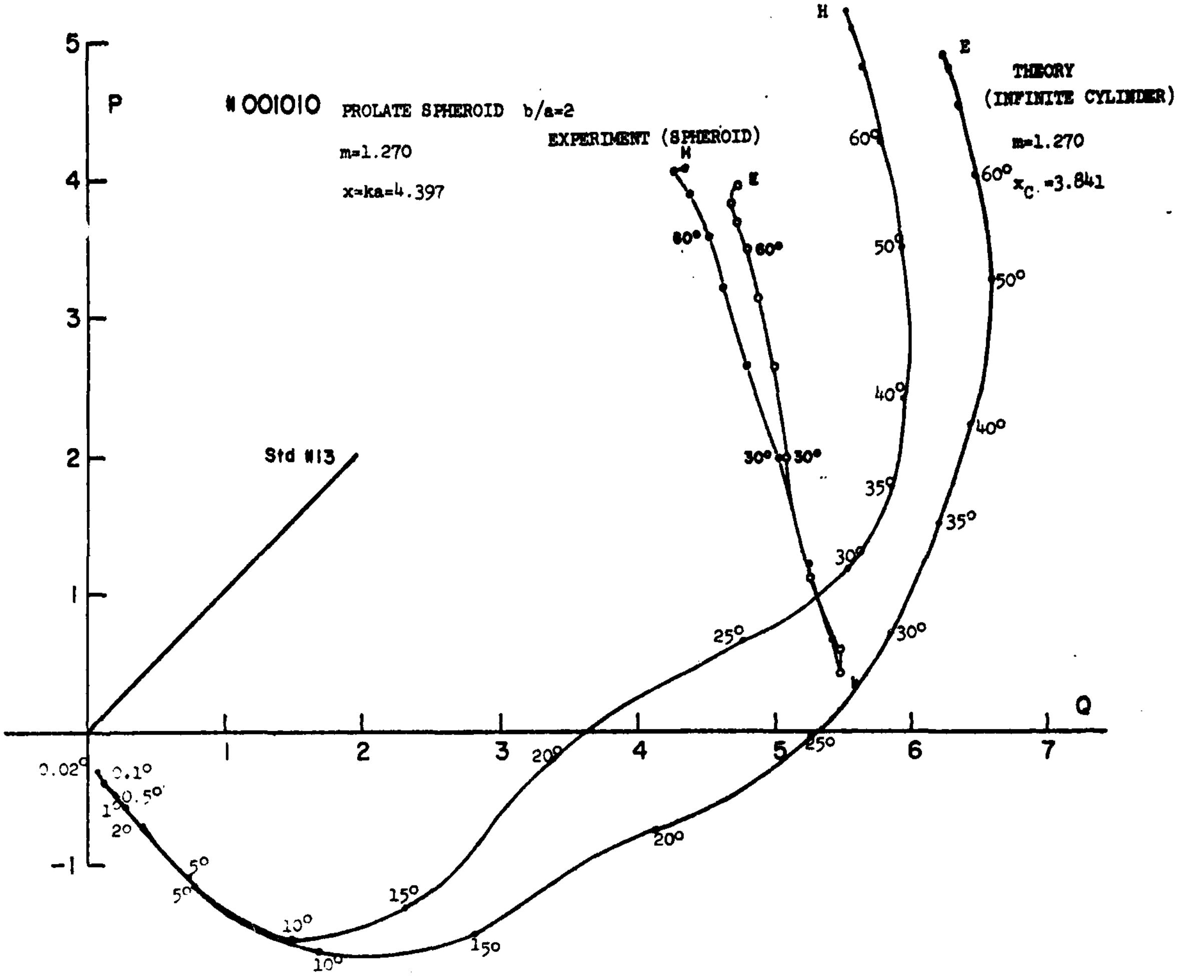

Fig. 24 Comparison of an experimental P-Q plot for a spheroid (Fig. 6C) and a theoretical P-Q plot for an infinite cylinder of an appropriate size

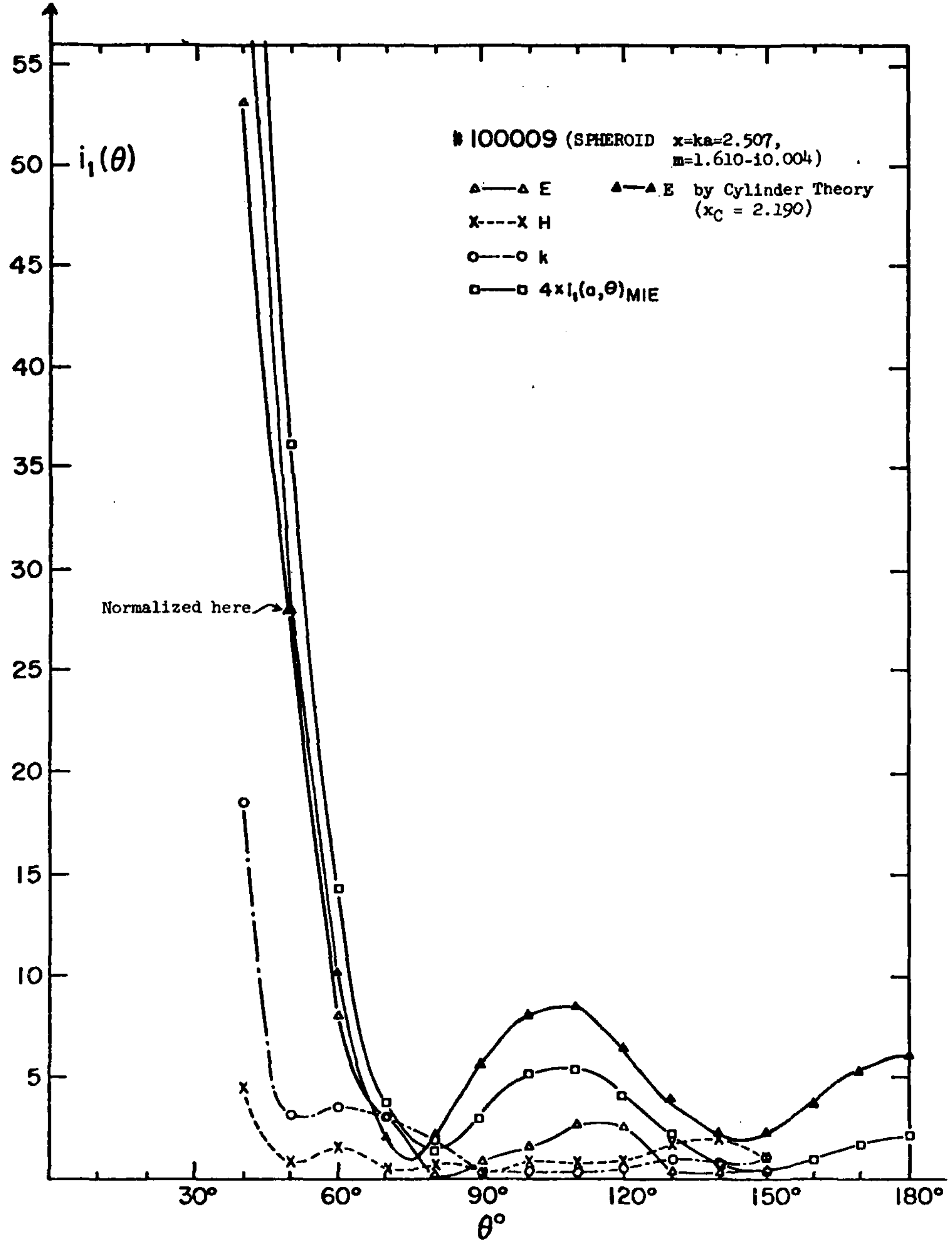

Fig. 25A Comparison of an experimental i_1 (θ) plot (Fig. 14A) and a theoretical i_1 (θ) vs 0 plot for an appropriately sized cylinder

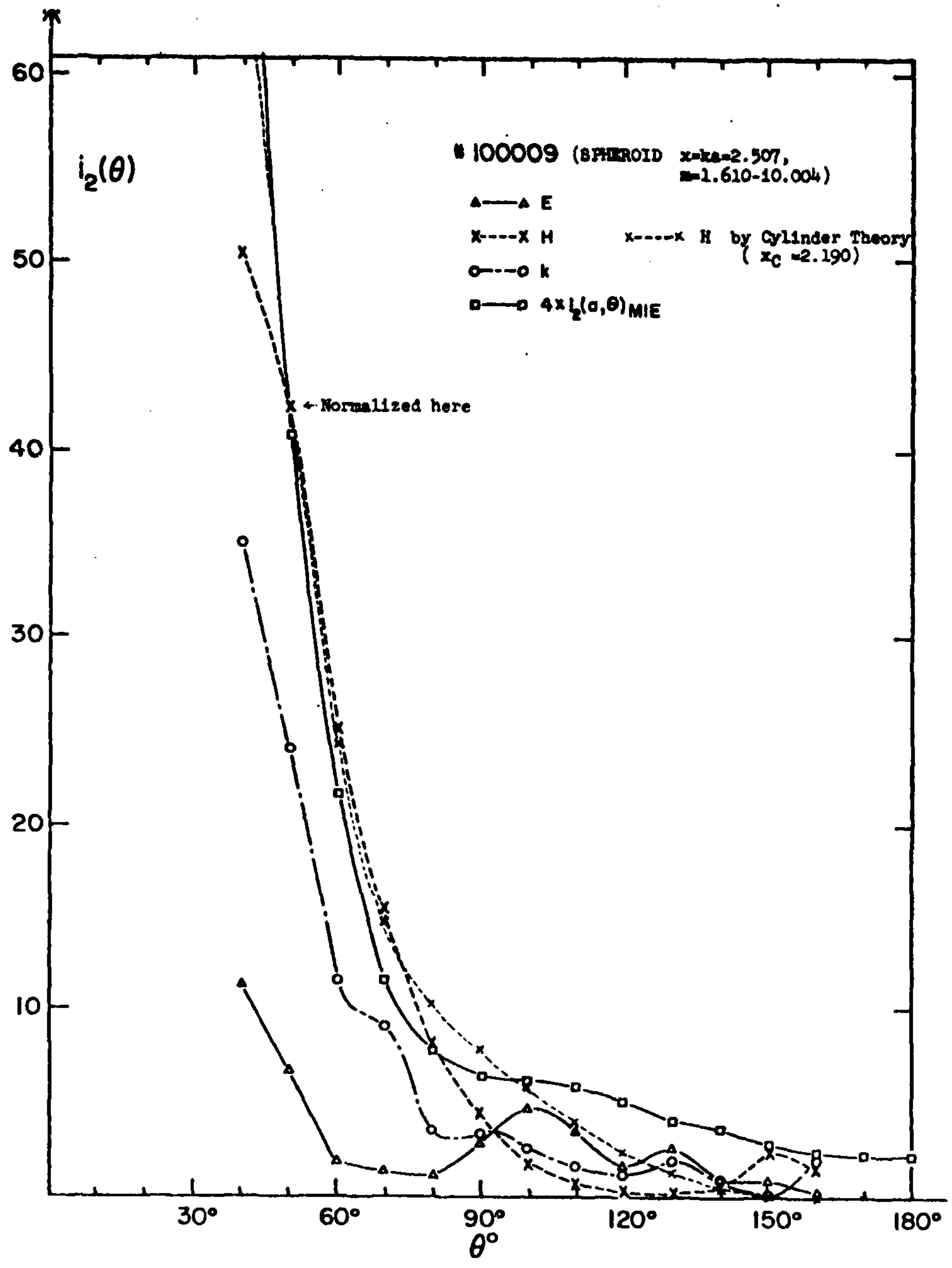

Fig. 25B Comparison of an experimental i_2 (θ) vs θ plot (Fig. 14B) and a theoretical i_2(θ) vs θ plot for an appropriately sized cylinder

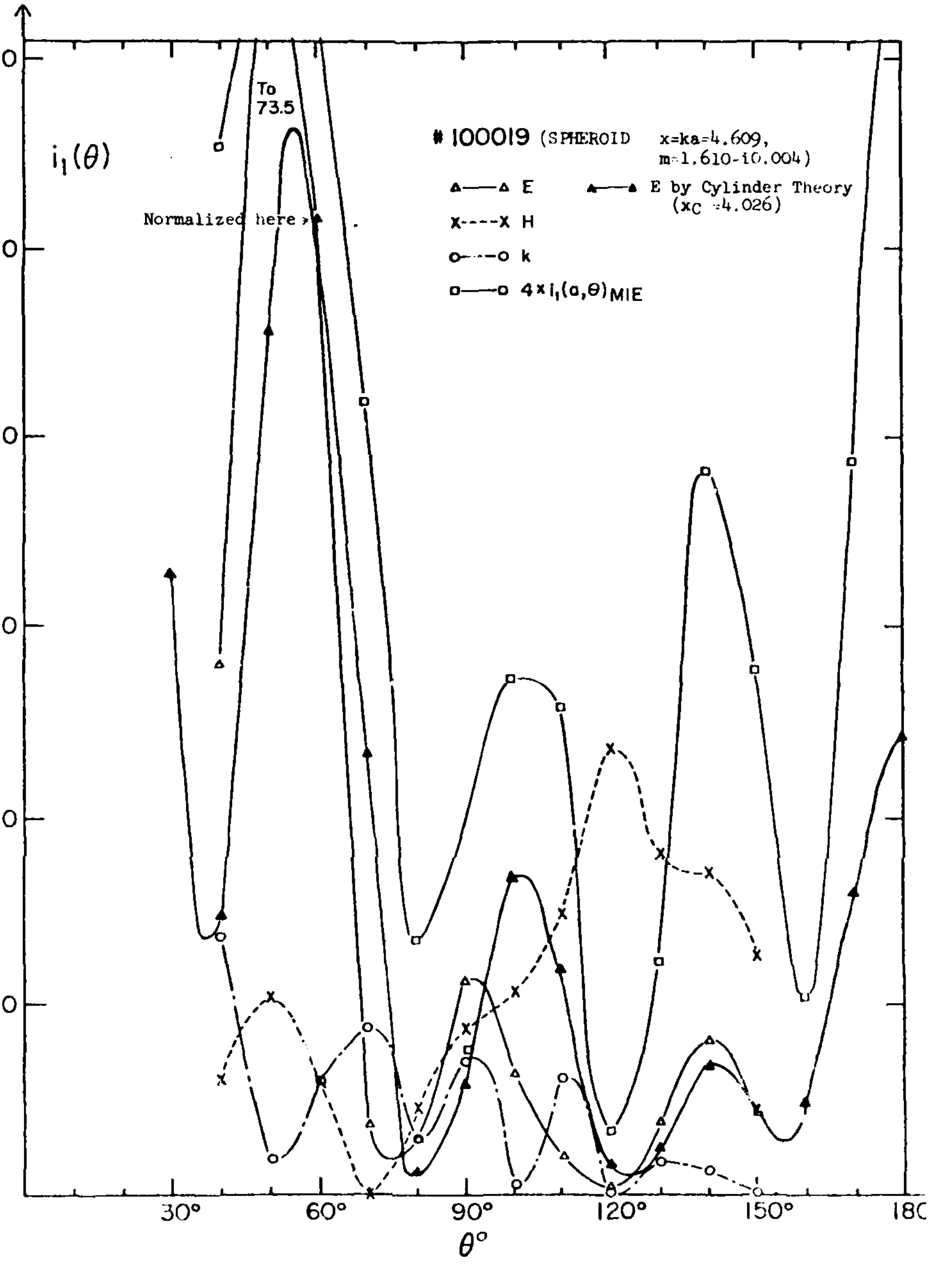

Fig. 20A Comparison of an experimental i_1 (θ) vs θ plot (Fig 19A) and a theoretical i_1 vs θ plot for appropriately sized cylinder

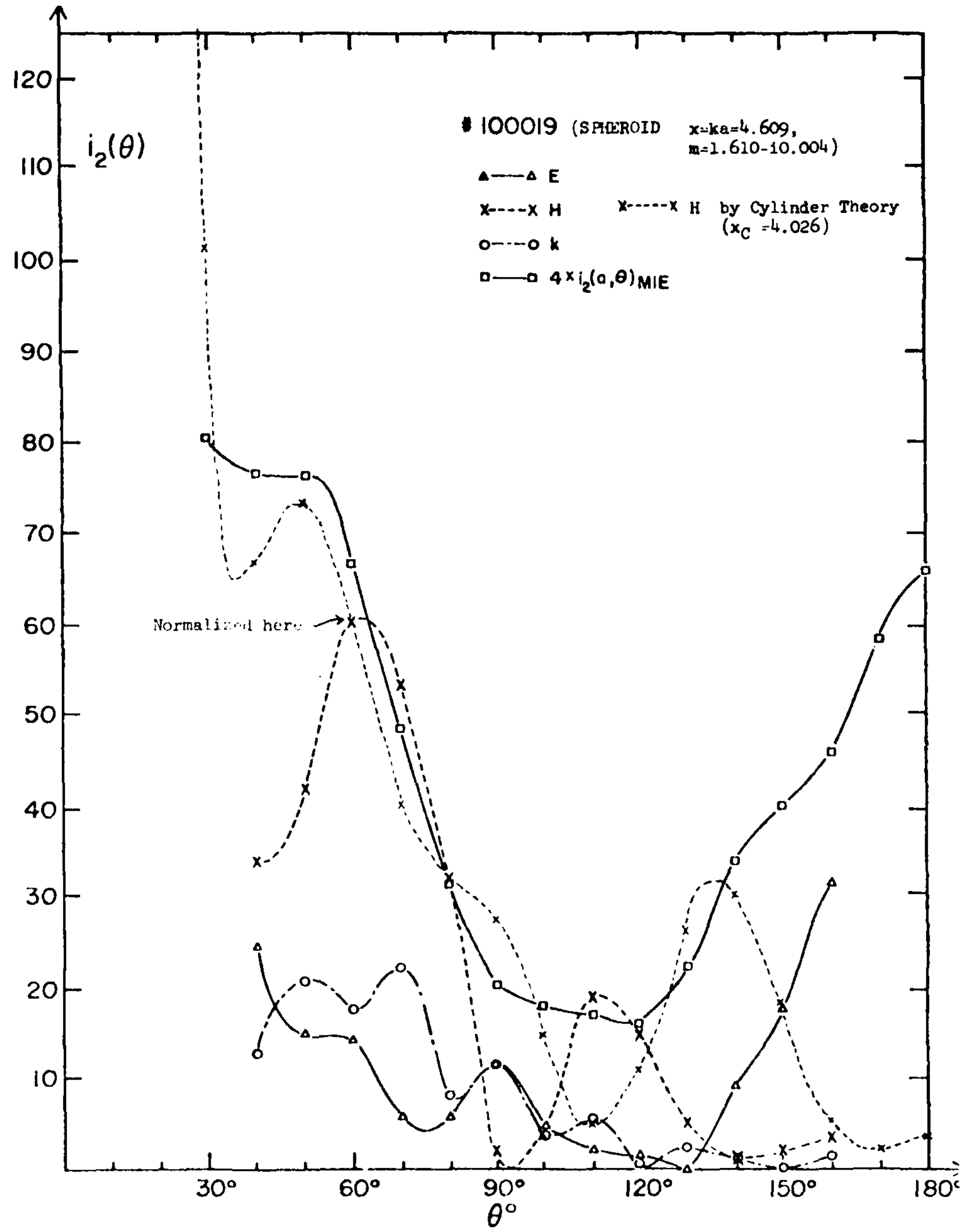

Fig. 26B Comparison of an experimental $i_2(\theta)$ vs θ plot (Fig. 19B) and a theoretical $i_2(\theta)$ vs θ plot for appropriately sized cylinder

REFERENCES

Asano, S. and Yamamoto, G., Appl. Opt., 14, 29 (1975).

Barber, P. and Yeh, C., Appl. Opt., 14, 2864 (1975).

Beard, C. I., Kays, T. H. and Twersky, V., J. Appl. Phys., 33, 2851 (1962).

Feenberg, E., Phys. Rev., 40, 40 (1932).

Greenberg, J.M., J. Appl. Phys., 31, 82 (1960).

Greenberg, J.M., Pedersen, N. E. and Pedersen, J. C., J. Appl. Phys., 32, 233 (1961).

Greenberg, J.M., Lind, A.C., Wang, R.T. and Libelo, L.F., in "Electromagnetic Scattering", Kerker, M., Ed., p. 123 (Pergamon, New York, 1963).

Greenberg, J.M., Lind, A.C., Wang, R.T. and Libelo, L.F., in "Electromagnetic Scattering", Rowell, L. and Stein, R., Eds., p. 3 (Gordon & Breach, New York, 1967).

Greenberg, J.M., Interstellar Grains, in "Nebulae and Interstellar Matter", Middlehurst, B.M. and Aller, L.H. Eds., p. 221 (Univ. of Chicago Press, 1968).

Greenberg, J.M., Wang, R.T. and Bangs, L., Nature, Phys. Sci., 230, 110 (1971).

Greenberg, J.M., in "Planets, Stars and Nebulae studied with Photopolarimetry" Gehrels, T. Ed., p. 107 (Univ. of Arizona Press, 1974).

Hansen, R.C. and Bailin, L.L., IRE Trans. Ant. Prop., 7 S458 (1959).

Latimer, P., J. Colloid & Interface Sci. 53, 102 (1975).

Lind, A.C., Wang, R.T. and Greenberg, J.M., Appl. Opt., 4, 1555 (1965).

Lind, A.C. and Greenberg, J.M., J. Appl. Phys., 37, 3195 (1966).

Lind, A.C., Ph.D. Thesis, Rensselaer Polytechnic Institute, Troy, N.Y. (1966).

Montroll, E.W. and Greenberg, J.M., in Proc. of Symposia on Appl. Math., Wave Motion and Vibration, Pittsburgh, Pa. 5, 103 (McGraw Hill, N.Y. 1954).

Roberts, S. and von Hippel, A., J. Appl. Phys. 17, 610 (1946).

Rhodes, D.R., Proc. IRE 1408 (Sept. 1954).

Stratton, J.A., "Electromagnetic Theory"(McGraw Hill, New York 1941).

Shah, G.A. and Vardya, M.S., Nature, Phys. Sci., 235, 115 (1972).

Silver, S. Ed., Microwave Antenna Theory and Design, MIT Rad. Lab. Series 12 (McGraw Hill, N.Y. 1949).

[illegible]RENCES (Cont.)

Silver, S., J. Opt. Soc. America 52, 131 (1962).

Sucher, M., Ed., Handbook of Microwave Measurement (BPI Microwave Research Inst., Brocklyn, N.Y. 1963).

van de Hulst, H.C., Thesis Utrecht, Rech. Astron. Obs. d'Utrecht 11, Pt. 1, (1946).

van de Hulst, H.C., Light Scattering by Small Particles (Wiley, New York 1957).

Wang, R.T., Ph.D. Thesis, Rensselaer Polytechnic Inst. Troy, N.Y. (1968).

Wang, R.T.,and Greenberg, J.M., Appl. Opt., 15, 1212 (1976).

Wang, R.T., Detenbeck, R.W., Giovane, F. and Greenberg, J.M., Final Report, NSF ATM75-15663 (1977).

DISTRIBUTION LIST FOR ARCSL-CR-82037

Names	Copies
CHEMICAL SYSTEMS LABORATORY	
ATTN: DRDAR-CLB	1
ATTN: DRDAR-CLB-C	1
ATTN: DRDAR-CLB-P	1
ATTN: DRDAR-CLB-PS	4
ATTN: DRDAR-CLB-R	1
ATTN: DRDAR-CLB-T	1
ATTN: DRDAR-CLB-TE	1
ATTN: DRDAR-CLC-B	1
ATTN: DRDAR-CLC-C	1
ATTN: DRDAR-CLF	1
ATTN: DRDAR-CLJ-R	2
ATTN: DRDAR-CLJ-L	2
ATTN: DRDAR-CLJ-M	1
ATTN: DRDAR-CLN	1
ATTN: DRDAR-CLN-S	1
ATTN: DRDAR-CLN-ST	1
ATTN: DRDAR-CLT	1
ATTN: DRDAR-CLY-A (Pennsyle, Hundley)	2
ATTN: DRDAR-CLY-R	1
COPIES FOR AUTHOR(S)	
Research Division (CPO)	25
RECORD COPY: DRDAR-CLB-A	1
DEPARTMENT OF DEFENSE	
Defense Technical Information Center	
ATTN: DTIC-DDA-2	2
Cameron Station, Building 5	
Alexandria, VA 22314	
Director	
Defense Intelligence Agency	
ATTN: DB-4G1	1
Washington, DC 20301	
Deputy Under Secretary of Defense for Research and Engineering (R&AT)	
ATTN: Dr. Musa	1
ATTN: COL Friday	1
ATTN: COL Winter	1
Washington, DC 20301	
Defense Advanced Research Projects Agency	
ATTN: Dr. Tegnelia	1
Washington, DC 20301	

Names	Copies
Advanced Research Projects Agency	1
1400 Wilson Boulevard	
Arlington, VA 22209	
DEPARTMENT OF THE ARMY	
HQDA	
ATTN: DAMO-NCC	1
ATTN: DAMO-NC/COL Robinson (P)	1
WASH DC 20310	
HQ DA	
Office of the Deputy Chief of Staff for Research, Development & Acquisition	
ATTN: DAMA-CSS-C	1
Washington, DC 20310	
HQ Sixth US Army	
ATTN: AFKC-OP-NBC	1
Presidio of San Francisco, CA 94129	
Commander	
DARCOM, STITEUR	
ATTN: DRXST-STI	1
Box 48, APO New York 09710	
Commander	
USASTCFEO	
ATTN: MAJ Mikeworth	1
APO San Francisco 96328	
Army Research Office	
ATTN: DRXRO-CB (Dr. R. Ghirardelli)	1
ATTN: DRXRO-GS	1
ATTN: Dr. W. A. Flood	1
P.O. Box 12211	
Research Triangle Park, NC 27709	
HQDA ODUSA (OR)	
ATTN: Dr. H. Fallin	1
Washington, DC 20310	
HQDA (DAMO-RQD)	
ATTN: MAJ C. Collat	1
Washington, DC 20310	

HQDA, OCE
ATTN: DAEN-RDM (Dr. Gomez) 1
Massachusetts Ave, NW
Washington, DC 20314

OFFICE OF THE SURGEON GENERAL

Commander
US Army Medical Research and Development Command
ATTN: SGRD-UBG (Mr. Eaton) 1
ATTN: SGRD-UBG-OT (CPT Johnson) 1
ATTN: LTC Don Gensler 1
Fort Detrick, MD 21701

Commander
US Army Medical Bioengineering Research and Development Laboratory
ATTN: SGRD-UBD-AL, Bldg 568 1
Fort Detrick, Frederick, MD 21701

Commander
USA Medical Research Institute of Chemical Defense
ATTN: SGRD-UV-L 1
Aberdeen Proving Ground, MD 21010

US ARMY MATERIEL DEVELOPMENT AND READINESS COMMAND

Commander
US Army Materiel Development and Readiness Command
ATTN: DRCDE-DM 1
ATTN: DRCLDC 1
ATTN: DRCMT 1
ATTN: DRCSF-P 1
ATTN: DRCSF-S 1
ATTN: DRCDL (Mr. N. Klein) 1
ATTN: DRCBSI-EE (Mr. Giambalvo) 1
ATTN: DRCDMD-ST (Mr. T. Shirata) 1
5001 Eisenhower Ave
Alexandria, VA 22333

Commander
US Army Foreign Science & Technology Center
ATTN: DRXST-MT3 1
ATTN: DRXST-MT3 (Poleski) 1
220 Seventh St., NE
Charlottesville, VA 22901

Director
DARCOM Field Safety Activity
ATTN: DRXOS-SE (Mr. Yutmeyer) 1
Charlestown, IN 47111

PM Smoke/Obscurants
ATTN: DRCPM-SMK-E (A. Van de Wal) 1
ATTN: DRCPM-SMK-M 1
ATTN: DRCPM-SMK-T 1
Aberdeen Proving Ground, MD 21005

Director
US Army Materiel Systems Analysis Activity
ATTN: DRXSY-MP 1
ATTN: DRXSY-CA (Mr. Metz) 1
ATTN: DRXSY-FJ (J. O'Bryon) 1
ATTN: DRXSY-GP (Mr. Fred Campbell) 1
Aberdeen Proving Ground, MD 21005

USA AVIATION RESEARCH AND DEVELOPMENT COMMAND

Director
Applied Technology Lab
USARTL (AVRADCOM)
ATTN: DAVDL-ATL-ASV 1
ATTN: DAVDL-ATL-ASW 1
ATTN: DAVDL-EV-MOS (Mr. Gilbert) 1
Ft. Eustis, VA 23604

Commander
USA Avionics R&D Activity
ATTN: DAVAA-E(M. E. Sonatag) 1
Ft. Monmouth, NJ 07703

USA MISSILE COMMAND

Commander
US Army Missile Command
Director, Energy Directorate
ATTN: DRSMI-RHFT 1
ATTN: DRSMI-RMST 1
ATTN: DRSMI-YLA (N. C. Katos) 1
Redstone Arsenal, AL 35809

Commander
US Army Missile Command
Redstone Scientific Information Center
ATTN: DRSHI-REO (Mr. Widenhofer) 1
ATTN: DRSMI-RGT (Mr. Matt Maddix) 1
ATTN: DRDMI-CGA (Dr. B. Fowler) 1
ATTN: DRDMI-KL (Dr. W. Wharton) 1
ATTN: DRDMI-TE (Mr. H. Anderson) 1
Redstone Arsenal, AL 35809

Commander
US Army Missile Command
Redstone Scientific Information Center
ATTN: DRSMI-RPR (Documents) 1
Redstone Arsenal, AL 35809

USA COMMUNICATIONS-ELECTRONICS COMMAND

Commander
USA Communications-Electronics Command
ATTN: DRSEL-WL-S (Mr. J. Charlton) 1
Ft. Monmouth, NJ 07703

Commander
USA Electronics Research and
Development Command
ATTN: DRDEL-CCM (Dr. J. Scales) 1
ATTN: DELHD-RT-CB (Dr. Sztankay) 1
Adelphi, MD 20783

Commander
Harry Diamond Laboratories
ATTN: DRXDO-RCB (Dr. Donald Wortman) 1
ATTN: DRXDO-RCB (Dr. Clyde Morrison) 1
ATTN: DRXDO-RDC (Mr. D. Giglio) 1
2800 Powder Mill Road
Adelphi, MD 20783

Commander
USA Materials & Mechanics Research Center
ATTN: DRXMR-KA (Dr. Saul Isserow) 1
Watertown, MA 02172

Commander
USA Cold Region Research Engineering Laboratory
ATTN: George Aitken 1
Hanover, NH 03755

Commander/Director
Combat Surveillance and Target
Acquisition Laboratory
ERADCOM
ATTN: DELCS-P (E. Frost) 1
Ft. Monmouth, NJ 07703

Director
Atmospheric Sciences Laboratory
ATTN: DELAS-AS (Dr. Charles Bruce) 1
ATTN: DELAS-AS-P (Mr. Tom Pries) 1
ATTN: DELAS-EO-EN (Dr. Donald Snider) 1
ATTN: DELAS-EO-EN (Mr. James Gillespie) 1
ATTN: DELAS-EO-ME (Dr. Frank Niles) 1
ATTN: DELAS-EO-ME (Dr. Ronald Pinnick) 1
ATTN: DELAS-EO-MO (Dr. Melvin Heaps) 1
ATTN: DELAS-EO-MO (Dr. R. Sutherland) 1
ATTN: DELAS-EO-S (Dr. Louis Duncan) 1
White Sands Missile Range, NM 88002

US ARMY ARMAMENT RESEARCH AND
DEVELOPMENT COMMAND

Commander
US Army Armament Research and
Development Command
ATTN: DRDAR-LCA-L 1
ATTN: DRDAR-LCE-C 1
ATTN: DRDAR-LCU-CE 1
ATTN: DRDAR-NC (COL Lymn) 3
ATTN: DRDAR-SCA-T 1
ATTN: DRDAR-SCF 1
ATTN: DRDAR-SCP 1
ATTN: DRDAR-SCS 1
ATTN: DRDAR-TDC (Dr. D. Gyorog) 1
ATTN: DRDAR-TSS 2
ATTN: DRCPM-CAWS-AM 1
Dover, NJ 07801

US Army Armament Research and
Development Command
ATTN: DRDAR-TSE-OA (Robert Thresher) 1
National Space Technology Laboratories
NSTL Station, MS 39529

Requirements and Analysis Office
Foreign Intelligence and Threat
Projection Division
ATTN: DRDAR-RAI-C 1
Aberdeen Proving Ground, MD 21010

Commander
ARRADCOM
ATTN: DRDAR-QAC-E 1
Aberdeen Proving Ground, MD 21010

Director
USA Ballistic Research Laboratory
ARRADCOM
ATTN: DRDAR-BLB 1
ATTN: DRDAR-TSB-S 1
Aberdeen Proving Ground, MD 21005

US ARMY ARMAMENT MATERIEL READINESS
COMMAND

Commander
US Army Armament Materiel Readiness Command
ATTN: DRSAR-ASN 1
ATTN: DRSAR-IRI-A 1
ATTN: DRSAR-LEP-L 1
ATTN: DRSAR-SF 1
Rock Island, IL 61299

Commander
US Army Dugway Proving Ground
ATTN: Technical Library (Docu Sect) 1
Dugway, UT 84022

US ARMY TRAINING & DOCTRINE COMMAND

Commandant
US Army Infantry School
ATTN: CTDD, CSD, NBC Branch 1
Fort Benning, GA 31905

Commandant
US Army Missile & Munitions Center
and School
ATTN: ATSK-CM 1
Redstone Arsenal, AL 35809

Commander
US Army Logistics Center
ATTN: ATCL-MG 1
Fort Lee, VA 23801

Commandant
US Army Chemical School
ATTN: ATZN-CM-C 1
ATTN: ATZN-CM-AD 2
ATTN: ATZN-CN-CDM (Dr. J. Scully) 1
Fort McClellan, AL 36205

Commander
USAAVNC
ATTN: ATZQ-D-MS 1
Fort Rucker, AL 36362

Commander
USA Combined Arms Center and
Fort Leavenworth
ATTN: ATZL-CAM-IM 1
ATTN: ATZL-CA-SAN 1
ATTN: ATZL-CA-TM-K 1
Fort Leavenworth, KS 66027

Commander
US Army Infantry Center
ATTN: ATSH-CD-MS-C 1
ATTN: ATSH-CD-MS-F 1
ATTN: ATZB-DPT-PO-NBC 1
Fort Benning, GA 31905

Commander
USA Training and Doctrine Command
ATTN: ATCD-N 1
ATTN: ATCD-TEC (Dr. M. Pastel) 1
ATTN: ATCD-Z 1
Fort Monroe, VA 23651

Commander
US Army Armor Center
ATTN: ATZK-CD-MS 1
ATTN: ATZK-PPT-PO-C 1
Fort Knox, KY 40121

Commander
US Army TRADOC System Analysis Activity
ATTN: ATAA-SL 1
ATTN: ATAA-TDB (L. Dominguez) 1
White Sands Missile Range, NM 88002

Commander
USA Field Artillery School
ATTN: ATSF-GD-RA 1
Ft. Sill, OK 73503

Director
USA Concepts Analysis Agency
ATTN: MOCA-SMC (Hal Hock) 1
8120 Woodmont Avenue
Bethesda, MD 20014

Los Alamos National Laboratory
ATTN: T-DOT, MS B279 (S. Gerstl) 1
Los Alamos, NM 87545

US ARMY TEST & EVALUATION COMMAND

Commander
US Army Test & Evaluation Command
ATTN: DRSTE-CM-F 1
ATTN: DRSTE-CT-T 1
ATTN: DRSTE-AD-M (Warren Balty) 1
Aberdeen Proving Ground, MD 21005

Commander
USA EPG
ATTN: STEEP-MM-IS 1
ATTN: STEEP-MT-DS (CPT Decker) 1
Ft. Huachuca, AZ 85613

Commander
Dugway Proving Ground
ATTN: STEDP-MT (Dr. L. Solomon) 1
Dugway, UT 84022

DEPARTMENT OF THE NAVY

Commander
Naval Research Laboratory
ATTN: Code 5709 (Mr. W. E. Howell) 1
ATTN: Code 6532 (Mr. Curcio) 1
ATTN: Code 6532 (Mr. Trusty) 1
ATTN: Code 6530-2 (Mr. Gordon Stamm) 1
ATTN: Code 8320 (Dr. Lothar Ruhnke) 1
ATTN: Code -326 (Dr. James Fitzgerald) 1
ATTN: Code 43202 (Dr. Hermann Gerber) 1
4555 Overlook Avenue, SW
Washington, DC 20375

Chief, Bureau of Medicine & Surgery
Department of the Navy
ATTN: MED 3C33 1
Washington, DC 20372

Commander
Naval Air Systems Command
ATTN: Code AIR-301C (Dr. H. Rosenwasser) 1
ATTN: Code AIR-5363 (D. C. Caldwell) 1
Washington, DC 20361

Commander
Naval Sea Systems Command
ATTN: SEA-62Y13 (LCDR Richard Gilbert) 1
ATTN: SEA-62Y21 (A. Kanterman) 1
ATTN: SEA-62Y21 (LCDR W. Major) 1
Washington, DC 20362

Project Manager
Theatre Nuclear Warfare Project Office
ATTN: TN-09C 1
Navy Department
Washington, DC 20360

Institute for Defense Analysis 1
400 Army-Navy Drive
Arlington, VA 22202

Commander
Naval Surface Weapons Center
Dahlgren Laboratory
ATTN: DX-21 1
ATTN: Mr. R. L. Hudson 1
ATTN: F-56 (Mr. Douglas Marker) 1
Dahlgren, VA 22448

Commander
Naval Intelligence Suport Center 1
ATTN: Code 434 (H. P. St.Aubin) 1
4301 Suitland Road
Suitland, MD 20390

Commander
Naval Explosive Ordnance Disposal
Technology Center
ATTN: AC-3 1
Indian Head, MD 20640

Officer-in-Charge
Marine Corps Detachment 1
Naval Explosive Ordnance Disposal
Technology Center
Indian Head, MD 20640

Commander
Naval Air Development Center
ATTN: Code 2012 (Dr. Robert Helmbold) 1
Warminster, PA 18974

Commander
Naval Weapons Center
ATTN: Code 382 (L. A. Mathews) 1
ATTN: Code 3882 (Dr. C. E. Dinerman) 1
ATTN: Code 3918 (Dr. Alex Shlanta) 1
China Lake, CA 93555

Commanding Officer
Naval Weapons Support Center
Applied Sciences Department
ATTN: Code 50C, Bldg 190 1
ATTN: Code 502 (Carl Lohkamp) 1
Crane, IN 47522

US MARINE CORPS

Commanding General
Marine Corps Development and
Education Command
ATTN: Fire Power Division, D091 1
Quantico, VA 22134

DEPARTMENT OF THE AIR FORCE

HQ AFLC/LOWMM 1
Wright-Patterson AFB, OH 45433

HQ AFSC/SDZ 1
ATTN: CPT D. Riediger
Andrews AFB, MD 20334

USAF TAWC/THL 1
Eglin AFB, FL 32542

USAF SC
ATTN: AD/YQ (Dr. A. Vasiloff) 1
ATTN: AD/YQO (MAJ Owens) 1
Eglin AFB, FL 32542

AFAMRL/TS
ATTN: COL Johnson 1
Wright-Patterson AFB, OH 45433

Commander
Hanscom Air Force Base
ATTN: AFGL-POA (Dr. Frederick Volz) 1
Bedford, MA 01731

Headquarters
Tactical Air Command
ATTN: DRP 1
Langley AFB, VA 23665

AFOSR/NE
ATTN: MAJ H. Winsor 1
Bolling AFB, DC 20332

AD/SPC 1
Eglin AFB, FL 32542

Dr. Charles Arpke 1
OSV Field Office
P.O. Box 1925
Eglin AFB, FL 32542

OUTSIDE AGENCIES

Battelle, Columbus Laboratories
ATTN: TACTEC 1
505 King Avenue
Columbus, OH 43201

Toxicology Information Center, JH 652
National Research Council 1
2101 Constitution Ave., NW
Washington, DC 20418

Dr. W. Michael Farmer, Assoc Prof, Physics
University of tennessee Space Institute 1
Tullahoma, TN 37388

ADDITIONAL ADDRESSEES

Office of Missile Electronic Warfare
ATTN: DELEW-M-T-AC (Ms Arthur) 1
White Sands Missile Range, NM 88002

US Army Mobility Equipment Research and
Development Center
ATTN: DROME-RT (Mr. O. F. Kezer) 1
Fort Belvoir, VA 22060

Director
US Night Vision and EO Laboratories
ATTN: DRSEL-NV-VI (Dr. R. G. Buser) 1
ATTN: DRSEL-NV-VI (Mr. R. Bergemann) 1
ATTN: DELNV-VI (Luanne Obert) 1
ATTN: DELNV-L (D. N. Spector) 1
Fort Belvoir, VA 23651

Commandant
Academy of Health Sciences, US Army
ATTN: HSHA-CDH 1
ATTN: HSHA-IPM 2
Fort Sam Houston, TX 78234

Commander
US Army Armament Research and
Development Command
ATTN: DRDAR-LCE (Mr. Scott Morrow) 1
Dover, NJ 07801

4 -

DT